2010-11-02

Halo Ion Trap Mass Spectrometry: Design, Instrumentation, and Performance

Miao Wang
Brigham Young University - Provo

BYU ScholarsArchive Citation
Wang, Miao, "Halo Ion Trap Mass Spectrometry: Design, Instrumentation, and Performance" (2010). *Theses and Dissertations*. 2458.
https://scholarsarchive.byu.edu/etd/2458

Halo Ion Trap Mass Spectrometry: Design, Instrumentation, and Performance

Miao Wang

A dissertation submitted to the faculty of
Brigham Young University
in partial fulfillment of the requirements for the degree of

Doctor of Philosophy

Milton L. Lee, Ph. D., Committee Chair
Daniel E. Austin, Ph. D., Committee Member
Aaron R. Hawkins, Ph. D., Committee Member
H. Dennis Tolley, Ph. D., Committee Member
David V. Dearden, Ph. D., Committee Member

Department of Chemistry and Biochemistry

Brigham Young University

December 2010

ABSTRACT

Halo Ion Trap Mass Spectrometry: Design, Instrumentation, and Performance

Miao Wang

Department of Chemistry and Biochemistry

Doctor of Philosophy

New ion trap mass spectrometry (ITMS) instrumentation, the toroidal IT and halo IT, were developed to meet the significant growth in on-site analysis applications. The miniature toroidal IT mass analyzer was operated with radio frequency (RF) trapping voltages of 3 $kV_{p\text{-}p}$ or less. Despite its reduced dimensions, it has roughly the same ion trapping capacity as conventional 3D quadrupole ITs. Unit-mass resolved spectra for *n*-butylbenzene, xenon, and naphthalene were obtained. The desired linear mass scale was obtained using conventional mass-selective instability scan combined with resonance ejection.

The halo IT was also based on toroidal trapping geometry and microfabrication technology, consisting of two parallel ceramic plates, the facing surfaces of which were imprinted with sets of concentric ring electrodes. Unlike conventional ITs, in which hyperbolic metal electrodes establish equipotential boundary conditions, electric fields in the halo IT were established by applying different RF potentials to each ring. The potential on each ring could be independently optimized to provide the best trapping field. The halo IT featured an open structure, allowing easy access for *in situ* ionization. The toroidal geometry provided a large trapping volume. The photolithographic fabrication method avoided difficulty in meeting the required machining tolerances. Preliminary mass spectra showed resolution ($m/\Delta m$) of 60–75 when the trap was operated at 1.9 MHz and 500 $V_{p\text{-}p}$. Ion ejection through a hole in the center of the trap, and through slits machined in the ceramic plates were evaluated. The latter ejection method was done to mimic the design of the toroidal IT. The preferred electric fields containing higher order components were optimized by adjusting the potentials applied to the electrode rings of the halo IT without changing the original trapping plates and structure of the IT. The performance of the halo IT with 1% to 7% octopole field (A_4/A_2) components was determined. A best resolution of 280 ($m/\Delta m$) was obtained with 5% octopole field. SIMION simulations were used to demonstrate the toroidal trapping of ions and their mass analysis in both toroidal and halo ITs.

Keywords: Ion trap, Mass spectrometry, Instrumentation, Toroidal ion trap, Halo ion trap.

ACKNOWLEDGEMENTS

I wish to express my profound appreciation to all individuals, teams, and organizations that have financially, physically and mentally contributed to the success of my projects. Their contributions in time and materials have been invaluable for the accomplishment of the work.

First of all, I want to especially express my sincere appreciation and best wishes to my advisor, Dr. Milton L. Lee, for allowing me to work on this project in his laboratory, and for his endless mentoring, patience, encouragement and support. It has been a pleasant and precious opportunity for me to be advised by him. His enlightening vision and enthusiastic attitude in his field will always remain a model for my life. I will continue to assimilate his work ethics and dedicated spirit in my own career. I will always be grateful for everything I learned in his laboratory.

I would also like to sincerely thank all of my other advisory committee members, Dr. Daniel E. Austin, Dr. Aaron R. Hawkins, Dr. H. Dennis Tolley, and Dr. David V. Dearden, for their valuable time and constructive evaluation of my work. Dr. Austin deserves special thanks for his enlightened instruction and invaluable suggestions for my project. Dr. Hawkins guided my efforts in solving problems concerning the fabrication of the ceramic plates.

I would like to thank Dr. Stephen A. Lammert for his guidance in leading me into the ion trap instrumentation field. He invented the toroidal ion trap and spent considerable time teaching me about it. I am grateful to Dr. Samuel E. Tolley, Dr. Edgar D. Lee, Dr. Joseph L. Oliphant, Randall W. Waite, Jeffrey L. Jones and James R. Oliphant of Torion Technologies for their time and help on this project. Dr. Alan L. Rockwood also provided valuable suggestions at the

beginning of the project. I also wish to thank Dr. Zhiping Zhang and Ying Peng for countless discussions during this project. Brett J. Hansen, Hannah E. Quist and Jeffrey D. Maas also deserve my appreciation for fabricating plates for this project. I also thank Eric L. Bylund and Therin P. Garrett for machining the parts that were used in this work.

I give my special thanks to Susan Tachka and Sarah Holstine for their service and support in our group. I am also appreciative of the help, discussions and friendships of my colleagues in the laboratory: Dr. Nosa Agbonkonkon, Dr. Li Zhou, Dr. Shu-ling Lin, Dr. Yansheng Liu, Dr. Aaron Nackos, Dr. Binghe Gu, Dr. Jenny Armenta, Dr. Jikun Liu, Dr. Xuefei Sun, Dr. Yun Li, Dr. Yan Fang, Dr. Yuhong Zhang, Lailiang Zhai, Yuanyuan Li, Jacolin Murray, Jesse Contreras, Tai Van Truong, Xin Chen, Jie Xuan, Dan Li, Kun Liu, Xiaofeng Xie, Anzi Wang, and Pankaj Aggarwal. To my friends and teachers, I thank all of you for your help, encouragement and valuable time we spent together which helped me finish my project.

My family members deserve my utmost appreciation for their deep love and continuous support. My parents, Xixiang Wang and Jianhua Zhang, raised me to believe in myself and devoted themselves to me for achieving my desired goals. The love, understanding, trust and support from them and my sister, Ying Wang, have always given me the strength and courage to overcome any challenge in my life.

Finally, I wish to thank the Department of Chemistry and Biochemistry at Brigham Young University for providing me such a great opportunity and generous financial support. I acknowledge Torion Technologies Inc., the Defense Threat Reduction Agency, Dugway Proving Ground, and the National Aeronautics and Space Administration for their financial support.

TABLE OF CONTENTS

LIST OF ACRONYMS AND SYMBOLS

2D	two-dimensional
3D	three-dimensional
a	the thickness of the germanium layer
A	the cross-sectional area of the germanium
AC	alternating current
AGC	automatic gain control
A_l	expansion coefficient of the order l
A_n	arbitrary coefficient
API	atmospheric pressure ionization
a_r, q_r	Mathieu stability parameters in the radial direction
a_z, q_z	Mathieu stability parameters in the axial direction
CID	collision-induced dissociation
CIT	cylindrical ion trap
$\overline{D}$	pseudopotential depth
DAPI	discontinuous atmospheric pressure interface
DAQ	data acquisition
DC	direct current
DESI	desorption electrospray ionization
DMMP	dimethyl methyl phosphonate
d_x d_y	half-distance between the electrodes in the x or y dimension in RIT
e	ion charge

EI	electron impact
ESI	electrospray ionization
FAIMS	field asymmetric ion mobility spectrometry
FTICR	Fourier transform ion cyclotron resonance mass spectrometry
FWHM	full-width at half-maximum
GC-MS	gas chromatograph-mass spectrometer
GD	glow discharge
IC	integrated circuit
IMS	ion mobility spectrometry
IT	ion trap
ITMS	ion trap mass spectrometry
l	the length of the germanium
LIT	linear ion trap
LMCO	low-mass cutoff
LTP	low-temperature plasma
m	ion mass
m/z	mass-to-charge ratio
MALDI	matrix-assisted laser desorption/ionization
MEMS	micro-electro-mechanical system
MS	mass spectrometry
MS/MS	tandem mass spectrometry
$N_{\max}$	maximum ion density
PA	potential array

PCB	printed circuit board
$P_n(\cos\theta)$	Legendre polynomial
QIT	quadrupole ion trap
QMF	quadrupole mass filter
R	distance from the trapping center to the rotational axis in toroidal ion traps
R	the resistance of the germanium
r_0	radial dimension of the ion trap
r_0	half of the shortest distance between the opposite rods in QMF
r_e	round rod electrode radius in quadrupole mass filter
r_N	normalization radius of ion traps
RF	radiofrequency
RIT	rectilinear ion trap
SPEM	solid phase microextraction
SWIFT	stored waveform inverse Fourier transform
TOF	time-of-flight mass spectrometry
U	DC voltage
V	zero-to-peak amplitude of RF voltage
z_0	axial dimension of the ion trap
β_r, β_z	parameters for secular frequency in the r or z dimension
ε_0	the permittivity of free space
ρ	the resistivity of germanium
ϕ	field potential
Φ_0	RF voltage

Ω	angular component of RF drive frequency
ω_r, ω_z	secular frequency in the *r* or *z* dimension

CHAPTER 1. ION TRAP MASS SPECTROMETRY

1.1 Mass Spectrometry and Ion Trap Mass Spectrometry

Modern chemical analysis has been developed not only for scientific research, but also for practical applications that influence our daily lives. It plays a significant role in the complex environmental, chemical, agricultural and pharmaceutical industries for use in identification, determination and quantitation of materials of all types. Among numerous analytical methods, mass spectrometry (MS) has become widely employed to elucidate the structures of compounds of all types, including environmental and forensic target compounds, drug impurities, flavors and polymers. Furthermore, it has been used to explore single cells and other planets, due to its unique high sensitivity and high selectivity for determination and quantitation of diverse chemical and biological compounds.[1] In the practice of MS, molecules in a sample are ionized, resultant mass-to-charge ratios (*m*/*z*) of product ions are measured, and mass spectra are produced as plots of intensity versus *m*/*z*. Mass spectra provide information about molecular weights and chemical structures of samples from patterns of the ions produced and their abundances. Extensive libraries of mass spectral data exist for comparison. If target analytes are in a complex mixture, more detailed information can be acquired using tandem mass spectrometry (MS/MS), an experiment in which multiple stages of mass analysis allow the selection of target ion(s) from a mixture of ions, followed by induction of further fragmentation. MS/MS spectra can be used for molecular structure elucidation, structural confirmation, and quantitation, for example in drug metabolism and other studies in the pharmaceutical industry, and for biochemical analyses.

Ion trap mass spectrometry (ITMS) is an important member of the MS family. Its inherently high sensitivity and specificity facilitate many applications,[2] including threat detection,[3,4] investigation of chemical and biochemical systems,[5,6] illicit drug identification,[7,8] planetary exploration,[9,10] environmental monitoring,[11,12] and so on. In the ion trap (IT) device, ions are subjected to electrical forces applied by a radiofrequency (RF) field and trapped within a system of electrodes. A scan function applied to the electrodes allows ions with stable motion in the trap to gain energy, lose their stability and be ejected out of the trap according to *m*/*z*. The principal advantages of the IT in chemical analysis can be summarized as follows: 1) high sensitivity; 2) compact size and mechanical simplicity in a device which is capable of high performance; 3) ease of performance of MS/MS experiments, which can be performed in a single trapping device; 4) less stringent vacuum requirements than other types of mass analyzers; 5) ability to isolate ions by mass to conduct ion/molecule reaction studies; 6) high resolution by way of slow scans (although mass measurement accuracy is relatively poor); 7) ability to select ions of high *m*/*z* using resonance ejection experiments with low frequency; and 8) availability of non-destructive detection using Fourier transform techniques. All of these advantages enhance the attractiveness of the IT mass analyzer, especially for miniaturization of instrumentation and on-site analyses with field portable instrumentation.[3]

1.2 Miniaturization of Ion Trap Mass Spectrometry

The growing demand for on-site analyses using MS for a broad range of applications has encouraged miniaturization of mass spectrometers. In comparison to traditional procedures of chemical analyses, where samples are collected and transported to the laboratory for analysis, the purpose of miniaturization is to bring the laboratory to the sample source. The ultimate goal of miniaturization is to perform complete chemical analyses on-site for convenience, as well as to decrease cost and increase throughput. Therefore, a system for on-site analysis should be affordable, small enough for the application environment, and simple to operate. In comparison, mass spectrometers in the laboratory are typically large, heavy, expensive and power-consuming. The development of miniaturized mass spectrometers must include the following considerations. First, compact size and low power consumption are necessary for handheld instrumentation, for example, at airport checkpoints and waste monitoring sites, and in spacecrafts for planetary exploration. Second, it is critical that operation of the miniaturized device is simple and that data are processed autonomously for *in situ* or real time applications. Third, the costs of ownership and maintenance of these instruments should be low enough for a wide variety of applications. Fourth, the operational procedures should be simplified for end-users.

While the aims for development of lab-scale mass spectrometers have centered around increasing mass range, mass resolution, mass measurement accuracy and sensitivity, the development of miniaturized instruments has aimed at achieving a balance among adequate mass analysis performance, reliable sensitivity, good selectivity, ease of fabrication, and simple operating procedure. Size reduction in mass analyzers surprisingly impacts the design and performance of the resulting mass spectrometers. Various considerations for miniaturization of mass spectrometers are crucial. The first is related to fabrication. It is difficult to maintain nondistorted electrode geometry in practice, which requires high precision machining techniques. The second is related to sensitivity. Smaller volume mass analyzers lead to fewer analyzed ions, which results in loss of sensitivity. The third is related to power consumption. The smaller the mass analyzer, the lower the force required to maintain the same field strength, which results in a reduction in power requirements. The fourth is related to MS/MS capability. For analysis of complex mixtures, MS/MS is very useful to minimize chemical noise and obtain information about the chemical structures of the analytes.

ITMS has distinct advantages over other MS instruments for miniaturization of mass analyzers, for instance, ability to operate under higher pressures than other mass analyzers, less demanding requirements for reducing the instrument size and power consumption, and the capability of performing MS/MS in a single device. Therefore, many groups have developed miniaturized mass spectrometers by using the IT as mass analyzer.[3, 14-17]

1.3 Quadrupole Ion Trap

The quadrupole ion trap (QIT) can function both as an ion storage device in which either positively charged or negatively charged gaseous ions can be confined for a period of time, and as an MS with large mass range, variable mass resolution, and high sensitivity. It is one of a number of devices that utilize trajectory stability as a means to separate ions according to *m*/*z*. Among the other devices are the quadrupole mass filter, cylindrical ion trap, linear ion trap, rectilinear ion trap, and toroidal ion trap.

1.3.1 Structure of the QIT

The original QIT, introduced by Paul in 1953,[18] also called the Paul IT, consists of a hyperbolic ring electrode between two virtually identical hyperboloidal end-cap electrodes, which form a chamber within which ions can be confined, as shown in Figure 1.1. One end-cap electrode, which resembles a small inverted saucer, contains the entrance aperture through which electrons and/or ions can be gated periodically, while the other is the exit electrode through which ions pass to a detector. The ring electrode is symmetrically positioned between the two end-cap electrodes. The r_0 dimension is the radius of the ring electrode in the central horizontal plane and $2z_0$ is the closest distance between the two end-cap electrodes measured along the axis

Figure 1.1. Photograph of electrodes for a QIT.

of the IT. The three electrodes are truncated for practical purposes; however, in theory they extend to infinity so as to produce an ideal quadrupole potential distribution for the confinement of ions.

1.3.2 Mathieu equations

An electrostatic field in free space must obey Laplace's equation, $\nabla^2\Phi = 0$. A time-dependent quadrupolar-shaped electric field in the IT is produced by a megahertz RF voltage applied to the ring electrode with the end-cap electrode grounded. The force on an ion is proportional to its distance from the center of the device, and ions of appropriate *m*/*z* ratios have stable trajectories within the chamber and can be trapped for many seconds.[19] The mass stability of ions in the axial direction in the IT is derived from Laplace's equation and governed by the Mathieu equations

$$a_z = -\frac{16eU}{m\left(r_0^2 + 2z_0^2\right)\Omega^2} \tag{1.1}$$

$$q_z = \frac{8eV}{m(r_0^2 + 2z_0^2)\Omega^2} \qquad (1.2)$$

where a_z and q_z are the two Mathieu stability parameters in the axial direction, e is the charge of the ion, m is the ion mass, r_0 and z_0 are, respectively, the radial and axial dimensions of the IT, V is the zero-to-peak amplitude of the RF voltage applied to the ring electrode, Ω is the angular component of the RF drive frequency which is expressed in radians per second instead of hertz, and U is the direct current (DC) offset applied to the ring electrode.

The Mathieu equations for the radial component of ion motion are

$$a_z = -2a_r \quad \text{and} \quad q_z = -2q_r \qquad (1.3)$$

The solutions to the Mathieu equation can be interpreted in terms of trajectory stability (and instability) in the radial, or r, and axial, or z, directions within the electric field of the QIT. The stability regions corresponding to stable solutions of the Mathieu equation in the r- and z-directions simultaneously compose the stability boundary. Ions can be stored in the IT provided that their trajectories are stable within the boundary. Solutions out of the boundary represent conditions at which ions are ejected from the device and either lost or detected externally. The stability boundary, as shown in Figure 1.2, intersects with the q_z axis at $q_z = 0.908$; this working point represents the ion of lowest mass/charge ratio (low-mass cutoff, LMCO) which can be stored in the IT for given values of r_0, z_0, V, and Ω.

1.3.3 Secular frequencies

The trajectory of an ion in a three-dimensional (3D) IT has the general appearance of a Lissajous curve composed of two fundamental frequencies, $\omega_{r,0}$ and $\omega_{z,0}$, of the secular motion. Planar motions of the trapped ions occur in a plane, shown in a simulation by the ITSIM program.[20] There exists a group of higher-order (n) frequencies in the trajectory, described by $\omega_{r,n}$ and $\omega_{z,n}$. These secular frequencies, also called tickle frequencies, are given by

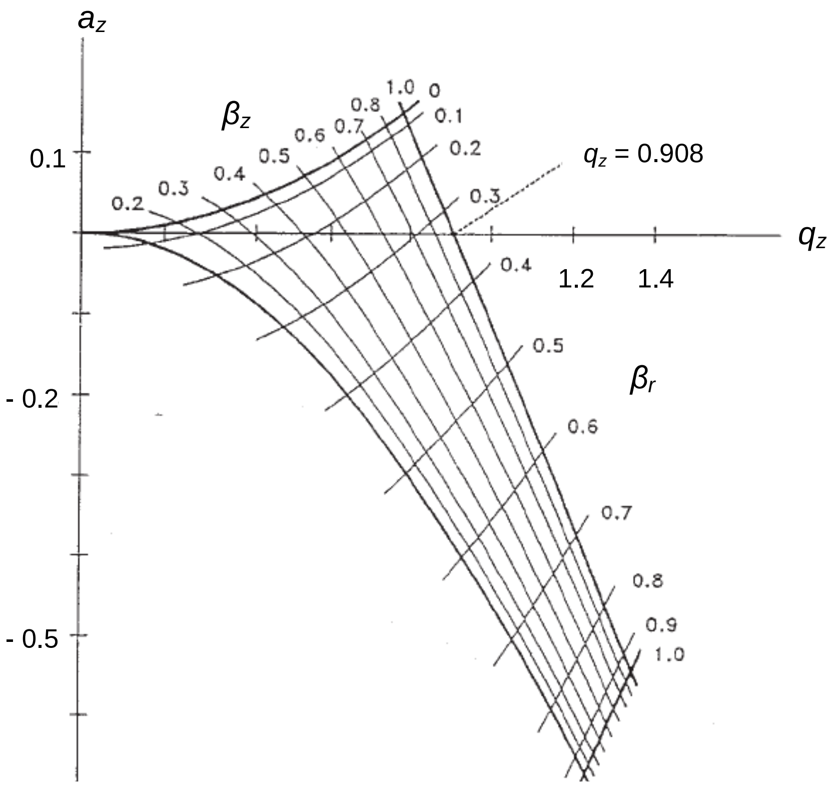

Figure 1.2. Stability diagram for the region of simultaneous stability in both the axial and radial directions near the origin for the 3D quadrupole IT. The iso-β_r and iso-β_z lines are shown in the diagram.

$$\omega_{u,n} = \left(n + \frac{1}{2}\beta_u\right)\Omega \qquad 0 \le n < \infty \tag{1.4}$$

and

$$\omega_{u,n} = -\left(n + \frac{1}{2}\beta_u\right)\Omega \qquad -\infty < n < 0 \tag{1.5}$$

where

$$\beta_u \approx \sqrt{\left(a_u + \frac{1}{2}q_u^2\right)} \tag{1.6}$$

for $q_u < 0.4$. Normally, the higher-order secular frequencies are of little practical significance.

1.3.4 Pseudopotential well model

The ion trajectory can be regarded as a combination of a low-frequency (secular) oscillation superimposed upon a high-frequency (driving RF) ripple. The pseudopotential well model was formulated from this characteristic by Wuerker and Dehmelt.[21,22] It is essentially assumed that, at low values of β_u, the high-frequency ripple is neglected, and the motion of trapped ions along the r and z directions can be approximated to that of charged particles acting in simple harmonic motion in a parabolic potential well. The depth of the well is related to the trapping parameters a_u and q_u and, thus, to the experimental operating conditions of the device. From this pseudopotential well model, the density of trapped ions can be estimated, and their kinetic energies (ignoring the collisional effects) can be evaluated.

For $q_u < 0.4$, the pseudopotential $\overline{D}_z$ acting in the z direction and $\overline{D}_r$ acting in the r direction can be expressed as

$$\overline{D}_z = \frac{m z_0^2 \Omega^2}{16e} q_z^2 \qquad \text{and} \qquad \overline{D}_r = \frac{m r_0^2 \Omega^2}{16e} q_r^2 \tag{1.7}$$

If $r_0^2 = 2z_0^2$ for the standard ideal quadrupole device, substitution of Eq. 1.2 for q_z and Eq. 1.3 for q_r in Eqs. 1.7 gives

$$\overline{D}_z = \frac{1}{8} V q_z \qquad \text{and} \qquad \overline{D}_r = \frac{1}{8} V q_r \tag{1.8}$$

The pseudopotential well model offers a fairly simple picture of the motion of ions held within the QIT, and also gives an estimation of the effects of space charge and maximum ion density in the trap. The space charge can be assumed to distribute uniformly over the whole trapping field, and then act as an effective DC voltage increment, which causes shifts in the a values which, in turn, leads to displacements of the boundaries of the stability diagram and, consequently, of the secular frequencies.[23]

Every ion which is placed in the IT must modify the fields experienced by ions already present. Eventually, the space charge limit is reached and the maximum number of ions are held in the chamber when the trapping potential is balanced with the repulsive electrostatic potential arising between the trapped ions.[24,25] It is assumed that this trapping potential is provided by the pseudopotential derived above. The maximum ion density, $N_{\max}$, is calculated from

$$N_{\max} = \frac{3}{\pi} \frac{V^2}{m\left(r_0^2 + 2z_0^2\right)^2 \Omega^2} \tag{1.9}$$

or, after making the substitution from Eq. 1.2

$$N_{\max} = \frac{3}{64\pi} \frac{m\Omega^2}{e^2} q_z^2 \tag{1.10}$$

From these equations, when the IT is operated at a fixed RF potential, V, and fixed frequency, Ω, the maximum number of trapped ions, $N_{\max}$, of a given species is inversely proportional to its mass. Conversely, when working at a fixed q_z value, $N_{\max}$ is directly proportional to the mass of the ion and inversely proportional to the square of its charge.

1.3.5 Higher order field components

In a real QIT, the operation of the system is dependent on certain electrical and geometrical limitations. The facts that the RF drive potential may not be strictly sinusoidal, that the electrodes do not extend to infinity, that the spacing between the electrodes may be inaccurate, that there may be imperfections in the shapes or precision of the electrode surfaces, and that one or more holes are drilled through the electrodes in order to admit electrons or ions and to eject ions for detection, induce the presence of superimposed higher order field components in the IT. These nonidealities may lead to mass shifts such that mass spectra of the ejected ions exhibit peaks not appearing at the correct assignment of m/z values, which produces "black holes" or "black canyons" or regions of instability embedded within the stability diagram where ions are not trapped.

The electric field in the QIT is a system with axial symmetry. The solution of Laplace's equation for the derivation of the potential in a QIT in spherical polar coordinates (ρ, θ, φ) has the general form

$$\phi(\rho,\theta,\varphi)=\phi_0\sum_{n=0}^{\infty}A_n\frac{\rho^n}{r_0^2}P_n(\cos\theta) \tag{1.11}$$

where A_n are arbitrary coefficients and $P_n(\cos\theta)$ means a Legendre polynomial. When $\rho^n P_n(\cos\theta)$ is written in cylindrical coordinates ($r = (x^2 + y^2)^{1/2}$, z), Eq. 1.11 becomes

$$\phi_{r,z}=\phi_0\left(A_2\frac{r^2-2z^2}{2r_0^2}+A_3\frac{3r^2z-2z^3}{2r_0^3}+A_4\frac{3r^4-24r^2z^2+8z^4}{8r_0^4}\right.$$
$$\left.+A_5\frac{15r^4z-40r^2z^3+8z^5}{8r_0^5}+A_6\frac{5r^6-90r^4z^2+120r^2z^4-16z^6}{16r_0^6}+\cdots\right) \tag{1.12}$$

The values of n = 0, 1, 2, 3, 4, 5, and 6 correspond to the monopole, dipole, quadrupole, hexapole, octopole, decapole, and dodecapole components, respectively, of the potential field, ϕ, in proportions according to their respective weighting factors, A_n. Higher-order field components such as hexapole and octopole can play important roles in the operation of modern IT mass spectrometers. The consequence is that the components of the RF field amplitude arising from the higher order fields are nonlinear in the r and z directions. Therefore, the secular frequencies of oscillation are not constant and become amplitude dependent for certain field parameters, and the ion trajectories in the r and z directions become amplitude dependent and are coupled with each other for the higher order fields.

1.3.6 Motion of trapped ions

In the operation of an IT, helium is used as a buffer gas at ~10^{-3} Torr to improve both the resolution and sensitivity[26] due to viscous damping by collisions between the ions and the helium buffer gas atoms. The ions collapse to the center of the trap in both the radial and axial directions so that ions do not experience any higher order fields, since the effects of higher order fields are negligible at the trapping center. Moreover, as the amplitude of the RF drive potential is increased, the buffer gas damping effect opposes the increase in maximum displacement of ions, and they remain tightly bunched and can pass through the exit holes in the end-cap electrodes. The trapped ions change little in momentum and hardly scatter in collisions with low-mass damping atoms. This effect of buffer gas in optimizing the performance of IT mass spectrometers is called collisional cooling. The optimization is affected by the pressure of the buffer gas, the operating q_z value, and the time for collisional cooling.[27]

During external injection of ions into the trap, the holes in the end-cap electrodes weaken the RF trapping field near the holes, which especially affects ions with large axial trajectories. The holes cause RF field penetration out toward the incoming ions, and increase the percentage of trapped ions, especially for slower moving high-mass ions, as a function of q_z at the time of injection.[28]

Several methods exist for mass analysis in an IT, such as mass-selective instability scan,[26] resonance frequency scan ejection, and mass-selective storage. For the mass-selective instability scan, the amplitude of the RF voltage is increased, and this causes ions of increasing *m/z* to become unstable as their excursions within the quadrupolar potential well eventually take them beyond the physical bounds of the device. At this point, ions are ejected in mass sequence from the device through perforations in an end-cap. An additional “supplementary alternating current (AC) potential" with a frequency equal to the secular frequency, ω_z, (Eq. 1.4 and 1.5) can be applied along the axis of the IT, which couples resonantly with the fundamental secular frequency of ions that have the corresponding value of β_z. These ions will, therefore, receive additional energy, their trajectories will expand, and ultimately they will pass through holes in the end-cap electrodes. For frequency scan resonance ejection, the amplitude of the RF voltage is kept constant, and the frequency of the supplementary AC potential is increased or decreased. Ions with decreasing or increasing *m/z* are coupled resonantly with the frequency scan and eventually eject out of the device.

This supplementary AC potential can be connected to the IT in different ways. The most common way is dipolar coupling, in which the two AC signals, equal but out-of-phase, are applied to each of the end-cap electrodes. The other method is monopolar coupling where a single AC signal is connected to one end-cap electrode with the other end-cap electrode held at ground.

1.3.7 Simulation of ion trajectories

Simulation of ion trajectories in a QIT permits visual measurement of ion motion with the applied drive potential.[29] The simplest simulation is to calculate the trajectory of a single ion in an ideal quadrupole field without buffer gas. Single ion trajectory simulation can be done at any a_z, q_z coordinate or working point within or beyond the stability diagram to show different secular frequencies or the ion hitting the electrodes. The effects of ion/neutral collisions are incorporated to simulate the collisional process of momentum dissipation, leading to ion focusing to the center of the IT. Thereafter, resonant excitation and resonant ejection of ions can also be simulated. Then, the higher-order terms can be added to the quadrupole field to affect ion motion in the IT. The investigation of spatial and energy distributions can be simulated by simultaneous calculation of the trajectories of more than 600,000 ions. A wide range of *m*/*z* ratios can be accommodated to permit simulation of mass spectra and ion kinetic energy distributions, and evaluation of space-charge effects. Ion trajectories from the ion source through the IT to the detector can now be simulated together with the processes of charge exchange, ionization, cluster ion formation and ion fragmentation. All of the above simulations can also be repeated in traps with different geometries.

Three computer programs have been extensively used for the simulation of ion trajectories. They are SIMION, ITSIM and ISIS. From a comparison of the performance, design, and operation of the three programs,[29-31] it was found that there are many similarities and some differences. The greatest similarity was found for the simulation of a single ion in a collision-free system; calculations of spatial trajectory components, kinetic energies and secular frequencies were very close. The differences occur in determining ion-trapping efficiency due to random effects such as collisions of ions with buffer gas atoms and the different approaches to field calculation.

1.3.8 Concerns about miniaturization of the QIT

Although more limited in resolution and mass accuracy compared to FTICR and TOF instruments, QITs offer some important advantages as miniature mass analyzers, such as high sensitivity, operation at higher pressure than any other type of analyzer, and multiple stages of MS in one single analyzer.

From Eq. 1.2, the miniaturized QIT requires lower power to operate, but this must be balanced with the performance of the mass analyzer, including mass resolution and mass analysis efficiency. Using a lower RF voltage decreases the trapping potential well depth, which causes lower ion trapping efficiency and poorer mass resolution. Often, RF signals of higher frequency are used for the characterization of miniature IT mass analyzers to improve performance because of an increase in the trapping potential well depth.

When a miniature QIT was constructed with half or quarter radius,[32] the shape of the hyperboloid trapping electrodes required high machining precision. Any imperfections in the shapes and inaccuracies in the precision of the electrode surfaces degrade the performance of the miniature IT, and even result in complete loss of ion signal.[33] Cylindrical quadrupole ion traps (CITs)[34,35] are much simpler to machine than QITs, and can therefore be miniaturized more easily because of their flat end-cap electrodes and barrel-shaped ring electrode.

Miniature IT mass analyzers are also limited in ion trapping capacity since half or quarter dimensions lead to quarter- or eighth-size mass analyzers. The smaller trapping volume results in lower sensitivity due to fewer ions trapped and poorer resolution due to space charge problems. An effective means to address the trapping capacity problem is to increase the trapping volume by using an array of traps with identical dimensions. For example, parallel arrays of small-sized CITs have been used.[36] The other way is to modify the geometry of the mass analyzer to increase the trapping capacity as well as to keep small dimensions. Two alternative geometries, linear and toroidal,[37,38] both allow ions to be trapped along a line instead of at a point, as occurs in a 3D IT.

1.4 Cylindrical Ion Trap

The CIT was derived as a simplified version of a Paul trap or QIT to confine charged particles for examination of charged species, study of their reactions with neutral species, and determination of the *m*/*z* ratios of such species. The CIT has a simplified geometry, consisting of a cylindrical electrode and two planar end-caps instead of the hyperbolic ring electrode and two hyperboloidal end-cap electrodes in the QIT. Each end-cap plate has one center hole for entrance or exit of ions. Simplicity of fabrication of CITs permits investigation of their ion-trapping properties as functions of size and geometry. Therefore, the general direction of research on CITs has been toward smaller size, or miniature CITs.

The CIT has received much attention from a number of research groups. Most of the interest in cylindrical traps has been for use as a simple ion storage device.[40,41] Once mass-selective axial ejection had been exploited with the QIT, thoughtful reflection on the application of the same technology to CITs was made, and Cooks *et al*. used cylindrical traps in the standard mass-selective instability mode of operation for mass analysis.[17,34 ,42] Multiple-stage mass analysis has also been demonstrated using a mini-CIT.[39]

The main driving force for the development of CITs is the increasing interest in field-portable analytical instrumentation for on-site analysis of toxic pollutants and detection of chemical warfare agents.[43] A CIT can be easily fabricated from a polished metal cylinder with an internal radius of a few millimeters and two flat round discs with suitable holes for admission of electrons or ions and ejection of ions. It is capable of storing an adequate mass range of ions,[39] can be operated as a portable mass spectrometer with tandem MS capabilities, and has good sensitivity. The performance of a CIT depends strongly on its structure and geometry. An optimization procedure was developed based on field calculations and simulations of ion motion in the CIT field, and experimental results were reported to confirm the enhanced performance.[44]

A miniature CIT mass spectrometer was developed by 1st Detect for field portable and handheld applications.[45] The miniature CIT mass analyzer accounts for < 1% of the total volume and weight of the instrument and, thus, the major miniaturization effort was directed to the accessory components. The weight of the device was 15 lbs with supplied battery, or 12 lbs when operated on 12/24 VDC or 110 / 220 VAC. The vacuum system in the mass spectrometer is normally large and heavy, and consumes considerable power. However, in a miniature IT, the oscillation of an ion at a certain secular frequency is smaller than in an IT of standard size. As a result, ions experience fewer collisions with buffer gas per RF cycle at a given pressure. Therefore, the miniature CIT can be operated at a higher pressure than a normal IT, and the pumping requirements are reduced. Electron impact (EI) ionization was used for the detection of volatile compounds. A miniaturized membrane inlet system was designed for gaseous and liquid samples. Mass spectra were recorded in 2 seconds with unit mass resolution.

The miniature CIT array mass spectrometer was developed in order to meet the demands for high-throughput analyses,[46] to increase the trapping volume for micro-sized mass analyzers that were made from modern microfabrication techniques,[47,48] and to simplify the IT control electronics and avoid the use of an RF ramp to decrease the power consumption.[49]

In the array for high throughput, there are four mini-CITs of the same size with barrel electrodes of 2.5 mm internal diameter. Each CIT has its own inlet system, filament assembly, and small electron multiplier, all within a common vacuum manifold, operated with a single set of control electronics. Therefore, the compounds examined in the four channels may differ from each other, and the channels can be operated simultaneously for high-throughput experiments.

In an array microfabricated using standard integrated circuit (IC) and micro-electro-mechanical system (MEMS) fabrication techniques, 10^6 traps with radius of 1 μm have been arrayed in parallel in a 0.25 cm^2 area. If only 10 % of the traps could be populated with an ion of interest, such an array would have a spectral charge density equivalent to a normal QIT, thereby regaining the signal with the sensitivity seen in conventional size traps. The benefit of CITs with dimensions on the order of a few micrometers is that operating voltages need to be only a few tens of volts, which is an appealing feature on which a truly handheld mass spectrometer could be based.

In an array with simplified control electronics, the individual traps were of different sizes, so that when the array was operated with a fixed RF potential, ions of different masses or mass ranges were stored in separate traps. The RF and DC voltages applied to the ring electrodes were kept constant, thus, simplifying the operating electronics and improving the miniaturization process. The CIT array was designed so that all ions could be ejected simultaneously using a fast DC pulse[50] applied to the flat end-cap entrance electrode in each trap. A position-sensitive detector was used to detect the ejected ions from each of the array elements and produce the ion intensity versus CIT from which the signal was generated; then, the full mass spectrum could be constructed. By employing an array of simple traps with different dimensions, in which mass analysis can be performed without the need to scan the RF voltage, significant simplification in the electronics system can be achieved, which is believed to represent a first step to a portable, handheld IT mass spectrometer for *in situ* analysis.

1.5 Quadrupole Mass Filter

A quadrupole mass filter (QMF) consists of four parallel metal rods arranged as in Figure 1.3. To reduce costs and to simplify construction, arrays of electrode rods in modern QMFs are fabricated as round instead of hyperboloidal shape.[2] A good approximation to a quadrupole field can be obtained when the value of the radius (r_e) of each rod was found in the range of $r_e = 1.12 \times r_0$ to $r_e = 1.13 \times r_0$, where r_0 is half of the shortest distance between the opposite rods,[51] as shown in Figure 1.3.

Each pair of opposite rods is electrically connected: one pair of rods having an applied potential of $(U+V_0\cos\Omega t)$ and the other two having a potential of $-(U+V_0\cos\Omega t)$, where U is a DC voltage and $V_0\cos\Omega t$ is an AC voltage. The applied voltages establish a two-dimensional (2D) quadrupole field in the *x*-*y* plane and affect the trajectory of ions traveling down the flight path in

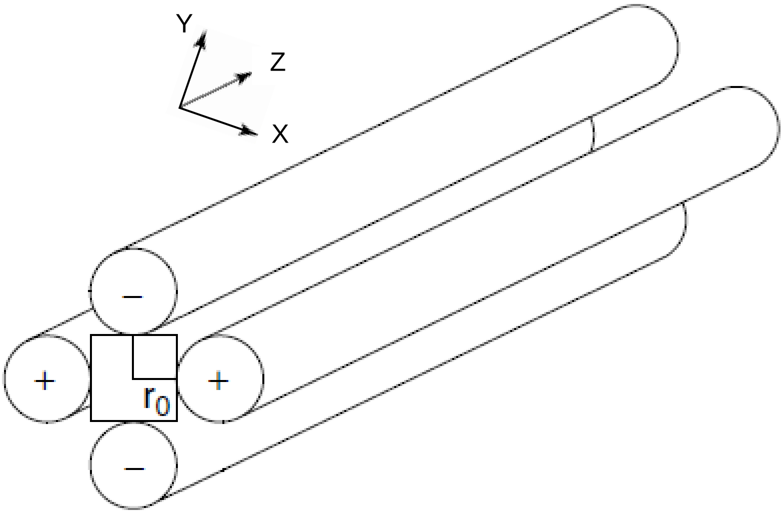

Figure 1.3. Quadrupole mass filter. Ions enter and migrate along the z direction, while they oscillate in the x-y plane. Only ions with stable trajectories travel the length in the z direction of the QMF to the detector.

the *z* direction centered between the four rods. While traveling in the *z* direction, the ions also oscillate in the *x*-*y* plane due to the potentials applied to the rods. For given DC and AC voltages, only ions of a certain *m*/*z* ratio have a stable trajectory and pass through the entire length of the quadrupole filter; all other ions deviate from the *z* axis and hit the rod electrodes. Therefore, a QMF can be operated so as to transmit either all ions or ions with a certain range of *m*/*z* ratio and to focus them at the exit aperture.

During the operation of a QMF, the potential applied to the vertical rods and the potential applied to the horizontal rods are out of phase with each other. The potential along the *z* axis centered between the four rod array is generally zero.

The trajectory stability of ions in the *x*-*y* plane in a QMF is governed by the Mathieu equations in the *x* direction

$$a_x = \frac{8eU}{mr_0^2\Omega^2} \tag{1.13}$$

$$q_x = \frac{-4eV}{mr_0^2\Omega^2} \tag{1.14}$$

and in the *y* direction

$$a_y = -a_x \tag{1.15}$$

$$q_y = -q_x \tag{1.16}$$

where a_x, q_x and a_y, q_y are the two Mathieu stability parameters in the *x* and *y* directions, respectively, *e* is the charge of the ion, *m* is the ion mass, $2r_0$ is the shortest distance between the opposite rod electrodes, *V* is the zero-to-peak amplitude of an RF potential oscillating with angular frequency Ω in radians per second, and +*U* is a DC voltage applied to one pair of electrodes while a DC voltage of –*U* volts is applied to the other pair of electrodes.

The solutions to the Mathieu equations can be interpreted in terms of ion trajectory stability (and instability) in each of the *x* and *y* directions of confinement within the quadrupole field. The stability regions correspond to stable solutions of the Mathieu equation in the *x* and *y* directions simultaneously, as shown in Figure 1.4. Only the upper part of the whole stability region is shown, since it is symmetric about the q_u axis. When an ion's a_x, q_x coordinates lie within the stability region, its a_y, q_y coordinates must also necessarily lie within the stability region.

When a QMF is operated with only an RF potential, the rod array allows the transmission of all ions above a fixed *m*/*z* through the device. Normally, the RF voltage is either fixed or increased gradually in order to enhance the efficiency of transmission of ions of higher *m*/*z* ratio.

The mass selectivity of a QMF is realized by varying the magnitudes of the DC and AC or RF voltages applied in a constant ratio to each pair of rods. Light ions (low *m*/*z*) are able to follow the AC component of the field. In the *x*-*z* plane, the RF potential greatly affects these ions.

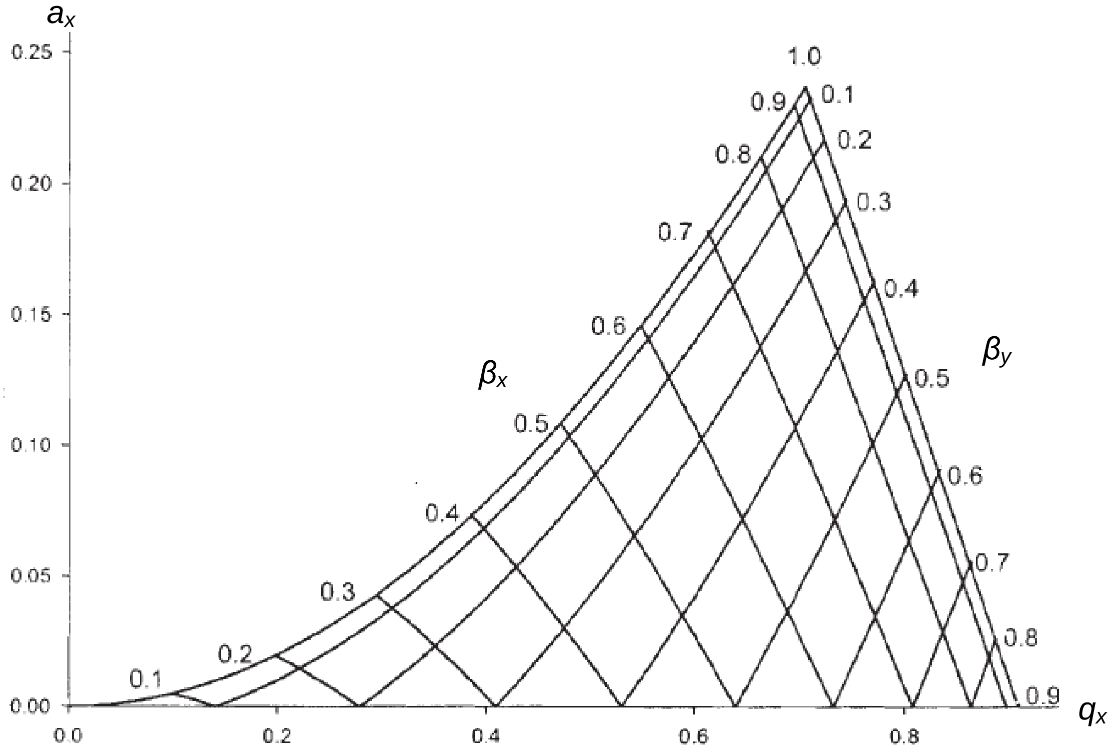

Figure 1.4. Stability diagram of linear quadrupoles, such as the QMF and LIT.

They will stay in phase with the RF drive potential, gain energy from the field and oscillate with a large increasing amplitude until they are lost either via contact with the rods or ejection from the quadrupole rod assembly. Heavier ions are less affected by the RF drive, and remain near the center of the four rod assembly, and are emitted through the exit aperture at the downstream end of the rod array. Therefore, the *x*-*z* plane is a high-mass pass filter. On the other hand, in the *y*-*z* plane, both heavy and light ions are drawn toward the negative DC potential of the rods. However, light ions are refocused toward the center by the RF drive if their magnitudes are such as to correct the trajectories whenever their amplitudes tend to increase. Therefore, the field in the *y*-*z* plane acts as a low-mass pass filter. By suitable choice of an appropriate DC/RF ratio, the two filters can overlap so that only ions within a small range of *m*/*z* ratios have stable trajectories while traveling in the *z* direction to the detector.

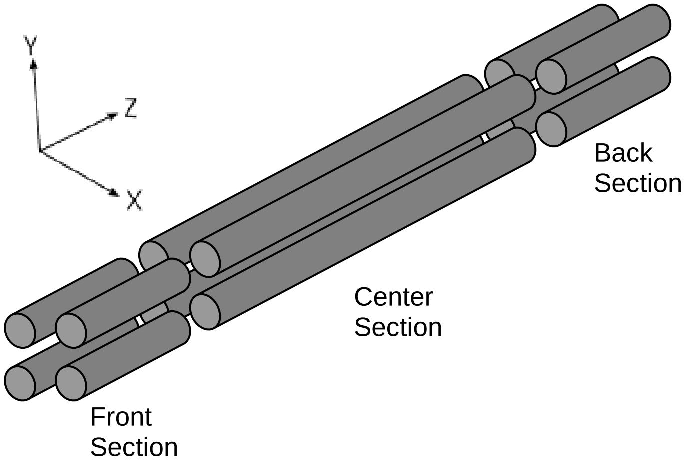

Figure 1.5. Electrodes of a linear quadrupole IT mass spectrometer.

By varying the amplitude of the RF voltage, V, or DC voltage, U, the QMF provides a convenient mass filter which can be tuned to the desired mass. The mass selectivity, i.e., resolution, can be varied electronically by simply adjusting the RF/DC ratio. Simultaneously, by ramping both the DC and RF potentials with fixed ratio of U/V, an entire mass spectrum of m/z can be scanned,[52,53] and the mass resolution can be determined by the slope of U/V.

1.6 Linear Ion Trap

A linear ion trap (LIT) has hyperbolic (or, in simpler versions, cylindrical) rod profiles, similar to QMFs, but with four rods in each of three axial sections.[54,55] In practice, round rod electrodes are widely used because they are easier to manufacture, as shown in Figure 1.5. These rod sections are positioned adjacently to avoid fringe field distortions of the trapping and excitation fields. In an LIT, ions are confined within the center section through a combination of a radial quadrupolar field by the RF voltage and axial potential created by raising the potentials on the two end sections. In comparison to 3D QITs, linear traps have higher injection efficiencies and higher ion storage capacities.[53] The trapping volume of the trap can be increased simply by making it longer. Thus, the problem of space charge repulsion and accompanying deterioration of mass resolution and shift of mass assignment is experienced only at greater ion loading. Virtually all advantages of the 3D QIT are retained in the LIT, such as collisional focusing, resonant excitation and ejection, tandem MS, and variation of mass resolution as a function of mass-selective ion ejection scanning rate. In addition to being combined with other mass analyzers[56-58] in hybrid instruments to isolate ions of selected *m*/*z* ratios and to perform tandem MS experiments, they can also be operated as stand-alone mass spectrometers.[59,60]

Ions stored in an LIT are subject to a 2D quadrupole field driven by an RF potential and a DC voltage on the rod electrodes in the center section. Mostly, the DC component is zero in the LIT. The trajectory stability of ions in an LIT is governed by the Mathieu equations (same as in the QMF) given by Eq. 1.14 in the *x*-*z* plane and by Eq. 1.15 in the *y*-*z* plane. The 2D stability diagram, which is the same as in the QMF as shown in Figure 1.4, is obtained from the solutions to the Mathieu equations. In the stability diagram, there is a continuum of iso-β_u lines, which are complex functions of a_u and q_u. From β_u, resonant frequencies of the ion motion could be characterized by Eqs. 1.4 and 1.5 as in a QIT. When $n = 0$, the resonant frequency for the *x* direction can be written as

$$\omega_x = \frac{1}{2}\beta_x\Omega \tag{1.17}$$

Thus, ions trapped in an LIT can be excited resonantly by applying an auxiliary AC signal to two opposing rod electrodes. Excited ions can dissociate following collisions with molecules of buffer gas, or can be ejected out the LIT, which is similar to that in the QIT. Trapped ions can be ejected mass-selectively so as to isolate a given species in the LIT, or to give a mass spectrum.

Similar to a QIT, 2D multipole fields are well known, which are used for trapping and manipulating ions.[61] The ratios of round rod electrode radius, r_e, to field radius, r_0, give approximations for higher order fields, so does the relative position of one pair of rods to the other.[62] The ratio which is optimum for mass analysis in a linear quadrupole field is approximately $r_e/r_0 = 1.13$.[63] Ion motion in the x and y directions is strongly coupled in the higher multipole fields. The frequencies of ion oscillation and the trajectories of trapped ions depend on the initial conditions. Therefore, there is no stability diagram for ion motion in higher order fields.

As a stand-alone mass spectrometer, the LIT can scan mass spectra with mass selective radial ejection.[55] Ions are confined radially in the center section by the RF voltage and axially by the DC potential on the front and back sections. Ions are ejected through a slot in a rod in the direction of the x axis (X rod). To compensate for the field distortions induced by the slots, these rods are moved 0.75 mm away from the center. Dipole excitation with auxiliary AC voltages on the X rods can be used to isolate, excite, and eject ions.

Ions can also be ejected axially from an LIT in a mass selective manner. Ions flow through an RF only quadrupole field in an LIT without trapping and produce mass spectra.[64] Ions receive increased energy in the x and y directions with q values close to the stability boundary limit ($q = 0.908$) when the RF voltage is ramped. Ions overcome a stopping potential applied at the end section of rod electrodes when ions get enough energy at the fringing field. Mass spectra are produced by scanning the amplitude of the RF voltage to cause ions with different m/z ratios overcome the stability boundary. Mass resolution can be improved by applying a small resolving DC voltage between the rods by unbalancing the RF.[65]

An excitation frequency can be applied to the exit section rods as dipole excitation, or between a pair of rods as quadrupole excitation.[66] Ions exciting with their resonant frequency at the fringing fields accumulate kinetic energy, or are ejected by overcoming the stopping potential at the trap exit. By scanning the excitation frequency, ions with different *m*/*z* can be ejected to produce a mass spectrum. Alternatively, the excitation frequency can be kept constant and the amplitude of the driving RF ramped to push ions with different *m*/*z* into resonance. The RF amplitude increases proportionally to the *m*/*z* value of the ion being ejected.

1.7 Rectilinear Ion Trap

A rectilinear ion trap (RIT) has been constructed and characterized by Cooks *et al*.[67-69] It combines the advantages of higher injection efficiencies and higher ion storage capacities in an LIT with the geometric simplicity of a CIT. Round rod electrodes were used in LITs for simplification, with the addition of a DC trapping field to the separated rod sections at the both ends of the LITs discussed above. The geometry of the LITs can be simplified to arrive at the RIT by using six planar sheets of metal or polymer[70,71] to give a six-electrode cubic structure.

The simple geometry of an RIT consists of three electrode pairs in the *x*, *y*, and *z* directions. The pairs of electrodes in the *x* and *y* directions are rectangular plates of high aspect ratio with length of 40 mm, 4–5 times the width, and they are arranged in a rectangular array. On each *x* electrode, a slit is centrally located through which ions can be ejected to a detector. There is a rectangular plate at each end of the *x*, *y* electrodes forming the *z* electrodes.

An RIT can be operated as an LIT by application of voltage, *V*, to the pair of electrodes in the *x* direction and – *V* to the pair in the *y* direction, with the end plates grounded. Mass spectra can be produced by scanning *V*, and ions can be ejected through the aperture in the end plate. Similarly, the six-electrode cubic structure can be operated as a 3D IT by applying the same RF drive potential to all four side electrodes and a DC voltage to the *z* electrodes. Ions are trapped in the quadrupolar RF field between the *x*-*y* planes, and stopped by the DC potential well along the *z*-axis. Mass analysis of trapped ions is performed using standard mass-selective instability by scanning the RF amplitude. The ions can be scanned out of the RIT through the slits in the x electrode. In addition, a supplementary AC dipolar frequency can be applied between the two x electrodes to achieve resonance ejection during the RF scan.

It is relatively easy to modify the essential dimensions of the RIT to explore variations in RIT performance. The magnitudes of the half-distance between the electrodes in the x dimension (d_x) or the one in the y dimension (d_y) can be varied independently so as to explore the effects of both physical size and ratio d_x/d_y on the performance of the RIT. The gaps between adjacent electrodes and the width of the slits for ejection also greatly influence ion ejection.[72] CreatePot was used to calculate the higher-order fields for various RIT geometries. The optimized RIT with d_x = 5.0 mm and d_y = 3.8 mm has a quadrupole field coefficient, $A_2 = 0.6715$, an octopole field coefficient, $A_4 = 0.0832$, and a dodecapole field coefficient, $A_8 = -0.1260$.

The stability diagram is an important characteristic of any quadrupole device. The variation of the stability diagram for the RIT was investigated as a function of the d_x/d_y ratio.[68] An ion species of m/z 105 was isolated at several values of the RF drive potential amplitude, from which the corresponding values of q_x could be determined by Eq. 1.14. At each q_x value, a DC potential was applied and adjusted until the ion ejection signal disappeared, and the corresponding a_x boundary value was determined. The complete stability diagram could then be plotted. The stability diagram for an RIT of $d_x = d_y$ = 5.0 mm is symmetric about the q_x axis, just as is the stability diagram for the QMF and the LIT. The stability diagram for an RIT of d_x = 5.0 mm and d_y = 3.8 mm is markedly asymmetric and resembles the stability diagram for a truncated QIT. As a result, the secular frequencies in the y direction are shifted to higher values. During resonant excitation by ramping the RF potential amplitude, ions come into resonance with ω_x before they come into resonance with ω_y, and so they are ejected preferentially in the x direction.

RITs have higher injection efficiency when ions are axially injected into the RIT,[74] compared with ~ 5 % for 3D ITs.[28] Therefore, external ion sources are suitable for coupling to RITs, especially atmospheric pressure ionization (API).[75,76] A direct leak atmospheric pressure interface used a capillary to directly connect the ambient air to the vacuum region of the RIT. However, ion transfer was limited by the low conductance of the capillary. The barrier to high performance was overcome with the development of a discontinuous atmospheric pressure interface (DAPI).[77] DAPIs have been characterized with electrospray ionization (ESI) ,[78,79] desorption electrospray ionization (DESI)[80] and low-temperature plasma (LTP)[81] probe ionization, and use a pinch valve to control the opening of an interface to the vacuum chamber. The introduced ions are trapped in the RIT while the introduced gas increases the pressure for ~20 ms, and then the gas is pumped away. Mass analysis could be performed after a delay of ~300 ms until the pressure dropped into the low millitorr range. Chemical analysis has been performed for various organic compounds and mixtures for amino acids, peptides, and proteins in solution.[15,77,82]

The tandem MS capability of the optimized RIT has been demonstrated using RF/DC isolation and SWIFT (stored waveform inverse Fourier transform) isolation.[83,84] In the MS/MS experiments, an analytically useful ion/molecule reaction[85] was performed in the RIT. The molecular ion of a chemical warfare simulant, dimethyl methyl phosphonate (DMMP), was isolated and then dissociated to form a phosphonium fragment ion (*m*/*z* 93), which included an Eberlin transacetalization reaction and electrophilic addition.

In order for simultaneous high-throughput analysis of multiple samples, a multi-channel RIT mass analyzer was designed and constructed.[86-88] The system consisted of four parallel API sources, four RIT mass analyzers, four sets of ion optic elements, and four dynode detectors. The four parallel systems were assembled in a single vacuum manifold with a common vacuum system, operated by a common set of control electronics, including a single RF power supply and transformer coil. Each of the channels could analyze either positive or negative ions with a choice of ionization method. This improved the information about analytes from an experiment with simultaneous data acquisition capabilities from all four channels. An automatic gain control (AGC) system for each channel was used to independently control the ion population in each trap. In experiments, two principal analytical modes could be used. In one mode, the same sample is tested in all of four channels using different ionization methods to better interrogate the sample. In the other operation mode, different samples are analyzed in all four channels with the same ionization method to provide higher throughput analysis.

1.8 Toroidal Ion Trap

The concept of the toroidal IT came about by rotating a 2D QIT cross-section about an axis at the edge of the ring electrode rather than its central axis, as shown in Figure 1.6. It was obvious that the toroidal IT had a larger volume, as it maintained the main dimensions (r_0 and z_0) which governed the operation of the IT, and there was only a single storage region instead of an array of traps. The toroidal IT is similar in nature to a device constructed by Church[89] in which linear quadrupoles were bent into closed circles and demonstrated for storage of $^3He^+$ and H^+ ions for several minutes. Similar to other groups,[90,91] they also described traps with circular quadrupole geometries for storage of ions. A similar curved quadrupole rod set was used in the TSQ-70 triple quadrupole mass spectrometer from Finnigan-MAT as a transmission device.[92]

The symmetrical toroidal IT was built by rotating the 3D IT quadrupole cross-section about an edge axis. The mass resolution was poor, and the shapes and intensities of the peaks were strongly dependent on the ejection *q* values because of distortions to the quadrupole

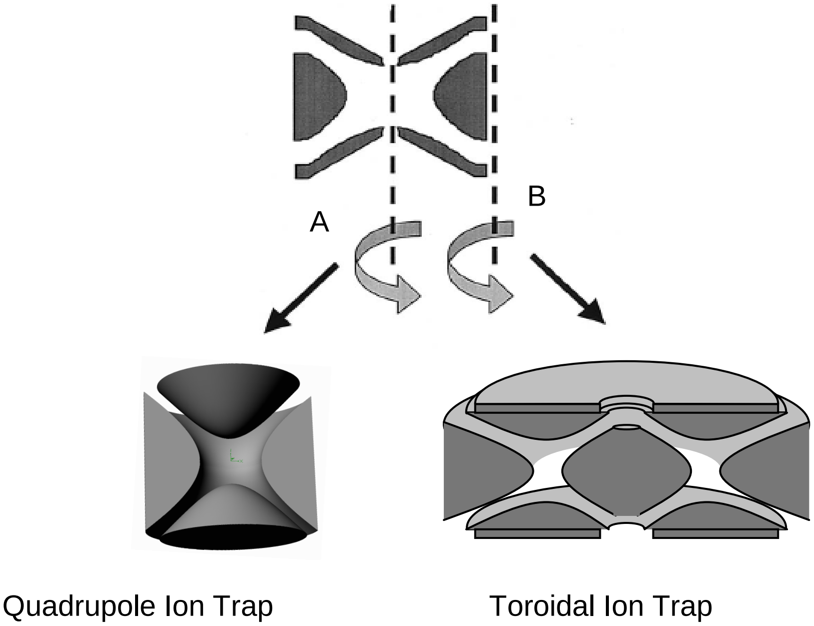

Figure 1.6. Original idea of a toroidal ion trap. Rotation about axis A gives the conventional 3D QIT. Rotation about axis B generates a toroidal ion trap with the same cross-sectional dimensions as the QIT.

Figure 1.7. Photograph of the 1/5-scale toroidal IT with the top end-cap removed. A U.S. quarter is shown to emphasize the small size of the analyzer.

trapping field presented by the curvature of the storage region. Geometric modification was made by stretching the separation of end-cap electrodes, as well as increasing the asymptote angle for the center ring electrode and decreasing the asymptote angle for the outer ring electrode, by which a slight nonlinear (mainly octopole) field is intentionally added to the linear 2D quadrupole trapping field. Adding a small DC component enlarged the difference between the axial and radial secular frequencies. As a result, better performance was obtained in the asymmetric toroidal IT and unit mass resolution was reached.[38] This full size toroidal IT had approximately 300 times larger trapping volume than comparable-sized QITs.

The significant feature of the toroidal IT is the possibility to trade off the increased trapping volume for a smaller analyzer assembly. As shown in Figure 1.7, a 1/5-scale version of the asymmetric toroidal IT was fabricated with four electrodes: two end-cap electrodes, an inner ring electrode, and an outer ring electrode, which formed the trapping chamber with an ion trapping volume comparable to a commercial 3D QIT,[33] but operated at RF voltages of less than 1.5 kV_{p-p} instead of 15 kV_{p-p}. It is currently utilized in a portable gas chromatograph-mass spectrometer (GC-MS) system commercialized by Torion Technologies, Inc.[3] The analytical performance of this miniature toroidal IT has been demonstrated to be comparable to commercial IT mass analyzers with better than unit mass resolution and system detection limit of 250 pg (signal/noise > 3) using solid phase microextraction (SPME). Further reduction in analyzer dimensions could become problematic due to machining tolerances (on the order of 0.0005 inch).

1.9 Halo Ion Trap

The halo IT mass analyzer[93] was developed based on a toroidal trapping geometry by using sets of lithographically deposited gold rings instead of machined electrodes. The mass analyzer was comprised of two parallel ceramic plates. Fifteen 0.1 mm wide concentric gold rings ranging in radius from 5 to 12 mm in 0.5-mm increments were imprinted on the inside surface of each plate and covered with a thin layer of germanium, which prevented charge buildup and smoothed out the potential between the electrode rings. A metal spacer with holes located between the plates around the exterior of the trapping region was used to further define the electric field. The holes were used to admit beams of ionizing electrons and were helpful for pumping of the analyzer. At the center of each plate was a 9-mm hole which allowed for ion ejection. A capacitive voltage divider was used to optimize the trapping field between the two plates by independently specifying the electrical potential function on each ring, which is impossible to do with machined ion traps.

Ions were created *in situ* by electron ionization, and then they were collisionally cooled in a circular band between the two trapping plates. Mass spectra were produced by resonantly ejecting the ions to an electron multiplier. Resonant ejection was carried out by linearly scanning the frequency of the secular voltage. The combination of toroidal geometry and open structure enabled easy access for *in situ* ionization, trapping and analysis. Microfabrication methods made the device easy to miniaturize. When the trap was operated at 1.9 MHz with a driving RF amplitude of 350 $V_{p\text{-}p}$, the mass spectrum of dichloromethane exhibited a resolution of 121 ($m/\Delta m$) for m/z 49, demonstrating both ion trapping and mass analysis capability. SIMION simulations of collisional cooling showed that the ions were collapsed in a toroidal shape, which has a significantly larger trapping volume than that of hyperbolic traps with the same r_0.

In the halo IT, electric fields are made using planar nonequipotential electrodes. The boundaries of electric fields are surfaces on which the potential varies over one or more spatial dimensions. As shown in Figure 1.8, the quadrupole potential field produced by hyperbolic electrodes in a QIT is the same as that in a volume having closed surfaces; the potential at every

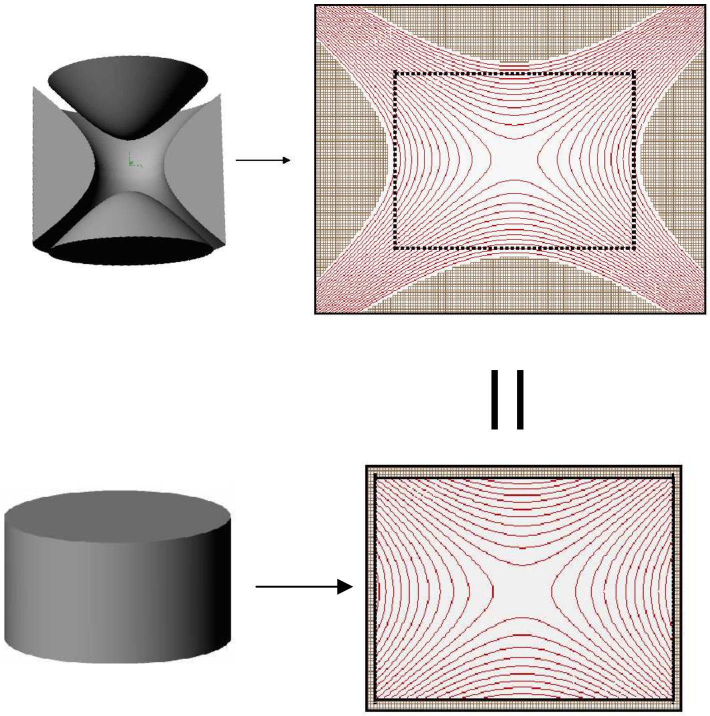

Figure 1.8. Specific potentials on two parallel plates and a cylinder can produce a quadrupolar electric field identical to that of a QIT.

point is chosen to be equal to the corresponding potential in a quadrupole field. Depending on the potentials applied to the closed surfaces, the electric field in such a volume could be perfectly quadrupolar, or be made to match the field in stretched-endcap traps.[94] In contrast to the QIT, a change in plate spacing has little effect on higher order electric fields, but can be modified electronically by adjusting the voltage on each electrode ring.[95]

With this approach, it is possible to produce ITs with various trapping geometries. A quadrupole trapping field was produced between two ceramic plates with the same design, but with a smaller central hole.[96] A coaxial IT[97] was also developed, in which a quadrupole trap was located at the center of the halo IT using the same trapping plates as the planar quadrupole trap. Ions could be trapped in the halo trap, mass-selectively transferred into the quadrupole trap, collisionally cooled, and then mass-selectively ejected to a detector, which resembles tandem MS experiments in space.

1.10 Significance and Contents of This Dissertation

The development of miniature and field portable MS is driven by a variety of *in situ* analysis applications, including environmental analysis and remediation, emissions monitoring and control, chemical and biological weapons detection, and cosmic exploration. The advantages of ITMS, such as ability to operate at relatively high pressure, easy of miniaturization and geometry optimization, and ability to perform tandem MS in a single device, have attracted many groups to develop miniaturized MS by using an IT as the mass analyzer. When the dimensions of the IT become smaller, the shapes of the metal electrodes must be fabricated with high machining precision. Any imperfection in the machining of the electrode surfaces would deteriorate the performance of the miniaturized IT. Moreover, ion trapping capacity becomes smaller with the miniaturization of the IT, resulting in low sensitivity and poor resolution due to ion repulsion problems.

A novel mass analyzer, called the halo IT (briefly described in the previous section), was developed in this work, and the intrinsic advantages of its design addressed the machining and space charge problems. The use of polished ceramic plates and photolithographically deposited electrode rings in the halo IT resulted in a highly planar electrode surface, which avoids problems related to surface roughness[98] and machining issues. The toroidal trapping volume between the two plates gave a large ion storage capacity and avoided space charge problems. The alignment of electrodes is relatively simple, since only two plates comprised the trap. The open structure of the halo IT provided convenient access for ion injection, easily admitted optical or electron beams for ionization, and allowed fast pump down to the same pressure as in the vacuum chamber. Finally, the trapping electric field was optimized by adjusting the potential on each of the electrode rings without change in plate position or modification of the structure of the halo IT.

In this dissertation, Chapter 2 describes a miniaturized toroidal RF IT mass analyzer, which operates with a maximum RF trapping voltage of 1 $kV_{p\text{-}p}$ or less. At the same time, it still retains roughly the same ion trapping capacity as a conventional 3D QIT despite the reduced dimensions. A conventional mass-selective instability scan mode combined with resonance ejection is used to show the expected linear mass scale with RF amplitude. Unit-mass resolution is obtained for the mass spectra of *n*-butylbenzene, xenon, and naphthalene. In Chapter 3, a halo IT is described based on toroidal trapping geometry and microfabrication technology. This device consists of two parallel ceramic plates, the facing surfaces of which are imprinted with sets of concentric ring electrodes. Electric fields in the halo IT are established by applying different RF potentials to each ring. Trapped ions are radially ejected by scanning the resonant frequency. Preliminary mass spectra show resolution ($m/\Delta m$) of 60–75 when the trap is operated at 1.9 kHz and 500 $V_{p\text{-}p}$. Chapter 4 introduces a modification that was made to the halo IT to allow ejection of ions through slits machined in the center ring electrode. This was done to mimic the operation of the toroidal IT with the goal of improving resolution by reducing ejection path dispersion experienced in the halo IT described in Chapter 3. The performance of the modified halo IT with 1% to 7% octopole field (A_4/A_2) components was determined. The best resolution of 280 ($m/\Delta m$) for the 51-Da fragment ion of benzene was obtained with 5% octopole field contribution with resonant frequency scan ejection from high to low frequency, dipole ejection and DC offset. Chapter 5 describes simulations of two designs of the halo IT using SIMION 7.0 and 8.0. The simulation of the halo IT with radial ejection shows bent ion trajectories when ejected ions pass through the central hole in one of the trapping plates, which results in decreased sensitivity. In the halo IT with axial ejection, SIMION and MatLAB are used to determine the quadrupole, octopole and dodecapole contributions to the electric field. Chapter 6 proposes future research directions for performance improvement of the halo IT and the possibility of performing field asymmetric ion mobility spectrometry combined with mass analysis in the halo IT mass analyzer.

1.11 References

1. Gross, J. H. *Mass Spectrometry*; Springer, Inc.: Berlin, Germany; 2004.
2. March, R. E.; Todd, J. F. J. *Quadrupole Ion Trap Mass Spectrometry*, 2nd ed.; John Wiley & Sons, Inc.: Hoboken, NJ; 2005.
3. Contreras, J. A.; Murray, J. A.; Tolley, S. E.; Oliphant, J. L.; Tolley, H. D.; Lammert, S. A.; Lee, E. D.; Later, D. W.; Lee, M. L. *J. Am. Soc. Mass Spectrom.* 2008, *19*, 1425–1434.
4. Blay, P. K. S.; Brombacher, S.; Volmer, D. A. *Rapid Commun. Mass Spectrom.* 2003, *17*, 2153–2159.
5. You, J.; Wang, D. L.; Lydy, M. J. *Talanta* 2010, *81*, 136–141.
6. Dulaurent, S.; Moesch, C.; Marquet, P.; Gaulier, J. M.; Lachatre, G. *Anal. Bioanal. Chem.* 2010, *396*, 2235–2249.
7. Liu, H. C.; Liu, R. H.; Ho, H. O.; Lin, D. L. *Anal. Chem.* 2009, *81*, 9002–9011.
8. Gottardo, R.; Bortolotti, F.; De Paoli, G.; Pascali, J. P.; Miksik, I.; Tagliaro, F. *J. Chromatogr. A* 2007, *1159*, 185–189.
9. Shortt, B. J.; Darrach, M. R.; Holland, P. M.; Chutjian, A. *J. Mass Spectrom.* 2005, *40*, 36–42.
10. Palmer, P. T.; Limero, T. F. *J. Am. Soc. Mass Spectrom.* 2001, *12*, 656–675.
11. Gros, M.; Petrovic, M.; Barcelo, D. *Anal. Chem.* 2009, *81*, 898–912.
12. Madureira, T. V.; Barreiro, J. C.; Rocha, M. J.; Cass, Q. B.; Tiritan, M. E. *J. Chromatogr. A* 2009, *1216*, 7033–7042.
13. Badman, E. R.; Cooks, R. G. *J. Mass Spectrom.* 2000, *35*, 659–671.
14. Gao, L.; Song, Q.; Patterson, G. E.; Cooks, R. G.; Ouyang, Z. *Anal. Chem.* 2006, *78*, 5994–6002.
15. Gao, L.; Sugiarto, A.; Haper, J.; Cooks, R. G.; Ouyang, Z. *Anal. Chem.* 2008, *80*, 7198–7205.
16. Yang, M.; Kim, T. Y.; Hwang, H. C.; Yi, S. K.; Kim, D. H. *J. Am. Soc. Mass Spectrom.* 2008, *19*, 1442–1448.
17. Patterson, G. E.; Guymon, A. J.; Riter, L. S.; Everly, M.; Griep-Raming, J.; Laughlin, B. C.; Ouyang, Z.; Cooks, R. G. *Anal. Chem.* 2002, *74*, 6145–6153.
18. Paul, W.; Steinwedel, H. *Z. Naturforsch.* 1953, *8A*, 448–450.
19. Cooks, R. G.; Kaiser, R. E. *Acc. Chem. Res.* 1990, *23*, 213–219.
20. Nappi, M.; Weil, C.; Cleven, C. D.; Horn, L. A.; Wollnik, H.; Cooks, R. G. *Int. J. Mass Spectrom. Ion Processes*. 1997, *161*, 77–85.

21. Wuerker, R. F.; Shelton, H.; Langmuir, R. V. *J. Appl. Phys.* 1959, *30*, 342–349.
22. Bates, D. R. *Advances in Atomic and Molecular Physics*; Academic Press, Inc.: New York, NY; 1967.
23. Todd, J. F. J.; Waldren, R. E.; Mather, R. E. *Int. J. Mass Spectrom. Ion Phys.* 1980, *34*, 325–349.
24. Guan, S.; Marshall, A. G. *J. Am. Soc. Mass Spectrom.* 1994, *5*, 64–71.
25. Li, G. Z.; Guan, S. Marshall, A. G. *J. Am. Soc. Mass Spectrom.* 1998, *9*, 473–481.
26. Stafford, G. C.; Kelly, P. E.; Syka, J. E. P.; Reynolds, W. E.; Todd, J. F. J. *Int. J. Mass Spectrom. Ion Processes*. 1984, *60*, 85–98.
27. March, R. E.; Todd, J. F. J. *Practical Aspects of Ion Trap Mass Spectrometry*, Vol. 1; CRC Press: Boca Raton, FL; 1995
28. Quarmby, S. T.; Yost, R. A. *Int. J. Mass Spectrom.* 1999, *190/191*, 81–102.
29. Forbes, M. W.; Sharifi, M.; Croley, T. R.; Lausevic, Z.; March, R. E. *J. Mass Spectrom.* 1999, *34*, 1219–1239.
30. Weil, C.; Nappi, M.; Cleven, C. D.; Wollnik, H.; Cooks, R. G. *Rapid Commun. Mass Spectrom.* 1996, *10*, 742–750.
31. Doroshenko, V. M.; Cotter, R. J. *J. Mass Spectrom.* 1997, *32*, 602–615.
32. Kaiser, R. E.; Cooks, R. G.; Stafford G. C.; Syka, J. E. P.; Hemberger, P. H. *Int. J. Mass Spectrom. Ion Processes*. 1991, *106*, 79–115.
33. Lammert, S. A.; Rockwood, A. A.; Wang, M.; Lee, M. L.; Lee, E. D.; Tolley, S. E.; Oliphant, J. R.; Jones, J. L.; Waite, R. W. *J. Am. Soc. Mass Spectrom.* 2006, *17*, 916–922.
34. Badman E. R.; Johnson, R. C.; Plass, W. R.; Cooks, R. G. *Anal. Chem.* 1998, *70*, 4896–4901.
35. Kornienko, O.; Reilly, P. T. A.; Whitten, W. B.; Ramsey, J. M. *Rapid Commun. Mass Spectrom.* 1999, *13*, 50–53.
36. Badman E. R.; Cooks, R. G. *Anal. Chem.* 2000, *72*, 3291–3297.
37. Hager, J. W. *Rapid Commun. Mass Spectrom.* 2002, *16*, 512–526.
38. Lammert, S. A.; Plass, W. R.; Thompson, C. V.; Wise, M. B. *Int. J. Mass Spectrom.* 2001, *212*, 25–40.
39. Wells, J. M.; Badman E. R.; Cooks, R. G. *Anal. Chem.* 1998, *70*, 438–444.
40. Mikami, N.; Sato, S.; Ishigaki, M. *Chem. Phys. Lett.* 1993, *202*, 431–436.
41. Ji, Q.; Davenport, M. R.; Enke, C. G.; Holland, J. F. *J. Am. Soc. Mass Spectrom.* 1996, *7*, 1009–1017.
42. Riter, L. S.; Peng, Y.; Noll, R. J. Patterson, G. E.; Aggerholm, T.; Cooks, R. G. *Anal. Chem*. 2002, *74*, 6154–6162.
43. Richardson, S. D. *Anal. Chem.* 2002, *74*, 2719–2742.
44. Wu, G.; Cooks, R. G.; Ouyang, Z. *Int. J. Mass Spectrom.* 2005, *241*, 119–132.
45. http://www.1stdetect.com/specifications.php
46. Tabert, A. M.; Griep-Raming, J.; Guymon, A. J.; Cooks, R. G. *Anal. Chem.* 2003, *75*, 5656–5664.
47. Blain, M. G.; Riter, L. S.; Cruz, D.; Austin, D. E.; Wu, G.; Plass, W. R.; Cooks, R. G. *Int. J. Mass Spectrom.* 2004, *236*, 91–104.

48 Sikanen, T.; Franssila, S.; Kauppila, T. J.; Kostiainen, R.; Kotiaho, T.; Ketola, R. A. *Mass Spectrom. Rev*. 2010, *29*, 351–391.

49. Badman, E. R.; Cooks, R. G. *Anal. Chem.* 2000, *72*, 5079–5086.
50. Lammert, S. A.; Cooks, R. G. *J. Am. Soc. Mass Spectrom.* 1991, *2*, 487–491.

51. Gibson, J. R.; Taylor, S. *Rapid Commun. Mass Spectrom.* 2001, *15*, 1960–1964.
52. Truong, T. V.; Nackos, A. N.; Williams, J. R.; VanDerwerken, D. N.; Kimball, J. A.; Murray, J. A.; Hawkes, J. E.; Harvey, D. J.; Tolley, H. D.; Robison, R. A.; Bartholomew, C. H.; Lee, M. L. *Anal. Methods* 2010, *2*, 638–644.
53. Truong, T. V.; Nackos, A. N.; Murray, J. A.; Kimball, J. A.; Hawkes, J. E.; Harvey, D. J.; Tolley, H. D.; Robison, R. A.; Bartholomew, C. H.; Lee, M. L. *J. Chromatogr. A* 2009, *1216*, 6852–6857.
54. Douglass, D. J.; Frank, A. J.; Mao, D. *Mass Spectrom. Rev.* 2005, *24*, 1–29.
55. Schwartz, J. C.; Senko, M. W.; Syka, J. E. P. *J. Am. Soc. Mass Spectrom.* 2002, *13*, 659–669.
56. Ruan, Q.; Zhu, M. *Chem. Res. Toxicol.* 2010, *23*, 909–917.
57. Niu, C.; Wu, C.; Sheng, Y.; Zhang, J. *J. Asian Nat. Prod. Res.* 2010, *12*, 300–312.
58. Kim, T.; Schwartz, J. C.; Reilly, J. P. *Anal. Chem.* 2009, *81*, 8809–8817.
59. Dulaurent, S.; Moesch, C.; Marquet, P.; Gauler, J. M.; Lachatre, G. *Anal. Bioanal. Chem.* 2010, *396*, 2235–2249.
60. Bansal, S. S. ; Abbate, V.; Bomford, A.; Halket, J. M.; Macdougall, J. C.; Thein, S. L.; Hider, R. C. *Rapid Commun. Mass Spectrom.* 2010, *24*, 1251–1259.
61. Gerlich, D. *Advances in Chemical Physics LXXXII. Inhomogeneous RF Fields: A Versatile Tool for the Study of Processes with Slow Ions*; John Wiley & Sons, Inc.: New York, NY; 1992.
62. Konenkov, N.; Londry, F.; Ding, C.; Douglas, D. J. *J. Am. Soc. Mass Spectrom.* 2006, *17*, 1063–1073.
63. Rama Rao, V. V. K.; Bhutani, A. *Int. J. Mass Spectrom.* 2000, *202*, 31–36.
64. Brinkmann, U. *Int. J. Mass Spectrom. Ion Phys.* 1972, *9*, 161–166.
65. Hager, J. W. *Rapid Commun. Mass Spectrom.* 1999, *13*, 740–748.
66. Hager, J. W. *Rapid Commun. Mass Spectrom.* 2002, *16*, 512–526.
67. Song, Y.; Wu, G.; Song, Q.; Cooks, R. G.; Ouyang, Z.; Li, H.; Plass, W. R. *J. Am. Soc. Mass Spectrom.* 2006, *17*, 631–639.
68. Ouyang, Z.; Wu, G.; Song, Y.; Li, H.; Plass, W. R.; Cooks, R. G. *Anal. Chem.* 2004, *76*, 4595–4605.
69. Gao, L.; Song, Q.; Patterson, G. E.; Cooks, R. G.; Ouyang, Z. *Anal. Chem.* 2006, *78*, 5994–6002.
70. Clare, A. T.; Gao, L.; Brkić, B.; Chalker, P. R.; Taylor, S. *J. Am. Soc. Mass Spectrom.* 2010, *21*, 317–322.
71. Fico, M.; Yu, M.; Ouyang, Z.; Cooks, R. G.; Chappell, W. J. *Anal. Chem.* 2007, *79*, 8076–8082.
72. Krishnavenia, A.; Vermab, N. K.; Menona, A.G.; Mohantya, A. K. *Int. J. Mass Spectrom.* 2008, *275*, 11–20.
73. Chattopadhyay, M.; Verma, N. K.; Mohanty, A. K. *Int. J. Mass Spectrom.* 2009, *282*, 112–122.
74. Dolnikowski, G. G.; Kristo, M. J.; Enke, C. G.; Watson, J. T. *Int. J. Mass Spectrom. Ion Process.* 1988, *82*, 1–15.
75. Keil, A.; Talaty, N.; Janfelt, C.; Noll, R. J.; Gao, L.; Ouyang, Z.; Cooks, R. G. *Anal. Chem.* 2007, *79*, 7734–7739.
76. Song, Q.; Xu, W.; Smith, S. A. Gao, L.; Chappell, W. J. ; Cooks, R. G.; Ouyang, Z. *J. Mass Spectrom.* 2010, *45*, 26–34.

77. Gao, L.; Cooks, R. G.; Ouyang, Z. *Anal. Chem.* 2008, *80*, 4026–4032.
78. Peng, W.; Goodwin, M. P.; Nie, Z.; Volny, M.; Ouyang, Z.; Cooks, R. G. *Anal. Chem.* 2008, *80*, 6640–6649.
79. Song, Q.; Kothari, S.; Senko, M. A.; Schwartz, J. C.; Amy, J. W.; Stafford, G. C.; Cooks, R. G.; Ouyang, Z. *Anal. Chem.* 2006, *78*, 718–725.
80. Takats, Z.; Wiseman, J. M.; Gologan, B.; Cooks, R. G. *Science* 2004, *306*, 471–473.
81. Harper, J. D,; Charipar, N.; Mulligan, C. C.; Zhang, X.; Cooks, R. G.; Ouyang, Z. *Anal. Chem.* 2008, *80*, 9097–9104.
82. Keil, A.; Hernandez-Soto, H.; Noll, R. J.; Fico, M. Gao, L.; Ouyang, Z.; Cooks, R. G. *Anal. Chem.* 2008, *80*, 734–741.
83. Song, Q.; Smith, S. A.; Gao, L.; Xu, W.; Volny, M.; Ouyang, Z.; Cooks, R. G. *Anal. Chem.* 2009, *81*, 1833–1840.
84. Zhang, C.; Chen, H.; Guymon, A. J.; Wu, G.; Cooks, R. G.; Ouyang, Z. *Int. J. Mass Spectrom.* 2006, *255/256*, 1–10.
85. Chen, H.; Xu, R.; Chen, H.; Cooks, R. G.; Ouyang, Z. *J. Mass Spectrom.* 2005, *40*, 1403–1411.
86. Tabert, A. M.; Goodwin, M. P.; Cooks, R. G. *J. Am. Soc. Mass Spectrom.* 2006, *17*, 56–59.
87. Tabert, A. M.; Goodwin, M. P.; Duncan, J. S.; Fico, C. D.; Cooks, R. G. *Anal. Chem.* 2006, *78*, 4830–4838.
88. Kothari, S.; Song, Q.; Xia, Y.; Fico, M.; Taylor, D.; Amy, J. W.; Stafford, G.; Cooks, R. G. *Anal. Chem.* 2009, *81*, 1570–1579.
89. Church, D. A. *J. Appl. Phys.* 1969, *40*, 3127–3134.
90. Deutch, B. U.; Jacobsen, F. M.; Andersen, L. H.; Hvelplund, P.; Knudsen, H.; Holzscheiter, M. H.; Charlton, M.; Laricchia, G. *Physica Scripta* **1988**, *T22*, 248–255.
91. Waki, I.; Kassner, S.; Birkl, G.; Walther, H. *Phys. Rev. Lett.* **1992**, *68*, 2007–2010.
92. Syka, J. E. P.; Schoen, A. E. *Int. J. Mass Spectrom. Ion Process.* 1990, *96*, 97–109.
93. Austin, D. E.; Wang, M.; Tolley, S. E.; Maas, J. D.; Hawkins, A. R.; Rockwood, A. L.; Tolley, H. D.; Lee, E. D.; Lee, M. L. *Anal. Chem.* 2007, *79*, 2927–2932.
94. Austin, D. E.; Peng, Y.; Hansen, B. J.; Miller, I. W.; Rockwood, A. L.; Hawkins, A. R.; Tolley, S. E. *J. Am. Soc. Mass Spectrom.* 2008, *19*, 1435–1441.
95. Austin, D. E.; Hansen, B. J.; Peng, Y.; Zhang, Z. *Int. J. Mass Spectrom.* 2010, *295*, 153–158.
96. Zhang, Z.; Peng, Y.; Hansen, B. J.; Miller, I. W.; Wang, M.; Lee, M. L.; Hawkins, A. R.; Austin, D. E. *Anal. Chem.* 2009, *81*, 5241–5248.
97. Peng, Y.; Zhang, Z.; Hansen, B. J.; Wang, M.; Lee, M. L.; Hawkins, A. R.; Austin, D. E. Presented at the 58th ASMS conference, Salt Lake City, UT, May 2010.
98. Xu, W.; Chappell, W. J.; Cooks, R. G.; Ouyang, Z. *J. Mass Spectrom.* 2009, *44*, 353–360.

CHAPTER 2. TOROIDAL ION TRAP

2.1 Introduction

Development of portable MS systems[1] addresses a broad range of applications, including chemical and biological agent detection, forensic investigations, environmental on-site monitoring, and illicit drug detection/identification. In order to develop portable mass spectrometers, support utility requirements and cost must be reduced as well as size, weight, and power consumption. In addition, several crucial components of mass spectrometers, such as vacuum system pumps and mass analyzers, must be miniaturized to allow portability.

IT mass analyzers[2] are ideal candidates for the development of portable MS due to their simplicity. They are inherently small, even in commercial devices, and do not require highly precise alignment compared to other types of mass analyzers. Multiple stages of MS can be performed in a single IT mass analyzer. The operating pressure for them is higher than for other forms of MS, which requires less stringent pumping systems. Moreover, since the RF trapping voltage is inversely proportional to the square of the size of the analyzer, a modest decrease in analyzer size results in a large reduction in operating voltage and, hence, lower power requirements. Another benefit is that the reduced IT mass analyzer size leads to shorter ion path length, which may relieve the vacuum requirements even more.

In order to miniaturize IT mass spectrometers, issues of space charge[3] and machining tolerance limits must be addressed. Miniature ITs with conventional hyperbolic shape electrodes have been previously researched.[4] However, the machining tolerance plays a more significant role in trapping field defects as devices become smaller. Simplifying the shapes of the electrodes is one approach to address this machining problem. CIT[5] mass analyzers have been explored since they have planar plate end-caps and a cylindrical ring electrode, which are considerably easier to machine than hyperbolic surfaces, especially in small dimensions. Therefore, much work has been done on miniaturization of ITs with cylindrical geometry.[6,7] When the geometry of the electrodes in CITs deviates significantly from theoretical, corrections to the electrodes and structures of the mass analyzer must be made to restore the trapping field potentials to their theoretical values. Modeling and simulation programs[8] have been used to guide these corrections.

Another issue which offsets the gains from reducing IT size is a reduction in ion storage capacity.[2] This reduced capacity leads to space charge conditions, based on ion-ion repulsion, which results in deteriorated mass resolution and mass peak shifts. Several approaches have been researched to address this constraint in miniaturized IT mass spectrometers. One of the approaches is to array several reduced volume cylindrical ITs[9-11] to recover the reduced ion capacity. Others involve modification of the trapping geometry to increase the ion storage volume while maintaining reduced IT size. Recently, LITs[12] with either radial[13] or axial[14] ejection have been developed by different groups. The length of the 2D quadrupole rod assembly in LITs can be increased to obtain enough trapping volume to avoid space charge problems. These devices are now readily available in commercial versions. For the same reasons that CIT geometries are used to approximate the 3D QITs, an RIT[15-17] has been reported that uses six rectangular plates instead of the three-section-rod assembly in the LIT. All of these linear devices provide an increase in ion storage capacity by employing a traditional 2D quadrupole with ions trapped over a significant length by applying DC potential at either end of the device. In a few cases, these devices have been miniaturized[18] for the purpose of portable analyses. Arrays of linear quadrupoles[19,20] have also been reported for high-throughput *in situ* determination in high pressure processes.

Another mass analyzer whose geometry offers increased ion storage and which could be miniaturized is the toroidal IT.[21] This device has a toroidal trapping region, and can be viewed either as rotating on an edge of a conventional 3D QIT cross section or as curving a linear quadrupole and connecting end to end. In these cases, distortion of the quadrupole trapping field caused by the curvature of the toroidal storage region degrades the performance of the device, and corrections to the shape of the electrodes are required to generate the necessary electric field and improve the performance of the IT. Trapped ions are distributed within a circular storage ring by an RF potential applied to the ring electrodes, which avoids the repulsion problems in smaller trapping volumes. A miniaturized version of the toroidal IT mass analyzer was fabricated, and preliminary data were obtained.

In the miniature toroidal mass analyzer, despite the reduced dimensions, approximately as many ions can be trapped in the toroidal region as a full size, commercial IT mass spectrometer with a 1 cm radial dimension. Moreover, because of the reduced geometric dimensions of the device, it is operated at considerably lower RF voltage because of the inverse relationship between the two variables. Therefore, this device operates with an RF voltage less than 1 $kV_{p\text{-}p}$ instead of operating at ca. 15 $kV_{p\text{-}p}$ in the case of commercial QITs.

The miniature toroidal IT retains all of the advantages discussed earlier, i.e., size, simplicity, pressure tolerance, and tandem MS capability. Compared to the approach of arraying several miniature ITs to address space charge problems, the toroidal IT traps all ions in a single trapping field, which avoids concerns from a machining standpoint in matching the individual ITs in an array or in interfacing ion sources or detectors to ensure equal rates of ions entering in or ejecting from each cell of the array. Multiple RF power supplies can be used to correct for the small machining differences that might be present in an array of ITs, however, multiple RF circuits are complicated and undesirable from the perspective of developing field portable instruments. Even though multiple IT cells of different size have been used to simultaneously and selectively trap ions of different *m*/*z* to avoid RF drivers,[22] this approach is limited by the number of cells that can be arrayed in order to miniaturize the mass spectrometer system. In the miniature toroidal IT, the trapping field is homogenous throughout the entire trapping volume. Because the performance of the mass analyzer strongly depends on machining quality, it remains to be determined if this advantage of homogenous trapping field could be fully realized as the toroidal mass analyzer is miniaturized further.

2.2 Experimental Section

The toroidal IT mass analyzer consists of three sections: the EI ion source, the trapping region, and the detector assembly. The trapping region is formed by four electrodes, a filament end-cap electrode, a detector end-cap electrode, an inner ring electrode and an outer ring electrode, as can be seen in the photograph in Figure 2.1. The names of the four electrodes arise historically from the 3D QIT origin and indicate their location in the assembly (i.e., the filament end-cap is the electrode closest to the ionizer; the detector end-cap is closest to the detector, etc.). The “axial” and “radial” dimension terms for the traditional 3D IT would still be valid if only the cross-sectional trapping geometry is considered in the toroidal IT. If it is treated as a linear quadrupole model, the *x*-dimension is defined here as the non-ejection dimension (towards the inner/outer rings), the *y*-dimension is defined as the ejection dimension (towards the end-caps), and the *z*-dimension is tangential to the toroidal trapping field. The electrodes were precisely machined with machining tolerance specified to 0.0005 inch (0.013 mm) from 316 stainless steel. The dimensions of the device were scaled to 1/5 of the size of the original version with a radius (r_0) of 2.0 mm, and it retained the same shape corrections of the trapping field.[21] Spacers

Figure 2.1. Photograph of the miniature toroidal IT mass analyzer showing the filament endcap (left) removed to expose the ion storage region (right). A U.S. quarter-dollar coin is included in order to emphasize the small size.

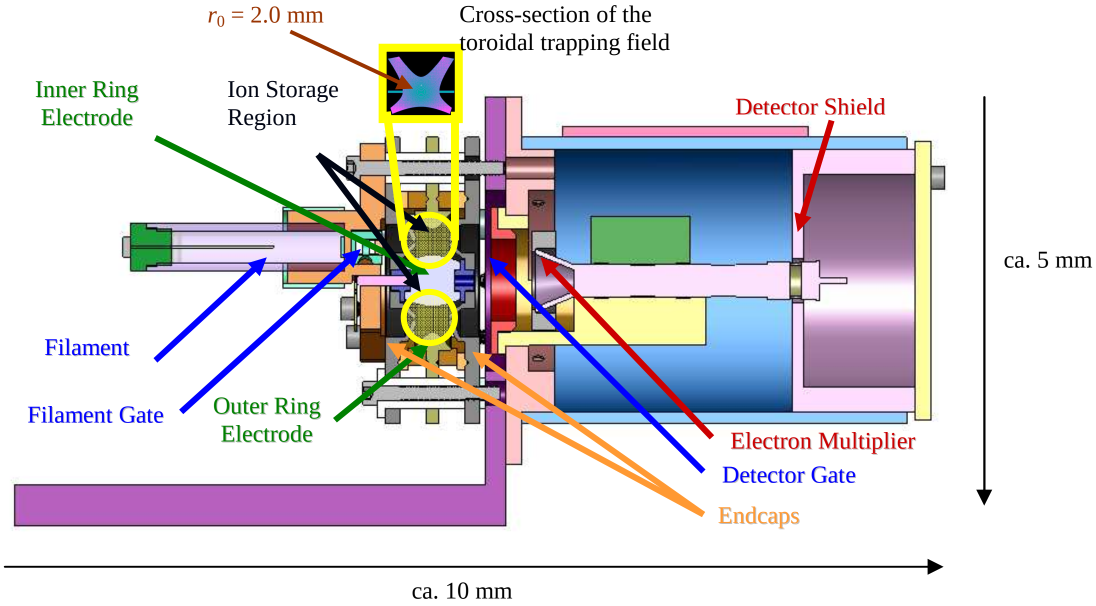

Figure 2.2. Cross-section schematic of the miniature toroidal IT analyzer showing the major components. The inset shows a cross-section of the miniature toroidal IT with shape corrections to the electrodes.

between electrodes were machined from alumina or Vespel and provided room to allow gas conductance in and out of the trapping region. Entrance and exit slits with a width of 0.28 mm and three 93° arcs were machined into each of the two end-caps using a plunge electro-discharge machining technique to allow the ionizing electrons to enter into the trapping region and ejected ions to exit to the detector.

A cross-section schematic of this toroidal IT mass analyzer assembly is shown in Figure 2.2. A miniature electron gun was designed to focus ion source electrons into the trapping area by emitting high-energy electrons from a heated filament through a three-element Einzel lens and then through a slit fabricated in the end-cap electrode. The middle part (L2) of the Einzel lens also acted as a gate to turn the ionization on and off. A custom circuit was designed to switch the L2 voltage between –50 V for ionization off and +125 V for ionization on. A constant-current power supply (Lambda, Model LPT-7202-FM, Plainview, NY) provided 70 eV electron energy with a 1.5-A filament current.

A custom continuous dynode electron multiplier detector (Detector Technologies, Palmer, MA) was fabricated to provide >10^5 gain at roughly 1 kV with pressures up to 10^{-2} mbar. A custom circuit providing a gating voltage on a lens mesh between the detector end-cap and the electron multiplier switched between a maximum of +50 V for detector gate closed and –50 V for detector gate open to protect the detector from large ion currents during ionization. A high voltage power supply (Bertan/Spellman, Model 230, Hauppauge, NY) provided the detector voltage at –1.7 kV.

The trapping field was established using a custom self-resonant tank RF driver with a 1.9-MHz-frequency signal applied to both the inner and outer ring electrodes. The amplitude of the RF voltage was 100–200 $V_{p\text{-}p}$ during the ionization and ion cooling periods of the scan.

During mass analysis, the RF amplitude was then scanned to 700–1200 $V_{p\text{-}p}$ in a time period of 200 ms, depending on the mass range desired. At the end of each scan, the RF amplitude was turned off for 5 ms to allow all remaining ions to leave the trap before the next scan. An arbitrary waveform generator (Agilent, Model 33250A, Palo Alto, CA) was used to provide the resonant ejection frequency during the RF amplitude scan to produce mass spectra. This signal was applied to both end-cap electrodes through a custom Balun amplifier, which converted the signal into two signals with 180º phase difference for dipole ejection. The system also contained a DC offset circuit to allow variations in the Mathieu *a* parameter.[2]

The entire mass spectrometer analyzer was only 5 cm in diameter and 10 cm long, including the ionizer and detector, as shown in Figure 2.2. The device was enclosed in a custom vacuum chamber pumped by a 230 L/s turbo pump (BOC Edwards, Model EXT255, Crawley, West Sussex, UK) backed by a 20 m^3/h mechanical pump (BOC Edwards, Model E2M18, Crawley, West Sussex, UK). Pressures were read using a full range cold cathode vacuum gauge and controller (Pfeiffer, Model PKR 251/261, Asslar, Germany). All pressure readings reported here are uncorrected values.

All samples used here were reagent grade and introduced directly into the vacuum chamber through either precision needle valves (Nupro/Swagelok, Solon, OH) or variable leak valves (Granville-Phillips, Boulder, CO). As is typical for most IT mass spectrometers, helium buffer gas was used to kinetically cool the ions before mass analysis with a nominal pressure of approximately 3×10^{-4} mbar admitted through the same precision needle valves described above.

Mass spectral data were recorded using a four-part scan function. A period of ionization for 10–100 ms was followed by a period of ion cooling for about 10–30 ms. The third segment of the scan function was RF amplitude ramping with resonant frequency ejection to perform mass analysis in 200 ms before the RF was turned off for approximately 5 ms to eliminate all ions from the trap in preparation for the next four-part scan. The timing of the scan function segments was controlled by a PIC-16C770 (Microchip Technology, Chandler, AZ) digital microcontroller, which was programmable through an I^2C interface, Aardvark I^2C Control Center (Total Phase, Sunnyvale, CA), to set the timing values in the PIC. The digital I/O outputs from the PIC were then used to control the initiation of the signal acquisition integrator, the start of the RF ramp, the arbitrary waveform generator, the gating of the ionizer and detector, and the RF signal on/off status.

A multifunction data acquisition (DAQ) board (National Instruments Model 6115, Austin, TX) coupled with a multiport connector panel (National Instruments, Model BNC 2110, Austin, TX) was used to provide a variable modulation voltage to the RF generator to control the RF ramp. Signals from the detector were integrated using a custom preamplifier with a transconductance of 128 MΩ and sent to the DAQ board by the multiport connector panel. Then the signals were digitized by one of the analog-to-digital channels of the multifunction DAQ. A synchronization pulse from the DAQ started both the signal integrator and the RF ramp simultaneously. The signal integrator was operated at 30 kHz, which means that it provided a digitized signal every 33.3 μs. A typical RF scan covered ~ 300 Da in 200 ms, allowing ~ 0.67 ms/Da. Therefore, at 30 kHz integration, there were ~ 20 scan points acquired across each nominal mass unit. The number of signal integrations in the output was linear with time and, therefore, the signal integrating count (or integrator sample number) was used to calibrate the mass scale for the acquired data. Operating input and data output were controlled and displayed by an instrument control screen program using Labview 7.1 (National Instruments, Austin, TX).

Since the current Labview instrument control and acquisition program was rudimentary, all spectra shown were screen captures of the spectra as displayed in the user interface.

2.3 Results and Discussion

Since the toroidal IT is a 2D quadrupole device, and if the field corrections employed to compensate the distortions introduced by the curvature of its geometry are adequate, the cross-sectional trapping field should look like a linear quadrupole. In the toroidal IT, unlike in traditional 3D ITs, the Mathieu *q*-values (and therefore β-values) for the x and y dimensions should be the same, which indicates that the trapped ions have similar, if not the same, secular frequencies in the x and y dimensions. A significant contribution of higher order fields introduced intentionally or unintentionally couples the ion motions in the x and y dimensions.[2] Therefore, energy associated with the ion's motion in the y dimension during resonance ejection can subsequently be coupled into the x dimension motion, causing spreading of the ion cloud during mass analysis, which results in poor resolution. It was found that a small DC voltage applied to either the end-caps or the ring electrodes alters the Mathieu a value in the stability equations and improves the mass resolution. In a 2D quadrupole device, β_x equal to β_y only occurs for an a value of zero, and any non-zero a value will separate the β_x and β_y parameters and, correspondingly, differentiate the secular frequencies in the x and y dimensions. Typically, a negative DC voltage (ca., –1 V) was applied to both end-cap electrodes through the Balun box during operation to realize this.

Mass spectral data were obtained for seven different samples (benzene, toluene, chlorobenzene, *n*-butylbenzene, naphthalene, xenon, and methylnaphthalene) and used to create the mass calibration graph shown in Figure 2.3. Since the RF amplitude was scanned linearly and the sample integrator was initiated at the same time as the beginning of the RF ramp, there is a

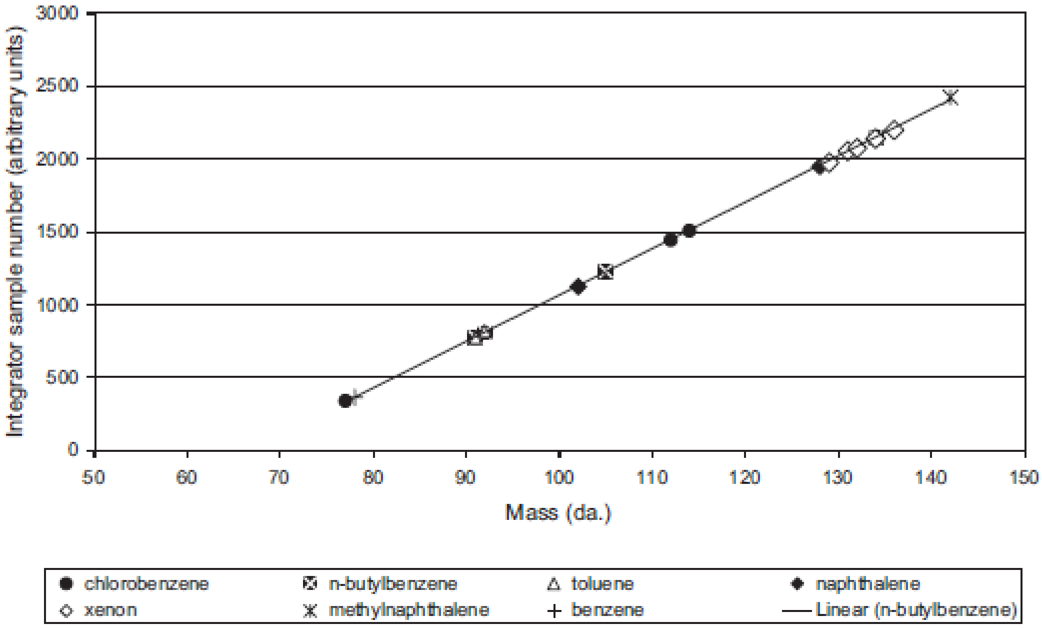

Figure 2.3. Mass calibration using seven compounds. Masses used for calibration are in parenthesis: chlorobenzene (77, 112, 114 Da); benzene (78 Da); toluene (91, 92 Da); n-butylbenzene (91, 92, 105, 134 Da); naphthalene (102, 128 Da); xenon (129, 131, 132, 134, 136 Da); methylnaphthalene (142 Da).

direct linear relationship between the sample integrator number and RF amplitude. The calibration table in Figure 2.3 shows the expected linear relationship between mass and RF amplitude.

The mass spectrum of *n*-butylbenzene (sample pressure of 1 × 10^{-5} mbar, uncorrected) is shown in Figure 2.4A. The inset shows the peak doublet at *m*/*z* 91/92, which is clearly resolved. Measurement of the mass resolution for the peak at *m*/*z* 91 gave 0.4 Da full-width at half-maximum (FWHM). The spectrum was obtained by scanning the RF amplitude from 190–770 $V_{p\text{-}p}$ in 200 ms. The RF frequency was 1.9 MHz, and a resonant ejection frequency of 900 kHz (corresponding to an approximate ejection β value of 0.95) was used to eject ions during the RF amplitude scan. A DC offset of –890 mV was applied to the end-caps to discriminate the secular frequencies in the x and y dimensions (i.e., Mathieu $a \neq 0$). The scan rate of 200 ms/scan was

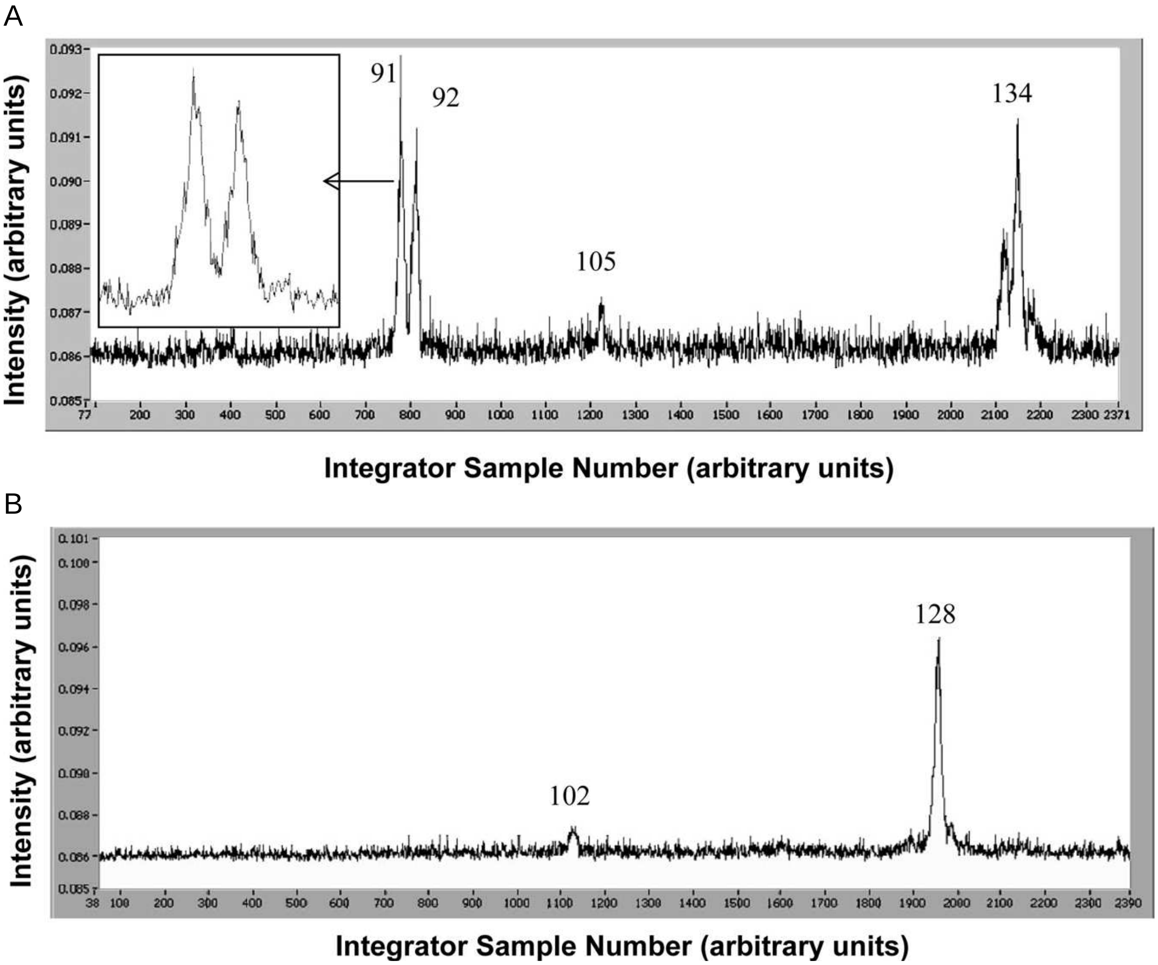

Figure 2.4. (A) Spectrum acquired for n-butylbenzene at a sample pressure of 1 × 10^{-5} mbar. Peaks were assigned with nominal m/z values derived from a calibration table. (B) Spectrum acquired for naphthalene at low sample pressure (2 × 10^{-6} mbar) and short ionization time (20 ms). Peaks were assigned with nominal m/z values derived from a calibration table.

required in this experiment to maintain unit mass resolution, but was slower than desired for effective capillary GC-MS performance. Experiments on mass analyzer design, operating conditions, and machining or assembly procedures are still being investigated to improve the mass resolution at faster scan rates.

A mass spectrum for naphthalene is shown in Figure 2.4B to evaluate the general system sensitivity. Despite the early stage of development, high signal-to-noise spectra were obtained for samples with pressures as low as 2 × 10^{-6} mbar and ionization times as low as 20 ms. The

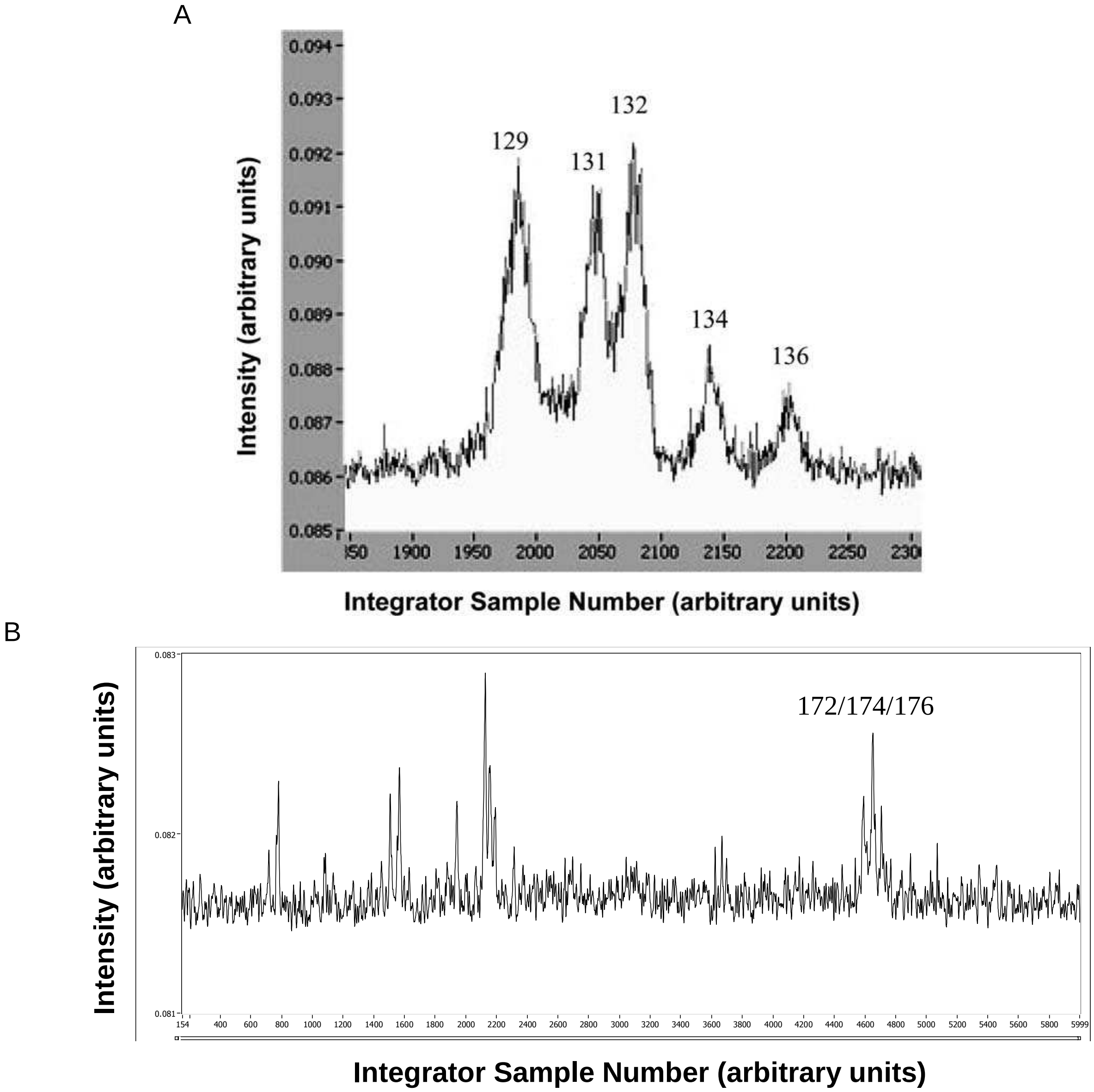

Figure 2.5. Mass spectra showing resolution of isotope peaks. (A) Spectrum for xenon showing five isotope peaks. Sample pressure was 2.3 × 10^{-5} mbar. (B) Spectrum for dibromomethane showing three molecular isotope peaks. Sample pressure was 9.1 × 10^{-5} mbar. All peaks were assigned with nominal m/z values derived from a calibration table.

minor peak in the naphthalene spectrum at *m/z* 102 Da is still clearly observable. This performance is comparable to a conventional 3D IT system. Mass spectra of xenon and dibromomethane are shown in Figure 2.5 to show the resolution of isotope peaks. A mass spectrum of the molecular ion region for xenon is shown in Figure 2.5A. The expected isotope pattern is observed and each of the isotopes is clearly resolved. Figure 2.5B shows a spectrum of dibromomethane with the molecular isotopes resolved at *m*/*z* 172, 174 and 176.

Machining tolerance is still crucial to further miniaturize the toroidal IT mass analyzer to a large degree. The precision of the electrode dimensions during machining were specified to 0.0005 in. (0.013 mm) tolerances, which are at or near the limits of machining capabilities today. The importance of tolerances in this device was realized when it was polished using aluminum oxide powder. As a result, ion signals were completely lost after the analyzer was reassembled and tested due to alteration of ~0.005 in. (0.13 mm) in the outer ring electrode shape during improper cleaning. After a new outer ring electrode was replaced, all normal performance in the system was restored.

Improvements in mass resolution are continually being made by optimizing the operating parameters, including the RF drive frequency, resonant ejection frequency, and DC offset voltage applied to the end-caps. In addition, further improvements in the RF power supply to give higher drive frequency and increased amplitude will provide improved mass resolution and faster scan speed. Cables and shielding were not yet optimum in the prototype system, resulting in relatively high system electronic noise. Simulation programs such as SIMION and COMSOL should be employed to optimize the quality of the toroidal trapping field, especially the non-ejection dimension, since previous efforts in geometry optimization in the full-size version[21] were focused only on the ejection dimension. Attempts must focus on lowering the higher order component in the non-ejection dimension, which spreads the trapped ions in this dimension, leading to poor resolution.

2.4 Conclusions

Miniaturization of the toroidal IT mass analyzer with unit mass resolution and high sensitivity was accomplished. Further development is challenging because of machining tolerances for the complex shapes of the trapping electrodes. The low RF power used and small analyzer components in this miniaturized device are necessary for development of portable mass spectrometer systems operated by batteries.

2.5 References

1. Badman, E. R.; Cooks, R. G. *J. Mass Spectrom.* 2000, *35*, 659–671.
2. March, R. E.; Todd, J. F. J. *Practical Aspects of Ion Trap Mass Spectrometry*, Vol. 1; CRC Press: Boca Raton, FL; 1995
3. Guan, S.; Marshall, A. G. *J. Am. Soc. Mass Spectrom.* **1994,** *5*, 64–71.
4. Kaiser, R. E.; Cooks, R. G.; Stafford G. C.; Syka, J. E. P.; Hemberger, P. H. *Int. J. Mass Spectrom. Ion Processes*. 1991, *106*, 79–115.
5. Wells, J. M.; Badman E. R.; Cooks, R. G. *Anal. Chem.* 1998, *70*, 438–444.
6. Kornienko, O.; Reilly, P. T. A.; Whitten, W. B.; Ramsey, J. M. *Rapid Commun. Mass Spectrom.* 1999, *13*, 50–53.
7. Patterson, G. E.; Guymon, A. J.; Riter, L. S.; Everly, M.; Griep-Raming, J.; Laughlin, B. C.; Ouyang, Z.; Cooks, R. G. *Anal. Chem.* 2002, *74*, 6145–6153.
8. Wu, G.; Cooks, R. G.; Ouyang, Z. *Int. J. Mass Spectrom.* 2005, *241*, 119–132.
9. Badman, E. R.; Cooks, R. G. *Anal. Chem.* 2000, *72*, 5079–5086.
10. Badman E. R.; Cooks, R. G. *Anal. Chem.* 2000, *72*, 3291–3297.
11. Tabert, A. M.; Griep-Raming, J.; Guymon, A. J.; Cooks, R. G. *Anal. Chem.* 2003, *75*, 5656–5664.
12. Douglass, D. J.; Frank, A. J.; Mao, D. *Mass Spectrom. Rev.* 2005, *24*, 1–29.
13. Schwartz, J. C.; Senko, M. W.; Syka, J. E. P. *J. Am. Soc. Mass Spectrom.* 2002, *13*, 659–669.
14. Hager, J. W. *Rapid Commun. Mass Spectrom.* 2002, *16*, 512–526.
15. Song, Y.; Wu, G.; Song, Q.; Cooks, R. G.; Ouyang, Z.; Li, H.; Plass, W. R. *J. Am. Soc. Mass Spectrom.* 2006, *17*, 631–639.
16. Ouyang, Z.; Wu, G.; Song, Y.; Li, H.; Plass, W. R.; Cooks, R. G. *Anal. Chem.* 2004, *76*, 4595–4605.
17. Gao, L.; Song, Q.; Patterson, G. E.; Cooks, R. G.; Ouyang, Z. *Anal. Chem.* 2006, *78*, 5994–6002.
18. Boumsellek, S.; Ferran, R. J. *J. Am. Soc. Mass Spectrom.* **2001,** *12*, 633–640.
19. Ferran, R. J.; Boumsellek, S. *J. Vac. Sci. Technol. A* **1996,** *14*, 1258–1265
20. Orient, O. J.; Chutjian, A.; Garkanian, V. *Rev. Sci. Inst.* **1997,** *68*, 1393–1397.
21. Lammert, S. A.; Plass, W. R.; Thompson, C. V.; Wise, M. B. *Int. J. Mass Spectrom.* 2001, *212*, 25–40.
22. Badman, E. R.; Cooks, R. G. *Anal. Chem.* 2000, *72*, 5079–5086.

CHAPTER 3. HALO ION TRAP WITH RADIAL EJECTION

3.1 Introduction

ITMS is playing a significantly increasing role in modern chemical analysis. Its inherent high sensitivity and specificity facilitate many applications,[1] including threat detection, investigation of chemical and biochemical systems, illicit drug identification, planetary exploration, and environmental monitoring. The advantages of compact size and the ability to trap and accumulate ions enhance the attractiveness of the IT mass analyzer. Furthermore, the ability to perform tandem MS in a single trapping device and the requirement to operate at higher pressures than other mass analyzers represent major advantages, especially for miniaturization of instrumentation and field portability.[2]

The original quadrupole IT, introduced by Paul[3] in 1953 and still used today, consists of a hyperbolic ring electrode between two hyperboloidal end cap electrodes. A megahertz RF voltage supplied at the ring electrode produces the time-dependent, quadrupolar-shaped electric field, which is essential for the storage of ions. Several methods exist for mass analysis, such as mass-selective instability scan, resonance ejection, and mass-selective storage. A variety of IT geometries and variations have evolved since the original Paul trap, including cylindrical,[4] linear,[5] rectilinear,[6] toroidal,[7] modified angle,[8] and higher-order multipole (e.g., 22-pole) traps.[9] Each trap geometry has a unique set of advantages in areas such as increased ion trapping capacity[5,10] or ease of fabrication and miniaturization.[11-13] For instance, the CIT has a simplified geometry, consisting of a cylindrical electrode and two end caps.[5,13-16] This geometry simplifies machining in full-size traps and greatly facilitates miniaturization.[17,18] Although the electric fields deviate from “ideal quadrupolar” more than some other traps, mass analysis is satisfactory for most applications.

LITs[5,19] have hyperbolic (or, in simpler versions, cylindrical) rod profiles, similar to QMFs, but with four rods in each of three axial sections. Ions are trapped within the center section through a combination of a radial quadrupolar field and axial potential created by raising the potentials on the two end sections. The trapping volume is larger than in Paul traps because ions are trapped over a significant length of the central axial section. This larger trapping region increases both the efficiency of cooling of injected ions and the number of ions that can be trapped.[10] The RIT[6,20] combines the advantages of the LIT and the simple geometry of the CIT. This device consists of two pairs of rectangular electrodes supplied with RF signals in the *x* and *y* dimensions and a pair of *z* electrodes supplied with only a DC voltage. Ions are trapped in the quadrupolar RF field between the *x*-*y* planes and stopped by the DC potential well along the *z* axis.

A toroidal IT, operated using mass-selective instability, was reported by Lammert et al.[7,21] This mass analyzer is composed of four electrodes: a filament end cap, a detector end cap, an inner ring, and an outer ring, which form the trapping chamber. This device can be viewed either as a Paul IT cross section that is rotated along a line external to the trap or as a QMF curved and connected end to end. Because of distortions to the quadrupole trapping field presented by curvature of the storage region, which deteriorate the performance of the device, a slight nonlinear (mainly octopole) field is intentionally added to the linear 2D quadrupole trapping field, and asymmetrically shaped electrodes are fabricated to improve the ion ejection characteristics. Ions are trapped and distributed in a large-volume circular storage ring. This miniature device has approximately the same ion storage volume as a commercial IT mass analyzer with a 1-cm radial dimension, but operates at RF voltages of less than 1 kV_{p-p} instead of 16 kV_{p-p}. Unit mass resolution has been achieved using the miniature toroidal RF IT mass analyzer.

Miniaturization of each of the above geometries has been pursued, but good performance has been hindered by several factors.[13,20,21] For instance, the trapping volume and, hence, storage capacity of a hyperbolic or cylindrical trap generally scales as the cube of the trap radius. The smaller the trap, the fewer the ions that can be contained, which can result in poor sensitivity unless a trap array is used.[22-25] Traps with larger inherent storage volumes (e.g., linear and toroidal) provide improvement in this area. Furthermore, sample ionization and introduction are more difficult with miniature traps.[17] For *in situ* EI, the electron path through the trap is short, so the ionization probability is reduced. For externally created ions, injection into the trap becomes inefficient as few cooling collisions can take place in the short distance within the trap. Both *in situ* and external ionization become difficult as the entrance to the trap becomes small compared with the size of the ion or electron beam. IT miniaturization strategies must take these factors into account.

In this chapter, we describe a novel IT mass analyzer, called the halo IT, which is based on a circular or toroidal trapping geometry in which the fields are produced, not by shaped electrodes, but rather by numerous electrode rings imprinted on two planar substrates. The term “halo”, meaning a disk or ring, describes both the geometry of the trapped ions and the geometry of the electrodes. The halo trap possesses the same large trapping volume as the toroidal and linear ITs. At the same time, the open structure provides improved access for ionization. Finally, constructing the trap using microlithography methods simplifies fabrication, assembly and miniaturization.

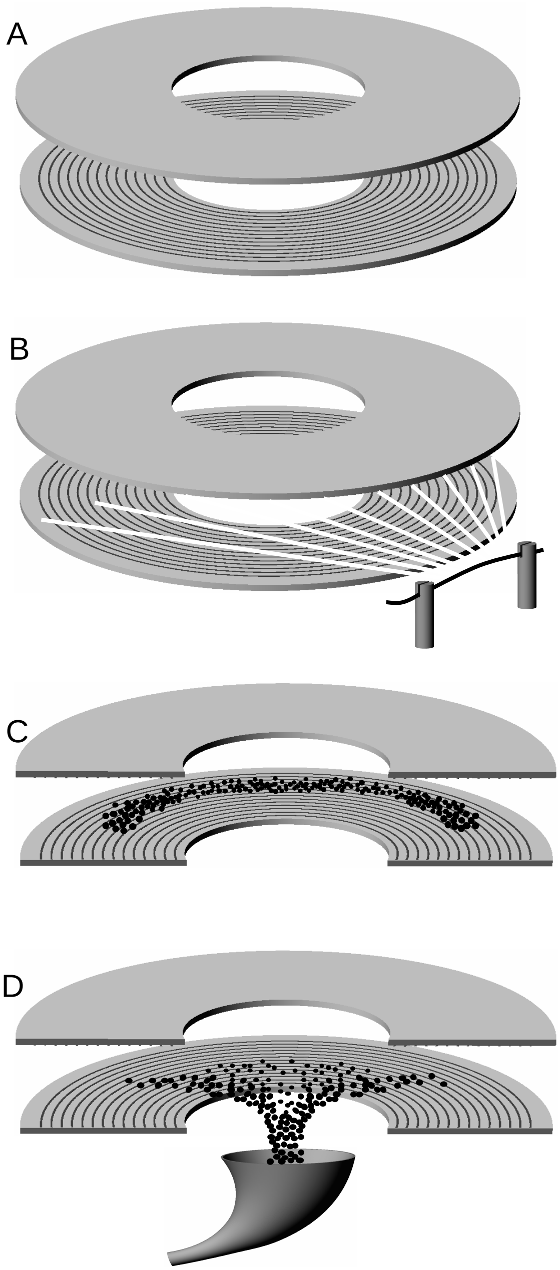

Figure 3.1. (A) Halo IT mass analyzer consisting of two parallel ceramic plates; the inside surfaces of each are patterned with metal ring electrodes and overlaid with germanium; (B) in situ electron ionization; (C) cut-away showing ion trapping between plates; (D) ion ejection into an electron multiplier.

3.2 Experimental Section

3.2.1 Design of the halo ion trap

The design of the halo IT is illustrated in Figure 3.1. It consists of two parallel ceramic plates with facing surfaces imprinted with concentric electrode rings. Appropriate RF and DC potentials are applied to each electrode ring to allow trapping and mass analysis. The field lines are generally similar to those of the toroidal IT. A unique feature of this trap is that it has a very open structure; i.e., gas molecules and ionizing electrons can freely enter the trap through the spacing between the plates. Ions are formed, trapped, and collisionally cooled within the toroidal field. During mass analysis, ions are ejected into the center of the structure and onto an electron multiplier detector.

3.2.2 Fabrication of the halo ion trap electrodes

The procedure for fabrication of the trapping plates is illustrated in Figure 3.2. Construction began with 0.635-mm-thick, 99.6% purity alumina substrates (Micro Substrate, Tempe, AZ). A series of holes were laser cut (Questech Services, Garland, TX) through the alumina. The largest center hole was cut to a diameter of 9.14 mm, and fifteen 127-μm holes were cut in a spiral pattern, each with an increasing radius from the middle of the center hole of 0.5 mm. The center hole served as an exit for electrons ejected from the trap, while the 15 spiraling holes were used to electrically connect ring electrodes to electronic elements on the opposite side of the substrate. Additional holes were cut to fit positioning rods used to align two substrates together to form the trap. After laser cutting, the 127-μm holes were filled with a gold-tungsten alloy and both sides of the alumina substrates were polished to a surface roughness of better than 1 μm. Small trap substrates as shown in Figure 3.3 were then laser cut from the

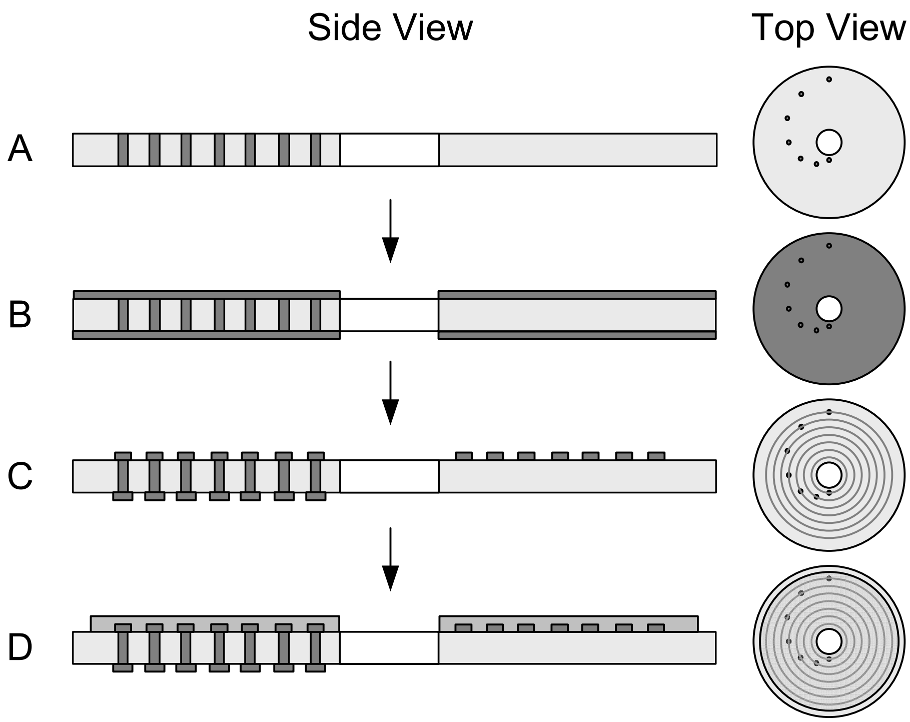

Figure 3.2. Fabrication steps for each open storage ring electrode plate. (A) Holes laser cut in smooth ceramic discs, filled with gold; (B) chromium and gold layers evaporated on both sides of discs; (C) chromium and gold layers patterned and etched on the top and back sides of the discs; (D) top-side coated with germanium.

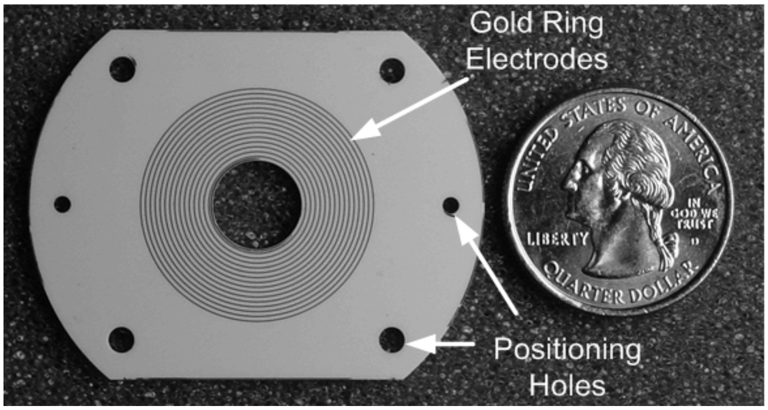

Figure 3.3. Top-view photograph of a trapping plate fabricated from an alumina substrate. The picture was taken before deposition of germanium over the gold ring electrodes.

polished sheets. Metal electrodes were formed on the substrate surfaces in the Brigham Young University Integrated Microfabrication Laboratory.

The substrates were spin-coated with photoresist, which was then photolithographically patterned using chrome masks. The mask design for each side of the substrate contained 15 rings, 100 µm wide, spaced 500 µm from each other as shown in Figure 3.3. Each ring was designed to intersect one of the gold-tungsten filled laser-cut through-holes in the substrate. After development and removal of the photoresist, a 500-nm germanium layer was vapor deposited on the top side of the substrates. The germanium layer coated the gold ring electrodes to serve as a charge dissipation layer for the trap while in operation. The resistivity of the germanium layer also produced a well-defined transition potential between adjacent rings, reducing edge effects on ions located close to the rings. Out of the total number of plates made, 75% worked well.

A capacitor network was used to establish the voltages on each of the ring electrodes under RF excitation. Spring-loaded pins were also soldered to the PCB board in order to make electrical contact with the substrates. The alignment rods that were used to hold the alumina substrates in position relative to one another were also used to hold the capacitor populated PCB boards in position relative to each substrate.

3.2.3 Electron ionization source

In initial tests, sample gases were ionized inside the trapping volume using electron ionization. Electrons emitted from a hot tungsten filament were accelerated and focused into a planar beam, which passed between the plates. Because of the open geometry of the trap, virtually all of the trapping volume was flooded with electrons simultaneously (see Figure 3.1). The gating of the electrons from the e-gun was done by changing the bias voltage on the filament from –70 to +50 V.

3.2.4 Waveform generation

The halo IT requires several different waveforms to function properly. The trapping RF waveform was generated using custom-built electronics that generate a 1.9-MHz sinusoidal wave with amplitude up to 650 $V_{p\text{-}p}$. The ejection AC signal was a triggered frequency sweep with increasing amplitude, starting at 50 kHz and ending at 600 kHz. The frequency sweep was provided by an arbitrary waveform generator (33250A, Agilent Technologies, Santa Clara, CA). The resonance ejection signal was applied only to the innermost and outermost electrode rings on each plate and was superimposed on the driving RF signal already being applied to those rings.

3.2.5 Operation of the halo ion trap

The halo IT was enclosed in a custom vacuum chamber pumped by a turbomolecular pump (Pfeiffer, model TMH 520-020, Asslar, Germany). All samples were HPLC grade or were >99% pure. The headspace vapors of the samples were introduced directly into the vacuum chamber via precision needle leak valves (Nupro/Swagelok, Solon, OH). Sample pressures were normally 10^{-5} mbar, and helium buffer gas was admitted into the vacuum chamber to kinetically cool the ions via the same precision needle leak valves to a nominal pressure of 10^{-4}–10^{-3} mbar. All pressures were measured by a full-range cold cathode vacuum gauge and controller (Pfeiffer, model PKR 251/261, Asslar, Germany). All readings reported here are uncorrected values.

As shown in Figure 3.1, ions are trapped between the two electrode plates and ejected through the center hole to the detector. The operation of the halo IT is illustrated by comparing the diagram in Figure 3.1 with the timing scheme in Figure 3.4. At the beginning of the cycle, the RF voltage is turned off to clear previously trapped ions out of the trap. The RF is then turned back on along with the e-gun, allowing sample to be ionized in the trapping volume. The e-gun is then turned off, allowing the ionized and trapped sample to collisionally cool. The ejection AC is

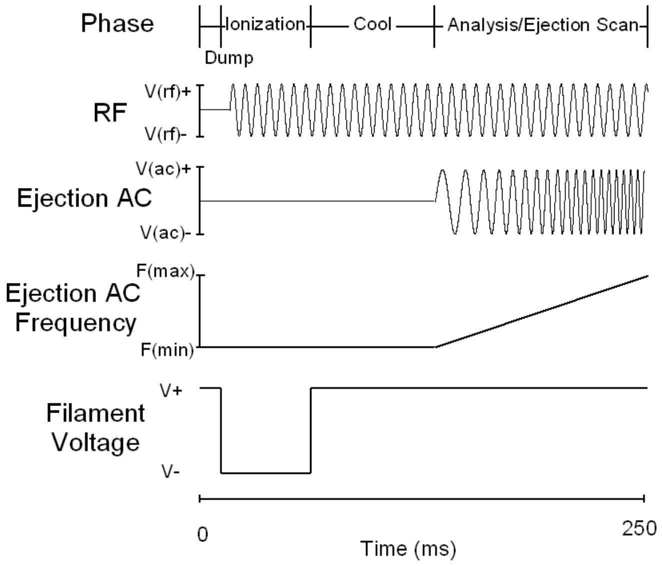

Figure 3.4. Timing diagram for the Halo IT. The four stages are dump, ionize, cool, and analysis/ejection scan. In the dump stage, the RF is turned off to eject trapped ions that were not ejected during the previous analysis/ejection scan. During the ionization stage, both the trapping RF and the filament bias voltage (-70 V) were turned on (e-gun on). During the cool stage, the filament bias voltage was turned back to +50 V (e-gun off), while maintaining the trapping RF in order to cool the ions. In the final stage (analysis/ejection scan), the trapping RF stayed on, while the ejection AC swept through the ejection frequency.

then turned on, and a frequency sweep is initiated. As this ejection frequency reaches the secular frequency of an ion, that ion is resonantly ejected from the trap. Because ejection frequency is ramped from lower to higher frequencies, ions are ejected out of the trap in order of decreasing *m*/*z*. The field and geometry of the trap were set to preferentially eject the ions toward the center of the rings (toward $r = 0$, in the radial direction). Once an ion is ejected from the trapping volume toward the center of the rings, it is accelerated toward the detector. The discrete dynode detector (ETP, SGE, Austin, TX) collects the positive ions ejected from the trap. The output of the detector is fed into an integrating amplifier and from there to the DAQ board in the computer. Figure 3.4 shows the time intervals and sequence for ionization, RF trapping, and ejection.

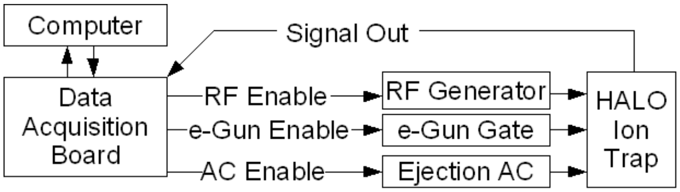

Figure 3.5. Control diagram for the Halo IT. The RF, e-gun, and ejection AC are all enabled by the computer through the DAQ board. The ejection AC is also modulated (amplitude) via the DAQ board. The frequency modulation for the ejection AC is provided by an arbitrary waveform generator.

3.2.6 Instrument control and data acquisition

The ion trap was controlled by a computer through a BNC-2110 data acquisition board (National Instruments, Austin, TX). The control software used was Labview 7.1. Figure 3.5 shows the data flow of the system. The computer/DAQ board provided the enabling pulses for the trapping RF, ionization, and the ejection AC. The computer/DAQ board also read the signal from the detector.

3.3 Results and Discussion

3.3.1 Arbitrary field generation

An electrostatic field in free space must obey Laplace's equation, $\nabla^2\Phi = 0$. In practical systems, the free space region is bounded by surfaces, and the problem of determining the field in free space reduces to the problem of defining the potential at every point on the boundary. From the potentials on the boundaries, one can determine the potential profile in free space. The inverse problem is closely related; i.e., choosing a desired potential profile in free space (such as a quadrupole potential) and then determining the boundary conditions that will produce the desired field profile. In other types of ion traps, the boundaries are selected to be equipotential surfaces. As a result, the boundaries can be established using conductors, and generally, the desired field profile is produced with relatively few electrodes. The shapes of these electrodes are determined by the field profile in free space, and with this approach, one is not free to select arbitrary boundary shapes. In most cases, the shapes of the field-defining electrodes do not correspond to shapes that are easy to machine.

In this work, we used an alternative approach for field generation, which is to start by defining the geometry of the boundary surfaces and then apply a different potential to each point on the surfaces to generate the desired potential in free space. Within a restricted volume, this approach is, in theory, capable of accurately synthesizing the desired field profile. This approach is similar in principle to that used by Wang and Wanczek.[26] By using this approach, it is possible to select simple geometries for the field-defining surfaces, such as planes and cylinders. The difficulty, however, is that every point on the surface requires a different potential. Rather than using an infinite number of potentials, a finite number of separate voltages can be used by taking advantage of the smoothing effect that occurs in electrostatic fields; i.e., discontinuities in the field become rapidly smoothed out as one moves away from the electrodes. Therefore, a good approximation to the desired field profile in the region of interest is achieved by selectively placing a series of finite-sized electrodes on the field-defining surfaces and setting an appropriate voltage at each point. A thin resistive layer between these electrodes further smoothes the potential function. Figure 3.6 shows a SIMION 7.0 simulation of the fields produced using this method. Both the potential and field functions are shown along the plane midway between the two plates. Near the center of the trapping region, the radial field is nearly linear.

In most ion traps, analysis of electric fields is typically done by projecting the fields onto the cylindrically symmetric Legendre polynomials (quadrupole, octopole, hexapole, etc.). Ion trap performance is then related to the amount and type of higher field contributions present. For the toroidal geometry, however, this derivation of fields is not strictly valid, and to date, no rigorous solution has been presented. For instance, the fields shown in Figure 3.6 are primarily

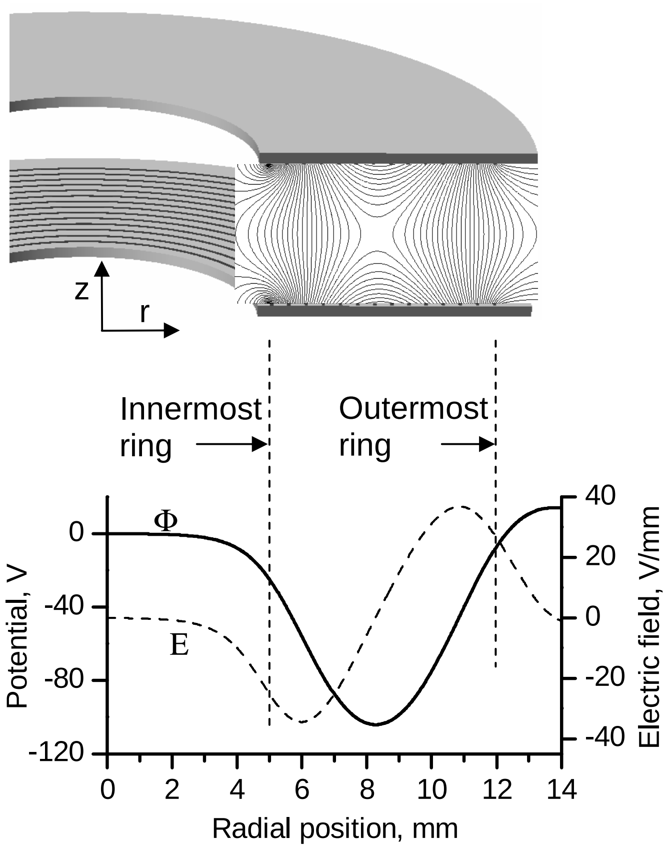

Figure 3.6. Equipotential surfaces in the halo IT, as calculated using SIMION (top); and plot of the potential, Φ, and electric field magnitude, E, as a function of radial position, measured on the plane equidistant between the two plates (bottom).

quadrupolar in the plane of the figure, but the figure does not show the curvature out of this plane. Also, whereas an ideal quadrupole field centered on the origin extends to infinity in every direction, a similar field in toroidal geometry, centered in the trapping region, would violate Laplace's equation at the rotational axis of the torus. It is, thus, not yet clear: (1) how higher-order fields are defined in this geometry and (2) what effect such fields will have on mass analysis. As a result, the fields in Figure 3.6 have not been analyzed, and are only shown for illustrative purposes. A possible advantage of this method of producing trapping fields is that modification of the field shapes can be done simply by changing the potentials on the rings, rather than physical modification of the electrodes (i.e., increasing the spacing between electrodes).

3.3.2 Performance characteristics of the halo ion trap

Preliminary mass spectra for dichloromethane and toluene are shown in Figure 3.7. The spectra were obtained by sweeping the resonant ejection frequency from 50 to 600 kHz in 100 ms. The RF frequency was 1.9 MHz. Figure 3.7A shows an average of four spectra of dichloromethane at a pressure of 7.6×10^{-5} mbar. Helium buffer pressure was 1.8×10^{-3} mbar. The RF amplitude was 500 $V_{p\text{-}p}$, and the resonance ejection AC amplitude was 656 $mV_{p\text{-}p}$. The expected isotopic peak doublet at *m*/*z* 49/51 is clearly resolved. The mass resolution for the peak at m/z 49 is measured as 0.64 Da FWHM. The isotopic molecular peak triplet at *m*/*z* 84/86/88 can also be seen, but is not clearly resolved. Figure 3.7B shows the average of four spectra of toluene. Sample pressure was 9.9×10^{-6} mbar, and helium buffer pressure was 2.7 × 10-3 mbar. The RF amplitude was 626 $V_{p\text{-}p}$, and the resonance ejection AC amplitude was 938 $mV_{p\text{-}p}$. Measurement of the mass resolution for the molecular peak at *m*/*z* 92 showed 1.3 Da FWHM, so the peak doublet that should be at *m*/*z* 91/92 is not resolved. The fragment peaks at *m*/*z* 63/65 are clearly resolved.

Simulations of the halo IT using SIMION 7.0 indicated that the standard mass-selective instability scan would not work with this trap. Specifically, ions are ejected onto the plates themselves, rather than into the center. For this reason, resonance ejection was used to obtain spectra. Due to limitations of our electronics, we used a mass analysis scan in which the resonance ejection frequency was scanned, while holding the driving RF amplitude and frequency constant. Although we used a frequency scan of the resonance ejection signal,

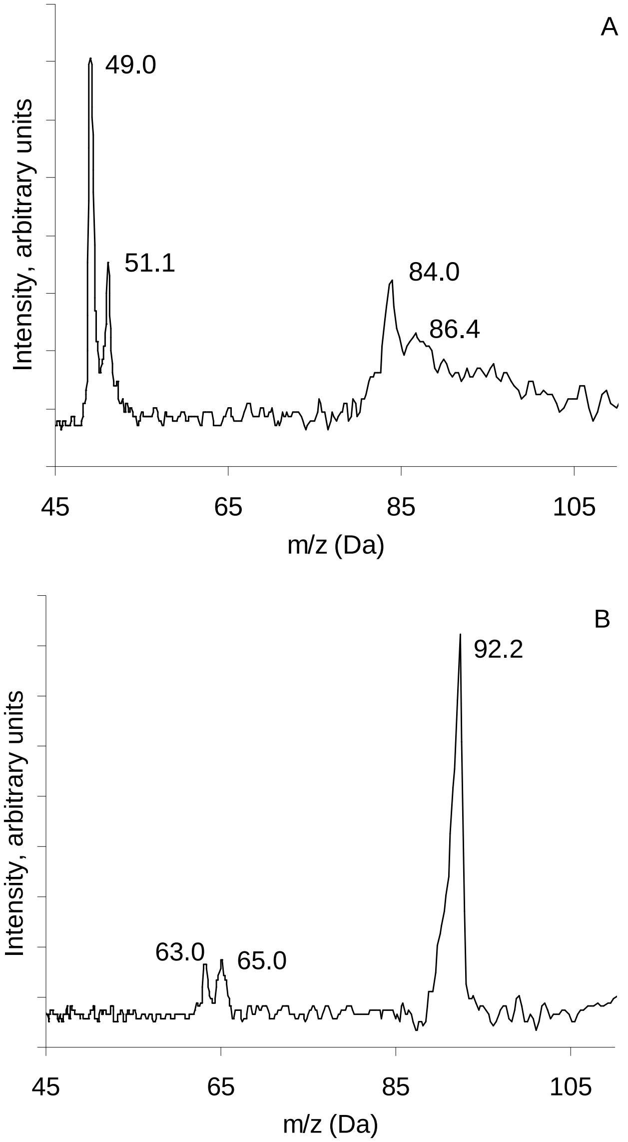

Figure 3.7. (A) Mass spectrum of dichloromethane recorded with the halo IT; FWHM mass resolutions for the m/z 49.0 and 51.1 peaks are, respectively, 0.64 and 0.83 Da; (B) mass spectrum of toluene; FWHM mass resolution for the m/z 92.2 peak is 1.3 Da.

presumably other types of resonance ejection scans would also work, and may improve resolution.

The effects of varying ionization time and helium collision gas pressure were studied using toluene as analyte. Ionization times ranged from 5 to 95 ms. As the ionization time increased from 5 to 45 ms, the signal intensity also increased. Above 45 ms, however, the intensity remained constant, but resolution deteriorated. Mass resolution improved as helium pressure increased from 1×10^{-4} to 1×10^{-3} mbar. This result is consistent with observations in other types of ion traps. The highest mass of the device is currently limited to 112 Da by the electronics, although a higher range would likely be possible by changing the driving RF amplitude or frequency. Other aspects of the halo IT performance may also be limited by the electronics, such as stability of the RF amplitude.

We anticipate several performance advantages due to the unique structure of the halo IT. For instance, the toroidal trapping volume is much greater than the trapping volume in traditional QITs. For full-sized traps, this translates into increased dynamic range and reduced space-charge effects on mass resolution. Ions in standard size (r_0 = 1 cm) hyperbolic and cylindrical traps are cooled to a small region at the trap center with radius of roughly 0.5 mm,[27] resulting in an effective trapping volume of roughly 0.5 mm^3. In contrast, ions in the halo IT are cooled to a ring between the plates. Assuming similar voltage gradients (so that the minor radius of the trapped ions is still 0.5 mm) and assuming the major radius of the ring of trapped ions is 8 mm, the trapping volume is increased to roughly 40 mm^3. Thus, for a given density of ions and a given level of mass resolution, the halo IT can contain ~80 times as many ions as a conventional quadrupole trap. This larger storage capacity, similar to that found in LITs, may allow greater sensitivity when using mass-selective trapping, better statistical factors when measuring ratios of small isotope peaks, and greater dynamic range. The larger volume is expected to result in improved sensitivity in a miniaturized device. Similarly, the open structure facilitates formation and trapping of ions; even if the device is small, the trapping volume remains easily accessible to electrons or ions, although externally injected ions must still overcome an RF barrier to be trapped. Significant work remains to be done, both in improving the halo trap design and in quantitative characterization of trapping capacity, sensitivity, and other parameters.

At a more general level, an advantage of producing arbitrary fields using rings is that less volume is wasted within the trapping structure. In hyperbolic ion traps, a perfect quadrupolar field requires that the electrodes be infinitely large. In practice, electrodes are truncated at 2–3 times the characteristic trap radius, a compromise between the field nonlinearity caused by truncation and device size and power. However, most of the volume is not used for trapping. In cylindrical and rectilinear traps, volume is also wasted because of field imperfections near the electrode surfaces. With an arbitrary field based on electrode rings, however, the electrodes do not have to follow equipotential surfaces. Rather, the field can be made to appear as though electrodes extend much farther. In this case, the electrodes can be located very close to the trapping region, so device size is minimized.

3.4 Conclusions

The halo IT combines the advantages of a toroidal trapping geometry with a novel fabrication method utilizing microfabrication lithography. Although the device reported here is not miniaturized in the traditional sense, aspects such as open access to ions or electrons, large ion storage volume, fabrication method, and the ability to electrically optimize trapping fields make the halo trap well-suited to future miniaturization efforts. Initial spectra are promising, although improvements in the exact form of trapping potentials, mass analysis scan functions, and other details will result in an improved instrument.

This work also demonstrates the method of arbitrary field generation in ITs. Time-dependent electric fields are not produced using curved three-dimensional metal surfaces, as in other ITs, but rather using 2D arrays of quasi-independent electrode rings. Using this method, the shapes of trapping potentials can be changed electronically, without physical modification of the trap electrodes. This same method also allows the exterior of the trap to be open for easy ion, sample, or ionizing electron admittance, while maintaining trapping fields in the interior of the device.

3.5 References

1. March, R. E.; Todd, J. F. J. *Quadrupole Ion Trap Mass Spectrometry*, 2nd ed.; John Wiley & Sons, Inc.: Hoboken, NJ; 2005.
2. Badman, E. R.; Cooks, R. G. *J. Mass Spectrom.* 2000, *35*, 659–671.
3. Paul, W.; Steinwedel, H. *Z. Naturforsch.* 1953, *8A*, 448–450.
4. Mather, R. E.; Waldren, R. M.; Todd, J.F. J.; March, R. E. *Int. J. Mass Spectrom. Ion Phys.* 1980, *33*, 201–230.
5. Schwartz, J. C.; Senko, M. W.; Syka, J. E. P. *J. Am. Soc. Mass Spectrom.* 2002, *13*, 659–669.
6. Ouyang, Z.; Wu, G.; Song, Y.; Li, H.; Plass, W. R.; Cooks, R. G. *Anal. Chem.* 2004, *76*, 4595–4605.
7. Lammert, S. A.; Plass, W. R.; Thompsom, C. V.; Wise, M. B. *Int. J. Mass Spectrom.* 2001, *212*, 25–40.
8. Franzen, J.; Gabling, R.-H.; Schubet, M.; Wang, Y. Nonlinear ion traps, in *Practical Aspects of Ion Trap Mass Spectrometry*; March, R. E., Todd, J. F. J., Eds.; CRC Press: Boca Raton, FL, 1995; Vol. 1, pp 69.
9. Prestage, J. D.; Chung, S.; Burt, E.; Maleki, L.; Tjoelker, R. L. In *Stability Measurements between Hg^+ LITE 12-Pole Clocks*, Proceedings of the 2002 IEEE International frequency Control Symposium and PDA Exhibition, New Orleans, LA, May 29–31, 2002.
10. Prestage, J. D.; Dick, G. J.; Maleki, L. *J. Appl. Phys.* 1989, *66*, 1013–1017.
11. Arkin, C. R.; Goolsby, B.; Laude, D. A. *Int. J. Mass Spectrom.* 1999, *190–191*, 47–57.
12. Song, Y.; Wu, G.; Song, Q.; Cooks, R. G.; Ouyang, Z.; Plass, W. R. *J. Am. Soc. Mass Spectrom.* 2006, *17*, 631–639.
13. Patterson, G. E.; Guymon, A. J.; Riter, L. S.; Everly, M.; Griep-Raming, J.; Laughlin, B. C.; Ouyang, Z.; Cooks, R. G. *Anal. Chem.* 2002, *74*, 6145–6153.
14. Wells, J. M.; Badman, E. R.; Cooks, R. G. *Anal. Chem.* 1998, *70*, 438–444.
15. Badman, E. R.; Johnson, R. C.; Plass, W. R.; Cooks, R. G. *Anal. Chem.* 1998, *70*, 4896–4901.
16. Riter, L. S.; Peng, Y.; Noll, R. J. Patterson, G. E.; Aggerholm, T.; Cooks, R. G. *Anal. Chem.* 2002, *74*, 6154–6162.
17. Austin, D. E.; Cruz, D.; Blain, M. G. *J. Am. Soc. Mass Spectrom.* 2006, *17*, 430–441.
18. Pau, S.; Pai, C. S.; Low, Y. L.; Moxom, J.; Reilly, P. T. A.; Whitten, W. B.; Ramsey, J. M. *Phys. Rev. Lett.* 2006, *96*, 120801.
19. Douglas, D. J.; Frank, A. J.; Mao, D. *Mass Spectrom. Rev.* 2005, *24*, 1–29.
20. Gao, L.; Song, Q.; Patterson, G. E.; Cooks, R. G.; Ouyang, Z. *Anal. Chem.* 2006, *78*, 5994–6002.

21. Lammert, S. A.; Rockwood, A. A.; Wang, M.; Lee, M. L.; Lee, E. D.; Tolley, S. E.; Oliphant, J. R.; Jones, J. L.; Waite, R. W. *J. Am. Soc. Mass Spectrom.* 2006, *17*, 916–922.
22. Blain, M. G.; Riter, L. S.; Cruz, D.; Austin, D. E.; Wu, G.; Plass, W. R.; Cooks, R. G. *Int. J. Mass Spectrom.* 2004, *236*, 91–104.
23. Badman, E. R.; Cooks, R. G. *Anal. Chem.* 2000, *72*, 5079–5086.
24. Badman, E. R.; Cooks, R. G. *Anal. Chem.* 2000, *72*, 3291–3297.
25. Tabert, A. M.; Griep-Raming, J.; Guymon, A. J.; Cooks, R. G. *Anal. Chem.* 2003, *75*, 5656–5664.
26. Wang, Y.; Wanczek, K. P. *J. Chem. Phys*. 1993, *98*, 2647–2652.
27. Hemberger, P. H.; Nogar, N. S.; Williams, J. D.; Cooks, R. G.; Syka, J. E. P. *Chem. Phys. Lett.* 1992, *191*, 405–410.

CHAPTER 4. HALO ION TRAP WITH AXIAL EJECTION

4.1 Introduction

With its inherent high sensitivity, compact analyzer size, and high specificity, ITMS[1] has been widely accepted for many applications, including cosmic exploration,[2,3] threat and forensic detection,[4,5] identification of chemical and biochemical compounds in pure form or in complex mixtures,[6,7] and environmental monitoring.[8,9] Other major advantages that enhance the attractiveness of ITMS for field portable applications[10] include simple construction, relatively high pressure operation compared to other mass analyzers, low power consumption, and the ability to perform multi-stage tandem MS in a single analyzer.

The conventional quadrupole IT was originated by Paul in 1953.[11] A hyperbolic ring electrode between two hyperboloidal endcap electrodes produces a time-dependent quadrupole electric field when an RF voltage is supplied to the ring electrode. Current commercial IT mass spectrometers typically have a trap radius (r_0) of approximately 1 cm and are operated with an RF trapping voltage on the order of 15 $kV_{p\text{-}p}$. For portable analysis by ITs, it is desirable both (1) to reduce electrical power by operating the trap using a lower voltage, and (2) to reduce the trap dimensions (z_0 and r_0). At the same time, the RF frequency must be increased to maintain an adequate pseudopotential well depth. However, smaller IT mass analyzers are more subject to space charge performance degradation.[12] One of the solutions to this problem is to increase the ion storage capacity of the trap without increasing its characteristic trapping dimensions (z_0 and r_0). Recently, several groups[13-18] have investigated various IT geometry designs to maintain ion capacity while miniaturizing the analyzer. The toroidal IT,[19,20] reported by Lammert et al., is comprised of four hyperboloidal electrodes: two endcaps, an inner ring, and an outer ring, which form a toroidal trapping geometry. RF trapping voltage supplied to the two ring electrodes forces ions to focus in a circular band rather than at a point as in a 3D quadrupole IT, thus maintaining the ion storage volume while significantly decreasing the characteristic trapping dimensions. This miniature device, with a 2.5-mm trapping field radius, has approximately the same ion storage volume as a commercial IT mass analyzer with a 1 cm radial dimension, but operates at RF voltages around 1 kV_{p-p} instead of the 15 kV_{p-p} typical of commercial quadrupole ITs. Unit mass resolution was obtained for toluene, dibromochloromethane and diethylphthalate, which is comparable to resolution values observed from most bench-top GC-MS systems.[4] However, improvement in the performance of the toroidal IT is limited to a large degree by the machining tolerances,[20] which are specified to 0.0005 inch (0.013 mm) for the electrodes and which are at or near the limits of current machining capabilities.

The halo IT mass analyzer,[21] which has a circular trapping geometry analogous in shape and size to the toroidal IT, was recently reported by our group. It consists of two patterned parallel ceramic plates made by microlithography. The toroidal trapping volume is located between the two plates, which is produced not by hyperboloidal electrodes, but rather by a number of concentric electrode rings fabricated on the two facing planar surfaces. By the same process, we have also created a conventional Paul ion trapping field between two ceramic plates, which demonstrates better resolution than the halo IT.[22] While the halo IT possesses a similar trapping volume as the toroidal IT, its open structure provides much greater access for electron ionization. The use of microlithographic methods to fabricate the traps resolves the issue of close machining tolerances, and all ITs fabricated in this manner can be further miniaturized without being limited by machining tolerances. By adjusting the array of the electrode rings (i.e., number of rings and spacing between rings) and the voltages applied to the rings, the radius of curvature

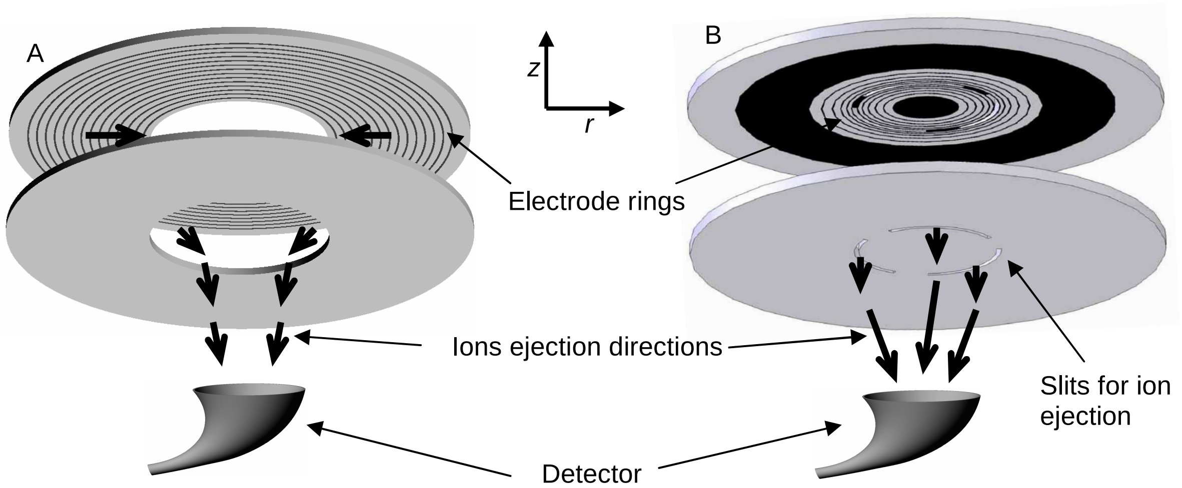

Figure 4.1. Schematic diagrams (not to scale) of (A) previous and (B) new halo IT mass analyzer designs.

of the toroidal trapping field can be changed to modify the shape and size of the ion storage volume.

In the halo IT described in the last chapter, the trapped ions were resonantly ejected radially to the center of the plates (in the *r* direction), as shown in Figure 4.1A, and then drawn by a high negative voltage through a hole in the middle of one of the plates to an orthogonally positioned detector. The spatial spread of ions in the *r* direction across the trapping field as well as spatial dispersion that occurs when the ions turn 90º from the trap to the detector compromise the peak intensity. Furthermore, the high voltage on the detector could interfere with the quadrupolar trapping field, degrading the resolution. Efforts to shield the trapping field from the detector voltage by inserting a hollow copper cylinder into the center hole did not solve this problem.

In the toroidal IT,[19] trapped ions are ejected through three equally spaced 93° arc slits in the endcap electrodes rather than through the inner electrode. The slits in one endcap electrode serve as the entrance for energetic electrons from the filament, and the slits in the other endcap electrode provide an exit passway for resonantly ejected ions in the axial direction (i.e., in the *z* direction) to the detector. In an attempt to improve the resolution of the halo IT, we simulated the resonant ejection of ions in the axial (*z*) direction instead of in the radial direction and found that axial ejection should improve resolution and ejection efficiency. Therefore, in this study, three equally spaced 92° arc slits for ion ejection were machined in each of the trapping plates (Figure 4.1B) at the same radius as in the toroidal IT.

It is well known that the mass resolution in ITMS is affected by the presence of multipole fields. A number of investigations of multipole field components in trapping fields of conventional quadrupole,[1,23] cylindrical,[24] and rectilinear ITs[17] have been made to understand the behavior of trapped ions and to optimize the performance of the ITs. Certain amounts and types of higher-order multipole fields can increase the speed with which ions accumulate energy during dipole ejection to improve the ITMS resolution. To date, no detailed studies have been made of the effects of higher-order fields on the performance of toroidal trapping fields. In fact, the curvature of the toroidal trapping area contributes additional multipole components to the electric field compared to the normal quadrupole IT.[19] Therefore, determination of the higher-order components in the toroidal field is an important step in the optimization of the performance of the halo IT.

In this chapter, the halo IT plates were modified by machining thin slits in the sixth electrode rings in order to determine if axial ejection of ions would improve ITMS resolution compared to radial ejection. Furthermore, a variety of potential distributions were simulated and then applied across the series of halo IT electrode rings to study the effects of higher multipole components on resolution. Both efforts were designed to improve the overall resolution of the halo IT.

4.2 Theory

The electrical potential[23] in a quadrupole ion trap with cylindrical symmetry can be expressed in spherical coordinates (ρ,θ,φ) as

$$\Phi(\rho,\theta,\phi,t)=\Phi_0(t)\sum_{l=0}^{\infty}A_l\left(\frac{\rho}{r_N}\right)^l P_l(\cos\theta) \tag{4.1}$$

where Φ_0 is the RF voltage applied to the ring electrode while the endcap electrodes are grounded, r_N is the normalization radius (normally the inner radius of the ring electrode), A_l is the expansion coefficient of the order l, and $P_l(\cos\theta)$ is the Legendre polynomial of order l. The values of $l = 0, 1, 2, 3, 4$……represent monopole, dipole, quadrupole, hexapole, octopole……as a multipole expansion for a given potential distribution. The quadrupole term gives the main contribution of the potential in the IT.

For an RF quadrupolar device with toroidal geometry, the form of a quadratic electric potential in cylindrical coordinates r and z in the axial direction of the toroidal IT can be expressed as[19]

$$\Phi(r,z)=\lambda(r-R)^2+\mu z^2 \tag{4.2}$$

where R is the distance from the trapping center to the rotational axis, and λ and μ are arbitrary constants. The potential in the toroidal region is constrained by the Laplace equation, which in cylindrical coordinates takes the form

$$\nabla^2\Phi(r,z)=\frac{1}{r}\frac{\partial}{\partial r}\left(r\frac{\partial\Phi}{\partial r}\right)+\frac{\partial^2\Phi}{\partial z^2}=2\lambda\left(2-\frac{R}{r}\right)+2\mu=2\lambda\left(2-\frac{R}{R+s}\right)+2\mu=0 \tag{4.3}$$

where s is defined as

$$s=r-R \tag{4.4}$$

From equation 4.3, the quadrupole electric potential distribution can only be generated for two cases

$R = 0$, then $\lambda = 1$, $\mu = -2$, resulting in a three-dimensional (3D) quadrupole IT (4.5)

$R \rightarrow \infty$, then $\lambda = -\mu = 1$, resulting in a two-dimensional (2D) linear IT (4.6)

Thus, the existence of a purely quadrupolar electric field in a toroidal trapping region is impossible, as are any pure higher-order multipole fields. However, if the curvature of the toroidal region is small enough, i.e., $s << R$, a nearly quadrupolar field is obtained in the vicinity of the trapping center. In this case, equation 4.3 reduces to

$$\lambda + \mu = 0 \tag{4.7}$$

similar to a 2D linear IT. Thus, the toroidal trapping field more closely resembles a 2D quadrupolar field than a 3D quadrupolar field.

Although pure multipoles (including quadrupole) electric fields do not exist in toroidal systems, similar effects induced by multipole fields still are observed in a toroidal trap. For the sake of convenience, throughout this chapter, multipole-like components in a toroidal trap are still applied by using the same terms used in conventional ITs.

For a primarily quadrupole device, the A_0 term (monopole) does not produce an electric field and, therefore, does not affect the behavior of ions. The odd ordered field components are zero for a toroidal trapping field because of symmetry about the plane perpendicular to the rotational axis. Thus, the potential distribution for the toroidal shape for the quadrupole (A_2), octopole (A_4) and dodecapole (A_6) terms can be approximated as[25]

$$\Phi(s,z,t) = \Phi_0(t)\left[A_2\left(\frac{z^2 - s^2}{r_N^2}\right) + A_4\left(\frac{z^4 - 6z^2s^2 + s^4}{r_N^4}\right) + A_6\left(\frac{z^6 - 15z^4s^2 + 15z^2s^4 - s^6}{r_N^6}\right)\right] \tag{4.8}$$

The potential along the z direction in the center of the toroidal trapping region can be evaluated at $s = 0$ in the above equation as

Table 4.1. Dimensions and positions of the electrode rings on the ceramic plates.

Ring number	Inner radius (mm)	Outer radius (mm)
1	0.0	2.8
2	3.5	3.6
3	4.2	4.3
4	4.8	4.9
5	5.3	5.4
6	5.7	6.3
7	6.6	6.7
8	7.1	7.2
9	7.8	7.9
10	8.7	8.8
11	9.8	16.0

$$\Phi(z,t)_{s=0} = \Phi_0(t)\left[A_2\left(\frac{z}{r_N}\right)^2 + A_4\left(\frac{z}{r_N}\right)^4 + A_6\left(\frac{z}{r_N}\right)^6\right] \quad (4.9)$$

where $\Phi_0(t)$ is the RF voltage on the ring electrode, A_l is a dimensionless coefficient for the l^{th} order, and r_N is the corresponding normalization radius. Since the halo IT more closely resembles a 2D quadrupole, equation 4.9 was used in the present work to approximate the higher order components, i.e., octopole (A_4/A_2) and dodecapole (A_6/A_2), along the z direction at the minimum of the radial potential ($s = 0$).

4.3 Experimental Section

4.3.1 Fabrication of the halo IT with axial ejection slits

Figure 4.1B shows the design of the halo IT with machined slits in the 6th electrode ring. The mass analyzer was comprised of two parallel ceramic plates with eleven concentric electrode rings, assembled face to face with each other and separated by a distance of 5.06 mm. Table 4.1 lists the dimensions of the electrode rings and the separation distances between successive concentric rings. The design of the plates for axial ejection was taken from the toroidal IT geometry, since it was already shown to give good mass resolution. The slits had a radius at 6

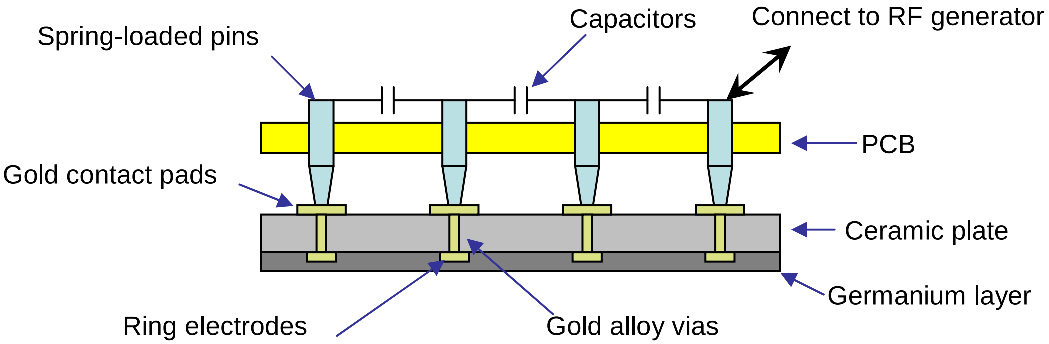

Figure 4.2. Schematic diagram illustrating the design for connection of the capacitor network to the electrode rings.

mm, which are the same as in the toroidal IT. Eleven electrode rings were fabricated on each trapping plate to allow the generation of a wide variety of electric fields. The slits had to be machined in one of the electrode rings to avoid surface charging during ion ejection. The 6th electrode ring was chosen for machining the ejection slits in order to leave the same number of electrode rings (5 rings) on either side to produce desired electric field. After simulations in SIMION, a toroidal trapping volume the same size as in the toroidal IT was produced at the slits when appropriate potentials were added to the electrode rings.

A detailed description of the fabrication of the trapping plates was given in the previous chapter.[21] The plates were constructed from alumina substrates (50.0-mm diameter, 0.64-mm thickness, 99.6% purity, Hybrid-Tek, Clarksburg, NJ). Holes and slits in the ceramic plates were machined by laser cutting. Three equal distance 3.91-mm diameter holes were machined 20.3 mm distance from the center for positioning three 6.35-mm diameter stainless steel balls to ensure accurate and precise spacing and parallel alignment of the trapping plates. The accuracy of plate alignment is limited by the placement precision of the laser-drilled holes, which was specified as ± 12 μm, but may be much tighter. The expected upper limit of misalignment is ± 10 μm in the *z* direction and ± 12 μm in the *r* direction. Two smaller holes (127-μm diameter) were laser drilled in each electrode ring and filled with a gold-tungsten alloy to serve as vias for electrically connecting the electrode rings to gold contact pads on the opposite side of the substrate. Finally, three equally spaced 92° arc slits with 6-mm radius and 0.4-mm width were cut by laser in the ceramic plates to function as axial ejection exits. The electrode rings were lithographically patterned on the ceramic plates and covered with a thin semiconducting germanium coating in a clean room facility as described previously.[21] Approximately, 50% of the plates fabricated according to this design were useful in making measurements.

A series of printed circuit boards (PCBs) were fabricated with spring-loaded contact pins that matched the contact pads on the ceramic plates. Each PCB contained a different capacitor network that determined the specific RF voltages to be applied to the individual electrode rings (Figure 4.2) in order to test the desired multipole electric fields. The capacitance between each ring was measured using a capacitance/conductance meter (HP 4280A 1MHz C Meter/C-V Plotter, Hewlett-Packard, Palo Alto, CA). Differences between measured and intended capacitor values were typically between 0.1 and 0.8%. The resulting errors in the octopole and dodecapole field components for each design were calculated using SIMION, and were found to be less than 0.02 of the magnitude of the octopole and dodecapole, respectively (that is, for a stated 5% octopole (A_4/A_2), the measured error was {5 ± 0.001}%). This level is likely to be less significant than factors such as capacitor heating, RF noise, and simulation/calculation error.

4.3.2 Experimental Setup

The experimental setup to test the modified halo IT design was identical to that described previously.[21] Briefly, the halo ITMS system included a home-built electron gun, halo IT mass analyzer, discrete dynode electron multiplier detector, RF waveform generator, arbitrary waveform generator, and control and data acquisition system. The electron gun was gated by changing the bias voltage from -70 to +120 V on the filament (W5, Scientific Instrument Services, Ringoes, NJ) with a 1.7-A current to control the ionization time. A custom-built RF generator was used to apply a 1.7-MHz sinusoidal waveform with amplitude up to 900 $V_{p\text{-}p}$ to the capacitor network on the PCB for trapping of ions, as shown in Figure 4.2. For monopole ejection, an AC signal was frequency swept using an arbitrary waveform generator (33250A, Agilent Technologies, Santa Clara, CA), which was amplified up to 10 $V_{p\text{-}p}$ using a custom-built amplifier. For dipole ejection, the signal from the custom-built amplifier was further converted into two signals with 180º phase difference using a custom-built converter. The ejection signal (either before the converter for monopole or one of the two phase different signals after the converter for dipole) was connected to the 6th electrode ring (where the slits are located) on the ceramic plate farthest from the detector, which was spread to the other electrode rings on the same plate by the capacitor network. The 6th electrode ring in the other plate (i.e., the plate closest to the detector through which the ejected ions pass) was grounded for monopole ejection, or connected to the out-of-phase signal after the converter for dipole ejection. The discrete dynode detector (AF138, ETP, SGE, Austin, TX) at -1.9 kV was used to collect positive ions ejected from the trap. The output of the detector was amplified with a transconductance of 128 MΩ using a custom-built integrating amplifier and fed into the DAQ board on a computer. The halo IT system was controlled using a PC through a BNC-2110 data acquisition board (National Instruments, Austin, TX). The control and data handling software was Labview® 7.1.

The halo IT was enclosed in a custom-built vacuum chamber pumped using a 520 L/s turbomolecular pump (Pfeiffer, model TMH 520-020, Asslar, Germany). Sample headspace vapors and helium buffer gas were introduced directly into the vacuum chamber via precision needle leak valves (Nupro/Swagelok, Solon, OH) at pressures of 10^{-5} mbar and 10^{-4} mbar, respectively, which were measured using a full-range cold cathode vacuum gauge (Pfeiffer, model PKR 251/261, Asslar, Germany). All pressure readings reported in this paper are uncorrected. Mass spectra shown here were calibrated using various samples, such as benzene, toluene, dichloromethane, heptane, chlorobenzene, and nonane under the same operating parameters.

4.3.3 Computation Methods

According to the superposition principle in electric field theory, the coefficients for each order (i.e., quadrupole, octopole and dodecapole in equation 4.9) for all rings in the halo IT can be summed to provide the overall multipole field component to the total electric field. SIMION 8.0 and MATLAB R2008b were used to calculate the A_2, A_4 and A_6 dimensionless multipole coefficients.[26] The resultant multipole components of the total electric field in the halo IT were calculated by multiplying the voltages applied to each ring by the various multipole coefficients, and summing all of the products of each multipole type. The various summed higher-order multipole percentages were obtained by dividing each summed higher-order multipole coefficient by the summed quadrupole coefficient, and then multiplying by 100% (i.e., A_4/A_2 for octopole, and A_6/A_2 for dodecapole). Finally, the SOLVER function in Microsoft Office Excel® was used to specify new voltages to apply to the electrode rings in order to adjust the multipole percentages to the desired values.

4.4 Results and Discussion

4.4.1 Performance of the halo IT with axial ejection

In the halo IT, ions are formed, trapped, and collisionally cooled within the toroidal field. In the original halo IT design,[21] a 9.14-mm-diameter center hole served as an exit for ions ejected from the trap during mass analysis (Figure 4.1A). During ejection, the trapped ions absorbed energy from the ejection signal and resonated in a direction parallel to the trapping plates (i.e., in the *r* direction), and then were drawn out through the center hole by the voltage on the detector. As shown in Figure 4.1B, in the modified halo IT, three 92° arc (6-mm radius) slits with 0.4-mm width were fabricated in the ceramic plates to allow direct axial ejection from the toroidal trapping field. In this new design, trapped ions resonate in a direction perpendicular to the trapping plates (i.e., in the *z* direction), and ultimately escape through the slits to the detector. From simulation using SIMION®, we observed that axial ejection should improve mass resolution compared to radial ejection.

Actual measurements using the new halo IT plate with axial ejection slits gave comparable peak intensities (Figure 4.3) to the older center ejection design, even though the total exit area through the slits was only approximately 0.176 times the area of the center hole. The center hole design was originally thought to provide high ion ejection transmission, however, the large negative voltage on the detector interfered with the ejection electric field. Consequently, ions with high energies were given trajectories that caused them to collide with the trapping plate instead of being drawn out through the center ejection hole, thus, significantly reducing ejected ion transmission efficiency. In contrast, axial ejection through the small slits gave similar ion transmission efficiency, even though the area through which the ions could escape from the trapping field was much smaller and only half of them could be ejected to the detector side for detection.

Mass spectral resolution was increased from approximately 100 ($m/\Delta m$) to 280 ($m/\Delta m$) when ion ejection was changed from radial to axial. The high order electric field components along the ejection (radial) direction in the original halo IT were calculated using SIMION as described in the experimental section, which gave an octopole (A_4/A_2) percentage of 24.3% and a

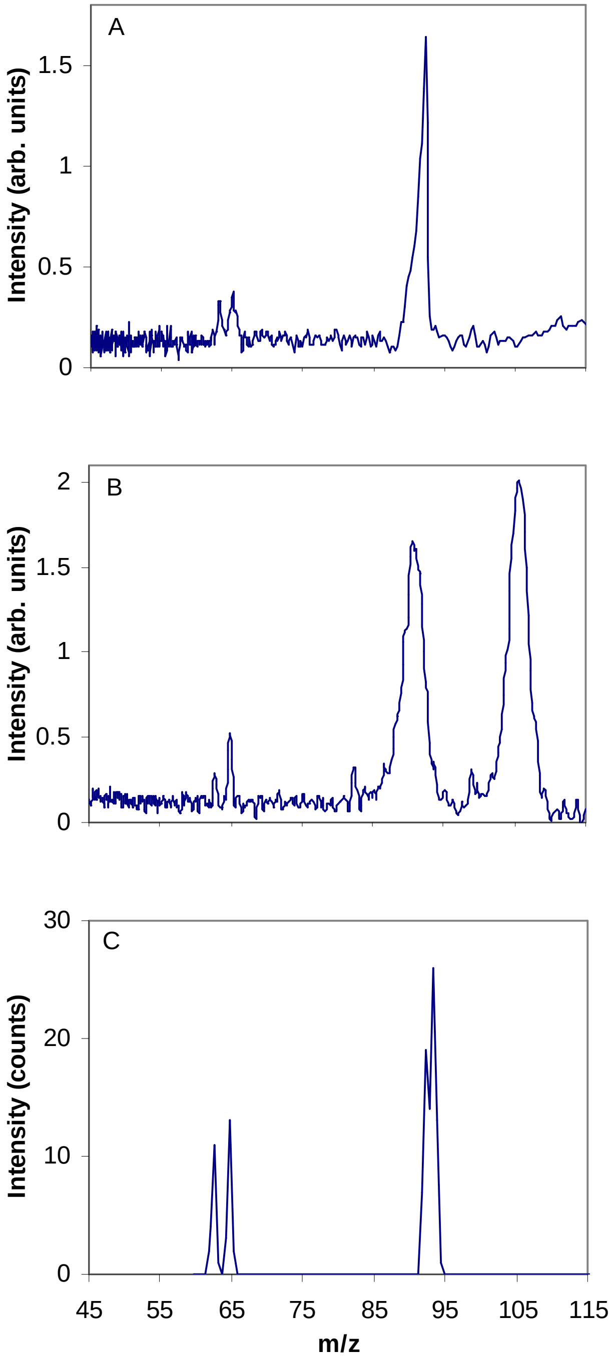

Figure 4.3. Toluene mass spectra obtained using (A) radial ejection, with 9.9 × 10^{-6} mbar sample pressure, 2.7 × 10^{-3} mbar helium pressure, 1.9 MHz RF frequency, 626 V_{p-p} amplitude, ejection AC frequency scanned from 50 to 600 kHz in 100 ms, 938 mV_{p-p} amplitude; (B) axial ejection, with 1.4 × 10^{-5} mbar sample pressure, 1.3 × 10^{-4} mbar helium pressure, 1.7 MHz RF frequency, 669 V_{p-p} amplitude, ejection AC frequency scanned from 640 to 100 kHz in 100 ms, 2.9 V_{p-p} amplitude with -0.8 V DC offset, dipole ejection; and (C) simulation of axial ejection (only ions with m/z values of 63, 65, 91 and 92). Note the presence in (b) of a peak at 105, the result of an ion-molecule interaction (H from tolyl ion exchanges with methyl from a neutral toluene).[22]

dodecapole (A_6/A_2) percentage of 1.6%. Such a high percentage of octopole field, which has the greatest influence on ion trapping among all of the multipole fields, was much higher than needed or desired. It lengthened the resonant ejection process, keeping the ions in the trapping field longer than necessary, and producing poor resolution as a result.

In the new design, trapped ions are ejected in the *z* direction through the slits. Therefore, the trapping center must be exactly in-line with the ejection slits. Simulation has shown that ions should be trapped in a very thin circular band exactly between the slits in the two ceramic plates under the electric field conditions we have considered in this work. In the toroidal IT,[19] geometric modification was made from symmetric to asymmetric geometry to intentionally add a slight nonlinear (mainly octopole) field to improve the performance of the device. Since the halo IT has the same trapping geometry, the higher order fields also play a very important role in the ejection of ions. Accordingly, they were studied in detail in order to optimize the performance of the new halo IT design.

4.4.2 Effect of percentage of octopole field component on performance of the halo IT

It was reported that the optimum performance of cylindrical ITs[24] and rectilinear ITs[17] was achieved when the sum of the percentages of the positive octopole field component and the negative dodecapole field component was approximately -10% in the axial direction. Since the curvature of the toroidal trapping geometry inherently produces higher order field components, as indicated in equation 4.3, it became necessary to determine their compositions in different electric fields and to investigate their effects on trap performance in order to optimize the performance of the halo IT. When we tried to constrain the percentages of the octopole and dodecapole field components, the dodecapole field component could not be more positive than -45% when the octopole field was kept below 10%. This was mostly due to the curvature of the toroidal geometry in the halo IT.[19] The electric fields in a toroidal trapping volume are not symmetric with respect to radial motion toward or away from the rotational axis. This asymmetry, which does not exist in other types of ITs, affects both the ion motion and the multipole fields. The influence of fields higher than dodecapole, such as hexadecapole (A_8), ikosipole (A_{10}), and tetraikosipole (A_{12}), on the performance of more conventional ITs have not previously received much attention because they are typically very small. Likewise, we did not consider their contributions to halo IT performance because the octopole and dodecapole components were likely much more important. In this work, we fabricated 4 sets of PCBs to generate 1%, 3%, 5% and 7% octopole fields (A_4/A_2) with constant -50% dodecapole field (A_6/A_2) to investigate the influence of octopole field percentage in the axial direction.

Three ejection modes were used to investigate the effects of different octopole field percentages: (1) RF amplitude ramp and ejection at the stability boundary, (2) RF amplitude ramp with constant resonant ejection frequency, and (3) resonant frequency scan with constant RF amplitude. The resonant frequency scan mode gave the highest ion intensity of the three excitation methods. Figure 4.4 shows the effects of octopole percentage on the mass spectra of benzene obtained from the halo IT using resonant frequency scan ejection. At 1% octopole field, the peaks at *m*/*z* 77 and 78 Da were narrow (1.2 Da FWHM) and partially separated with approximately 60% valley. At 3% octopole field, the molecular ion peak (i.e., 78 Da) was much wider (3.8 Da FWHM), and the resolution was reduced. A broad peak appears at *m*/*z* 90, possibly the result of an ion molecule reaction in the trap, such as the H/CH_3 exchange that occurs for toluene.[20] When the octopole field was increased to 5%, very narrow peaks were observed for the $C_4H_3^+$ and $C_4H_4^+$ fragments at *m*/*z* 51 and 52 Da (0.19 Da FWHM), however, peaks for 77 and 78 Da were unresolved, and the peak at 90 *m*/*z* is still present. Finally, for 7% octopole field,

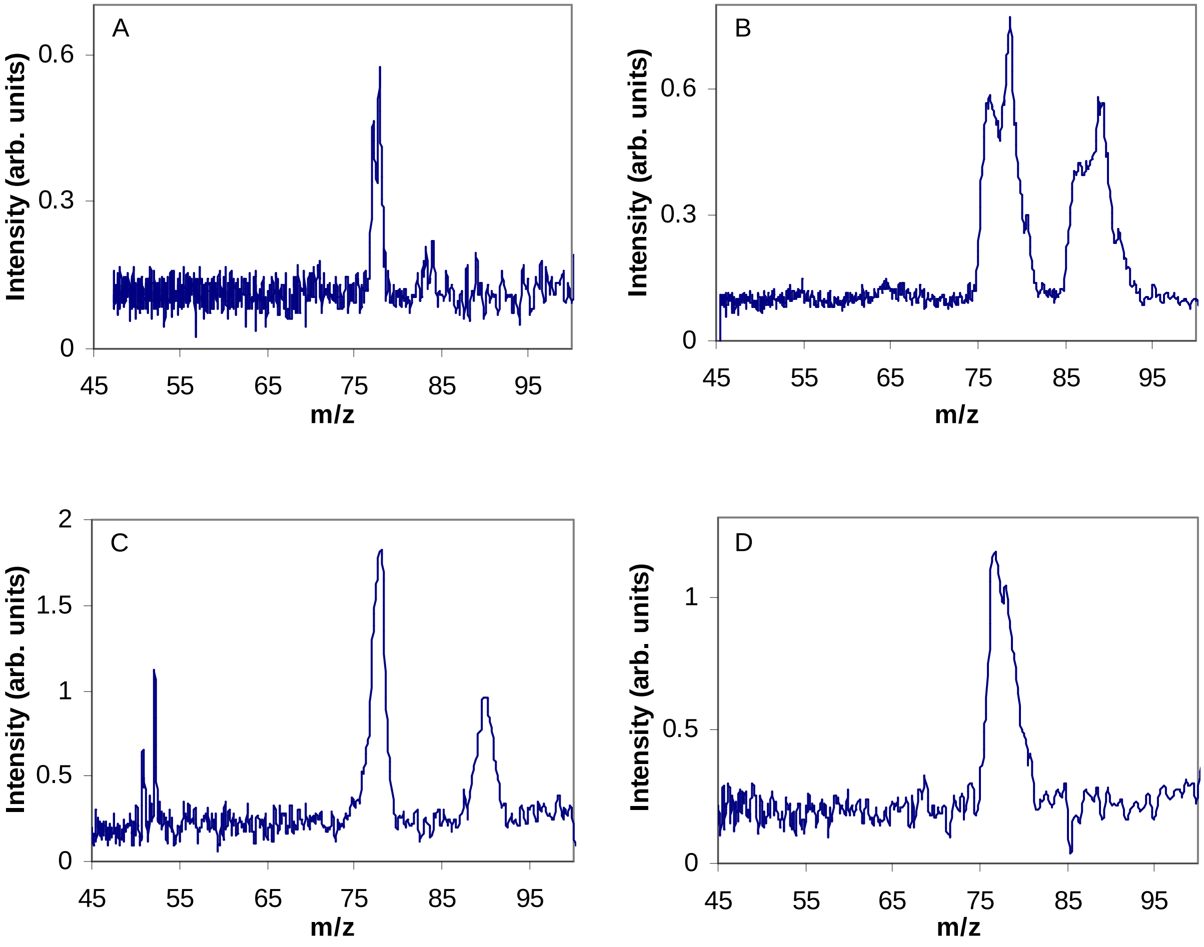

Figure 4.4. Benzene mass spectra obtained using trapping fields containing (A) 1% (2.9 × 10^{-5} mbar sample pressure, 5.8 × 10^{-4} mbar helium pressure, 1.7 MHz RF frequency, 910 $V_{p\text{-}p}$ amplitude, ejection AC frequency scanned from 600 to 80 kHz in 100 ms, 1.1 $V_{p\text{-}p}$ amplitude), (B) 3% (1.4 × 10^{-5} mbar sample pressure, 1.3 × 10^{-4} mbar helium pressure, 1.7 MHz RF frequency, 825 $V_{p\text{-}p}$ amplitude, ejection AC frequency scanned from 500 to 100 kHz in 100 ms, 2.6 $V_{p\text{-}p}$ amplitude with -2.0 V DC offset, dipole ejection), (C) 5% (2.0 × 10^{-5} mbar sample pressure, 1.1 × 10^{-4} mbar helium pressure, 1.7 MHz RF frequency, 644 $V_{p\text{-}p}$ amplitude, ejection AC frequency scanned from 640 to 100 kHz in 100 ms, 2.3 $V_{p\text{-}p}$ amplitude with -0.6 V DC offset, dipole ejection) and (D) 7% (3.6 × 10^{-5} mbar sample pressure, 3.1 × 10^{-4} mbar helium pressure, 1.7 MHz RF frequency, 657 $V_{p\text{-}p}$ amplitude, ejection AC frequency scanned from 650 to 100 kHz in 100 ms, 0.2 $V_{p\text{-}p}$ amplitude, dipole ejection) octopole field contributions.

the spectrum showed the poorest mass resolution of any set of conditions. Fragment peaks were only observed for 5% octopole field conditions, which also provided the best overall resolution for the low masses (e.g., 280 $m/\Delta m$ for m/z 51 and 52 Da and 52 $m/\Delta m$ for m/z 77 and 78 Da). The peak for m/z 90 Da in 3% and 5% octopole fields is probably products of fragment ion

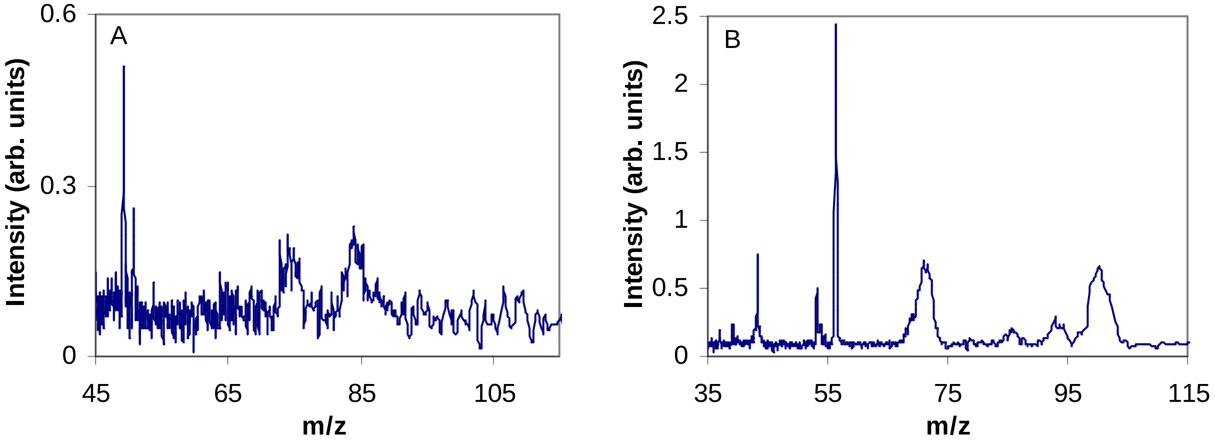

Figure 4.5. Mass spectra obtained using 5% octopole field contribution for (A) dichloromethane (3.7 × 10^{-5} *mbar sample pressure, 1.9 ×* 10^{-4} *mbar helium pressure, 1.2 MHz RF frequency, 485* $V_{p\text{-}p}$ *amplitude, ejection AC frequency scanned from 600 to 100 kHz in 100 ms, 0.3* $V_{p\text{-}p}$ *amplitude with -0.2 V DC offset, dipole ejection) and (B) heptane (2.8 ×* 10^{-5} *mbar sample pressure, 1.9 ×* 10^{-4} *mbar helium pressure, 1.2 MHz RF frequency, 360* $V_{p\text{-}p}$ *amplitude, ejection AC frequency scanned from 600 to 100 kHz in 100 ms, 1.2* $V_{p\text{-}p}$ *amplitude with -0.3 V DC offset, dipole ejection).*

condensations with benzene molecules[27] due to electron transfer by helium, which could be stable if the pressure was high enough. Both 1% and 3% octopole fields gave better results than the 7% octopole field. The strongest ion intensities were obtained for the 3% and 5% octopole fields. Of the field combinations studied, 5% octopole appears to give the best tradeoff of performance.

4.4.3 Performance of the halo IT with 5% octopole field

Mass spectra for dichloromethane and heptane are shown in Figure 4.5. The spectra were obtained using dipole ejection by sweeping the resonant ejection frequency. A few volts of DC offset were added to the ejection signal in order to obtain stronger peak intensity. From equation 4.7, the electric field in the halo IT more closely resembles that of a linear quadrupole than a 3D quadrupole IT. The secular frequencies in the axial and radial directions are equal for a linear quadrupole, and trapped ions will be resonantly excited in both directions simultaneously unless a DC voltage is used to differentiate the two secular frequencies such that ions are excited only in the axial direction.[19]

Figure 4.5A shows an average of ten spectra (as given by the Labview operating software) of dichloromethane taken sequentially. The fragment peaks at *m*/*z* 49 and 51 Da were clearly resolved with a mass resolution of 0.18 Da (FWHM for *m*/*z* 49 Da). However, the molecular ions at *m*/*z* 84/86/88 Da could not be resolved. Figure 4.5B shows an average of ten spectra (same as above) of heptane with resolution of 0.20 Da and 0.36 Da (FWHM) for the fragment peaks at *m*/*z* 43 Da and 57 Da, respectively. However, the peaks at *m*/*z* 71 and 100 Da are relatively wide. From these and other mass spectra not shown here, good resolution was only observed for ions with *m*/*z* values less than 70 Da. The largest and smallest ions observed in this work were *m*/*z* 198 and 38 Da, respectively. Fragments with *m*/*z* values lower than 38 Da were below the low-mass cut-off and could not be detected.

Simulations of the halo IT using SIMION® 8.0 also indicated that good mass resolution could be obtained in the low mass region, as shown in Figure 4.3C. In this simulation, ions with *m*/*z* at 63, 65, 91 and 92, matching the *m*/*z* values and relative abundances of the typical fragment ions of toluene, were generated between the two trapping plates at random positions, random energies, and random directions. For collisions between ions and helium atoms, only elastic collisions were taken into account. Two out-of-phase frequency-sweeping ejection signals were applied, one to each plate, with a DC offset voltage to eject ions out of the trap. The conditions in the simulation were close to those in the real experiment, except no neutral sample molecules were added. In the simulation, space charge effects were not considered. The simulation was terminated when all ions hit the trapping plates, the boundary walls, or the detector.

From the simulated mass spectrum in Figure 4.3C, peaks at *m*/*z* 63 and 65 are well resolved (0.55 Da FWHM for *m*/*z* 63). Much worse resolution (1.9 Da FWHM) was obtained for *m*/*z* 91/92, which matched the results from the experiments as shown in Figures 4.3B, 4.4C and 4.5. Since the depth of the pseudopotential well is dependent on the *m*/*z* value, higher mass ions are trapped in shallower wells and may be more easily ejected from oscillations stimulated by the scanning ejection frequency, even though their matched secular frequencies have not yet been reached.[28] Therefore, there essentially exists a wider range of ejection frequencies to give trapped ions of specific *m*/*z* values energy and move them out of the trap, especially for higher *m*/*z* values, which broadens the time interval for ejecting ions and, hence, lowers the mass resolution. This may possibly be a result of using lower operating voltages in miniaturized ITs, since lower trapping amplitude gives a shallower pseudopotential well. This will need to be addressed if the operating power is reduced for portable analysis. Moreover, the ejection frequency was scanned linearly, but the relationship between *m*/*z* value and its secular frequency is not linear. Higher mass analysis requires more scan frequency points per unit time to obtain the same sampling per mass unit as lower mass analysis. This was demonstrated with a slower frequency scan used for higher mass analysis, and better resolution was obtained.

During experiments with 5% octopole field contribution, an unexpected phenomenon was observed. With an increase in RF potential, mass spectral peaks with *m*/*z* values greater than 70 Da moved further into the low mass direction (leftwards) as expected, while peaks with *m*/*z* values less than 70 Da moved further into the high mass direction (rightwards), as shown in Figure 4.6. The degree of movement was less for peaks with *m*/*z* values lower than 70 Da. This behavior was consistent regardless of test analyte or RF generator, and only occurred in a 5% octopole field with resonant frequency scan ejection from high to low frequency in the dipole

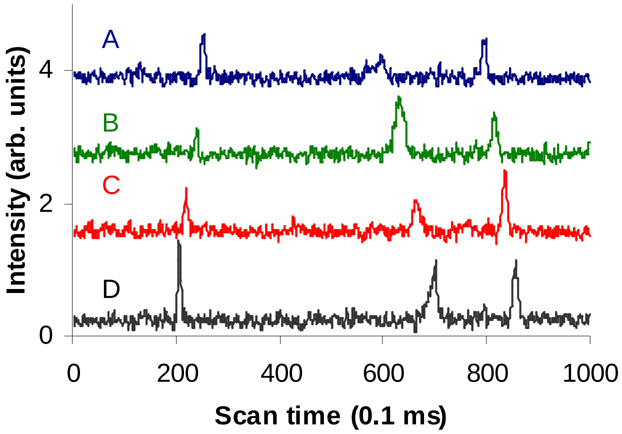

Figure 4.6. Heptane mass spectra showing the effects of (A) 423 $V_{p\text{-}p}$*, (B) 402* $V_{p\text{-}p}$*, (C) 381* $V_{p\text{-}p}$*, and (D) 360* $V_{p\text{-}p}$ *RF amplitudes on peak positions for 5% octopole field contribution; 2.0 ×* 10^{-5} *mbar sample pressure, 1.9 ×* 10^{-4} *mbar helium pressure, 1.2 MHz RF frequency, ejection AC frequency scanned from 600 to 100 kHz in 100 ms, 1.1* $V_{p\text{-}p}$ *amplitude with -0.4 V DC offset, dipole ejection.*

ejection mode with DC offset. While we do not completely understand this phenomenon, it may be related to the non-linear electric field present in the toroidal geometry. When the secular frequency of the trapped ions was scanned, the ions increased their oscillation amplitude by picking up energy from the ejection signal. Simultaneously, with the oscillation amplitude increase, their frequency shifted to higher values because of the positive octopole field. The ions were then out of resonance and the increase in oscillation amplitude stopped. However, when they went back to the center, their oscillation amplitudes increased again until they picked up enough energy from the ejection signal to be ejected. In this ejection process, the ions are delayed in leaving the trap, and they shift to the high mass direction (rightwards). With an increase in RF potential, the pseudopotential well which holds the trapped ions get deeper. Ions take more time to eject, and they shift more to the high mass direction (rightwards). Since lower mass ions have deeper pseudopotential wells than higher mass ions, the phenomenon is more apparent for them compared to the higher mass ions. This effect on lower mass is larger than the effect of changing of q_z values by increasing the RF potential, which results in mass peaks moving in the low mass direction (leftwards). Therefore, the compromised movement of low-mass ions is towards the high mass direction (rightwards) with low speed. The movement of low-mass peaks with increase in RF amplitude is not a chemical mass shift,[23] since it is not compound dependent.

4.5 Conclusions

The performance of the halo IT mass spectrometer was improved by axial ejection of ions from the trapping region through slits machined in the ceramic plates. The resolution was improved by a factor of 2.3. The resolution and abundance of the mass spectral peaks were greatly affected by percentages of high-order components of the electric field. The best resolution (280 $m/\Delta m$ for m/z 51 Da) was obtained using an electric field with 5% octopole component. It was found important to consider higher order components in the trapping field to optimize the performance of the halo IT. The overall trapping field shape and multipole composition can be changed by applying different potentials to the electrode rings. This is accomplished by soldering the appropriate capacitor network onto the PCB without having to change the ceramic plates and the structure of the halo IT. This design should allow straightforward evaluation of the effects of multipole fields other than quadrupole and octopole on ion trapping and the effects of all multipole components on resonant ejection[29,30] to further enhance the performance of the halo IT. Improvements in mass resolution may also be possible with higher frequency or higher amplitude RF, or with optimization of other trapping parameters.

4.6 References

1. March, R. E.; Todd, J. F. J. *Quadrupole Ion Trap Mass Spectrometry*, 2nd ed.; John Wiley & Sons, Inc.: Hoboken, NJ, 2005.
2. Spann, J. F.; Abbas, M. M.; Venturini, C. C.; Comfort, R. H. *Physica Scripta.* 2001, *T89*, 147–153.

3. Palmer, P. T.; Limero, T. F. *J. Am. Soc. Mass Spectrom.* 2001, *12*, 656–675.
4. Contreras, J. A.; Murray, J. A.; Tolley, S. E.; Oliphant, J. L.; Tolley, H. D.; Lammert, S. A.; Lee, E. D.; Later, D. W.; Lee, M. L. *J. Am. Soc. Mass Spectrom.* 2008, *19*, 1425–1434.
5. Blay, P. K. S.; Brombacher, S.; Volmer, D. A. *Rapid Commun. Mass Spectrom.* 2003, *17*, 2153–2159.
6. You, J.; Wang, D. L.; Lydy, M. J. *Talanta* 2010, *81*, 136–141.
7. Dulaurent, S.; Moesch, C.; Marquet, P.; Gaulier, J. M.; Lachatre, G. *Anal. Bioanal. Chem.* 2010, *396*, 2235–2249.
8. Gros, M.; Petrović, M.; Barceló, D. *Anal. Chem.* 2009, *81*, 898–912.
9. Madureira, T. V.; Barreiro, J. C.; Rocha, M. J.; Cass, Q. B.; Tiritan, M. E. *J. Chromatogr. A* 2009, *1216*, 7033–7042.
10. Badman, E. R.; Cooks, R. G. *J. Mass Spectrom.* 2000, *35*, 659-671.
11. Paul, W.; Steinwedel, H. *Z. Naturforsch.* 1953, *8A*, 448-450.
12. Fulford, J. E.; Hoa, D. N.; Hughes, R. J. March, R. E.; Bonner, R. F.; Wong, G. J. *J. Vac. Sci. Technol.* 1980, *17*, 829-835.
13. Campbell, J. M.; Collings, B. A.; Douglas, D. J. *Rapid Commun. Mass Spectrom.* 1998, *12*, 1463-1474.
14. Schwartz, J. C.; Senko, M. W.; Syka, J. E. P. *J. Am. Soc. Mass Spectrom.* 2002, *13*, 659-669.
15. Prestage, J. D.; Dick, G. J.; Maleki, L. *J. Appl. Phys.* 1989, *66*, 1013-1017.
16. Douglas, D. J.; Frank, A. J.; Mao, D. *Mass Spectrom. Rev.* 2005, *24*, 1-29.
17. Ouyang, Z.; Wu, G.; Song, Y.; Li, H.; Plass, W. R.; Cooks, R. G. *Anal. Chem.* 2004, *76*, 4595-4605.
18. Gao, L.; Song, Q.; Patterson, G. E.; Cooks, R. G.; Ouyang, Z. *Anal. Chem.* 2006, *78*, 5994-6002.
19. Lammert, S. A.; Plass, W. R.; Thompsom, C. V.; Wise, M. B. *Int. J. Mass Spectrom.* 2001, *212*, 25-40.
20. Lammert, S. A.; Rockwood, A. A.; Wang, M.; Lee, M. L.; Lee, E. D.; Tolley, S. E.; Oliphant, J. R.; Jones, J. L.; Waite, R. W. *J. Am. Soc. Mass Spectrom.* 2006, *17*, 916-922.
21. Austin, D. E.; Wang, M.; Tolley, S. E.; Maas, J. D.; Hawkins, A. R.; Rockwood, A. L.; Tolley, H. D.; Lee, E. D.; Lee, M. L. *Anal. Chem.* 2007, *79*, 2927-2932.
22. Zhang, Z.; Peng, Y.; Hansen, B. J.; Miller, I. W.; Wang, M.; Lee, M. L.; Hawkins, A. R.; Austin, D. E. *Anal. Chem.* 2009, *81*, 5241-5248.
23. March, R. E.; Todd, J. F. J. *Practical Aspects of Ion Trap Mass Spectrometry*, Vol. I; CRC Press: Boca Raton, FL, 1995; Chap. 3.
24. Wu, G.; Cooks, R. G.; Ouyang, Z. *Int. J. Mass Spectrom.* 2005, *241*, 119-132.
25. Szilagyi, M. *Electron and Ion Optics*, Plenum Press: New York, NY, 1988; p. 62.
26. Austin, D. E.; Hansen, B. J.; Peng, Y.; Zhang, Z. *Int. J. Mass Spectrom.* 2010, *295*, 153–158.
27. Field, F. H.; Hamlet, P.; Libby, W. F. *J. Am. Chem. Soc.* **1967**, *89*, 6035-6038.
28. Julian, R. K.; Nappi, M.; Weil, C.; Cooks, R. G. *J. Am. Soc. Mass Spectrom.* 1995, *6*, 57-70.
29. Kaiser, R. E.; Cooks, R. G.; Stafford, G. C.; Syka, J. E. P.; Hemberger, P. H. *Int. J. Mass Spectrom. Ion Processes* 1991, *106*, 79-115.
30. Traldi, P.; Curcuruto, O.; Bortolini, O. *Rapid Commun. Mass Spectrom.* 1992, *6*, 410-412.

CHAPTER 5. SIMULATIONS OF TOROIDAL AND HALO ION TRAPS USING SIMION

5.1 Introduction

With the evolution of the IT mass spectrometer into a powerful tool for both research and routine analysis, there has been significant interest in understanding and characterizing trajectories of trapped ions in an IT through calculations or simulation software. Simulation of ion trajectories in an IT permits visual measurement of ion motion from ionization, trapping and cooling by the applied drive potential, and producing unstable ion trajectories and ejecting ions out of the IT according to *m*/*z* by ramping the amplitude of the RF potential or scanning the frequency of the ejection signal.[1] In tandem MS, more sophisticated techniques were developed to simulate the isolation and ejection of ions with a particular *m*/*z*. Simulation of the ion trajectories in a newly-designed IT can be used to predict the performance of the new IT, which would be very helpful in the development of the IT.

The earliest calculations of ion trajectories in a QIT were reported over 40 years ago involving resonance free and collision free motion for single-mass ions, and predictions were obtained from calculations for ion trajectories, resolution, sensitivity, storage, and peak shapes.[2] A few years later, improved trajectory calculations of ions qualitatively explained the complex process of ions pulsing out of the quadrupole trap.[3] By integration of the Mathieu equation

$$\frac{d^2u}{d\xi^2}+\left(a_u-2q_u\cos 2\xi\right)u=0 \tag{5.1}$$

the ion trajectory properties in time and space can be calculated. In the equation, u is the displacement in a trap; ξ is a dimensionless parameter equal to $\Omega t/2$ where Ω is a frequency and t is time; and a_u and q_u are Mathieu stability parameters as in Eqs. 1.1 to 1.3. This integration method was limited to calculations for only one ion, and required time-consuming calculations. With the application of higher order Runge-Kutta algorithms and high performance computers, the run time for simulations was reduced while still maintaining an acceptable accuracy. Subsequently, simulation software packages added the capability of simultaneously calculating ion trajectories under the influence of auxiliary AC and/or DC potentials, collisions with buffer gas of variable pressures, space charge interactions, and higher order electric fields.[4]

The simplest simulation in an IT is calculating the trajectory of a single ion in an ideal quadrupole field without buffer gas. This can be done at any point with different a_z, q_z coordinates within or beyond the Mathieu stability diagram to show the secular frequency of the single ion or how it is lost by hitting the electrodes of the trap. The effects of ion/neutral collisions were simulated using the discontinuous collision model in order to calculate the collision probability for the pressure of the buffer gas.[5] After collision, it was assumed that the kinetic energy of ions would decrease without changing their directions,[6] leading to ion focusing to the center of the IT. Thereafter, resonant excitation and resonant ejection of ions can also be simulated by adding supplementary voltages to the electrodes. The investigation of spatial and energy distributions can be simulated by simultaneous calculation of the trajectories of more than 600,000 ions. A wide range of *m*/*z* ratios can be accommodated to permit simulation of mass spectra and ion kinetic energy distributions, and evaluation of space-charge effects. Ion trajectories from the ion source through the IT to the detector can now be simulated together with the processes of charge exchange, ionization, cluster ion formation and ion fragmentation.[7]

Three computer programs, SIMION[8,9] ITSIM[10] and ISIS[4], have been extensively used for the simulation of ion trajectories. In contrast to ITSIM and ISIS, which are adept at providing detailed information for ITs, SIMION is more versatile and allows the simulation of ion trajectories in virtually any electrostatic or magnetic field of hybrid instruments or of custom-designed assemblies of electrodes. It has been used to simulate a number of different mass spectrometers, including QITs,[8] QMFs,[9] digital ITs,[12] time of flight,[11] and ion cyclotron resonance,[13] as well as ion mobility spectrometers.[14] Ion behaviors in new IT designs were simulated by SIMION to examine their performance. In an array of micrometer-sized CITs,[15] simulations were performed on the effects of temperature on ion and neutral species, pressure of cooling gas, ion mass, trapping voltage and frequency, space charge, and fabrication defects. In the new concept of gap-tripole IT,[16] which is a mix of a linear and a 3D trap, simulations showed axially-focused performance, high ejection efficiency, and high duty cycle. Moreover, SIMION has been extremely powerful for modeling electron or ion optics in an ion source where externally created ions were guided such as in ESI,[17] matrix-assisted laser desorption/ionization (MALDI),[18] or glow discharge (GD)[19] instrumentation, or where high-energy electrons were concentrated for *in situ* ionization such as in Einzel lenses[20] or complex ion funnels.[21] The efficiency of injecting and trapping ions from an external ion source in a QIT was measured and simulated using a simple hard-sphere collision model.[22,23] Thus, SIMION can directly model charged particle trajectories through custom-designed electrodes as in new-concept ITs or ion sources, and can take into account truncation and holes in electrodes, and additional higher order electric fields due to IT geometric modification.

To understand the ion trapping and ejection trajectories in the toroidal IT and halo IT, computer simulations with SIMION 7.0 and 8.0 have been performed in this work. Focus was on the trapping field, ion collisional cooling and trapping in the field, and ion excitation and ejection. Higher order fields were calculated in the trapping field, and electric gradient contours were researched for trapping ions. Ions were collisionally cooled in a toroidal shape to demonstrate trapping in the toroidal and halo ITs. Mass spectra were also simulated from random creation of ions in trapping areas, collisional cooling with buffer gas, trapping by RF drive potential, resonant excitation and ejection by auxiliary AC voltage, detection and compiling the simulated data.

5.2 Computational Method

Simulations of toroidal IT and halo IT performance were carried out using SIMION 7.0 and 8.0 software (Idaho National Engineering Laboratory, Idaho Falls, ID). All electrodes in both the toroidal and halo ITs were defined in SIMION using a half-million-point potential array (PA) with nonsymmetrical *x* dimension and symmetrical *y* and *z* geometry. Every grid unit was set as 10 μm for all simulated traps. In the toroidal IT, PAs were drawn according to the metal electrodes with ideal machining and perfect alignment. In the halo IT, since the semi-conductive germanium layer is neither an electrode nor non-electrode, there were two approaches to simulate the electrode rings and the germanium layer. In the first approach, ring electrodes were simulated as PAs according to their dimensions, and the germanium layer was regarded as a metal electrode between each pair of rings with the average potential of the two adjacent electrode rings. In the other approach, bars according to the dimensions of the electrode rings were drawn all the way across the PA, and corresponding potentials were set. The electrodes in this PA file consisted of a series of concentric cylinders. Then the “find” function was used to highlight all points with potentials lower than the maximum ring voltage, and all non-electrode points between the bar electrodes were changed to electrodes with the same potentials, which were regarded as the germanium layer. Excess electrode points were changed to non-electrodes and the thickness of the ring electrodes and germanium layer were kept at 1 mm (100 grid units), and a center hole or slits for ion ejection and metal spacers were added in the PA file. For this approach, the potentials on the germanium layer between the electrode rings were set at identical values as the potentials between the corresponding concentric cylinder electrodes.

In the concentric cylinder system, the voltages of the adjacent cylinders can be expressed as[24]

$$V_2 - V_1 = \frac{\lambda}{2\pi\varepsilon_0} \ln \frac{r_2}{r_1} \tag{5.2}$$

where V_2 and V_1 are the voltages of the adjacent cylinder electrodes, λ is the charge per unit length of the cylinder, ε_0 is the permittivity of free space between the adjacent cylinders, and r_2 and r_1 are the radii of the adjacent cylinders. Since the charge is uniformly distributed on the electrodes, Eq. 5.2 can be used to express the relationships between the potential of any point in the system V and the voltages of the cylinder electrodes

$$\frac{2\pi\varepsilon_0 (V_2 - V)}{\ln \frac{r_2}{r}} = \frac{2\pi\varepsilon_0 (V - V_1)}{\ln \frac{r}{r_1}} \tag{5.3}$$

Therefore, the potential of any point between the cylinder electrodes V is

$$V = \frac{V_1 \ln \frac{r_2}{r} + V_2 \ln \frac{r}{r_1}}{\ln \frac{r_2}{r_1}} \tag{5.4}$$

where r is the distance between the point and axis of the concentric cylinder electrodes.

In the germanium layer between two adjacent electrode rings, the resistance of the germanium R can be written as

$$R = \rho \frac{l}{A} \tag{5.5}$$

where ρ is the resistivity of germanium, l is the length of the piece of germanium, and A is the cross-sectional area of the germanium.

Therefore, the resistance of any tiny germanium ring of radius r between two electrode rings with voltages of V_1 and V_2 is

$$R = \rho \frac{dr}{2\pi ra} \tag{5.6}$$

where a is the thickness of the germanium layer.

Eq. 5.6 can be integrated to obtain the resistance of the germanium between any two adjacent electrode rings with radii of r_1 and r_2.

$$R = \frac{\rho}{2\pi a} \ln \frac{r_1}{r_2} \tag{5.7}$$

Therefore, the relationships between the voltage V at any point on the germanium with radius r and the voltages of the electrode rings are expressed as

$$\frac{V_2 - V}{\frac{\rho}{2\pi a} \ln \frac{r_2}{r}} = \frac{V - V_1}{\frac{\rho}{2\pi a} \ln \frac{r}{r_1}} \tag{5.8}$$

From Eq. 5.8, the voltage V at any point on the germanium can be expressed as

$$V = \frac{V_1 \ln \frac{r_2}{r} + V_2 \ln \frac{r}{r_1}}{\ln \frac{r_2}{r_1}} \tag{5.9}$$

The identities of Eqs. 5.4 and 5.9 proves the second approach to simulate the germanium layer.

Then the PAs were refined to a convergence limit of 10^{-7}, the lowest limit possible in SIMION. A user-written program using SIMION language provided the initial ion parameters in the traps, collisions with buffer gas, time-varying electrical potentials at the electrodes, and other control functions. These programs are included in the Appendix.

In the simulations, ionization took place *in situ* and the initial positions of ions were randomly distributed in x, y, and z directions within a cylinder in the trap. Initial ion velocities and directions were randomized to a Maxwell distribution. Ion time-of-birth was randomized within the ionization period. Ions collided with buffer gas and were trapped in a circular band with low energies in the center of the trapping region in a-few-second cooling time. In order to speed up the simulations, in a simple version of the program, the random initial positions of ions were restricted within a spherical volume with 0.1-mm radius to decrease the cooling time, and the initial ion velocities and directions were randomly set in small ranges to simplify the calculations.

The simulations involved a helium collisional buffer gas, and each helium molecule was defined to have a random position and resting state at the moment of impact with an ion. In all simulations, both ions and buffer gas molecules stayed at the same temperature. The collisional probability is related to the mean free path, which is determined by the temperature and pressure. The collisions between ions and buffer gas molecules were assumed to be elastic collisions. Whether or not a collision happened was determined by comparing a random number between 0 and 1 to the probability of collision in each time step. Scattering angle and velocity for each ion collision were determined using momentum and energy conservation calculations in the *x*, *y*, and *z* dimensions. In the simple program version, the mean free path was defined at 300 K and 1 mTorr pressure to avoid extra calculations.

In all simulations, space charge effects were not considered due to the large trapping capacity a toroidal geometry can provide to avoid ion-ion repulsion issues. Simulations were terminated when all ions hit the trapping plates, the boundary walls, or the detector. In the simple program version, another restriction that all remaining ions died when the mass scan was over was added to terminate the program to minimize the simulation time.

The SIMION program can be used to calculate and determine the coefficients for higher order multipole electric fields in the trapping fields of ITs.[25] SIMION 8.0 and MATLAB R2008b programs were used to calculate the A_2, A_4 and A_6 dimensionless multipole coefficients. According to the superposition principle in electric field theory, the coefficients for each order (i.e., quadrupole, octopole and dodecapole in equation 10) for all rings in the halo IT can be summed to provide the overall multipole field component to the total electric field. Initially, a file describing the geometry of the halo IT was created in SIMION. Then, a voltage of 1000.0001 V was sequentially added to each ring electrode while keeping the voltage on the remaining electrodes at 0 V. For each applied voltage change, the simulated potential and its corresponding z value were recorded for every grid unit (i.e., at equal time steps) along the z direction. With the data obtained, MATLAB was used to determine the multipole field components for each ring at a desired degree of accuracy (i.e., A_{2l}, A_{4l} and A_{6l} for the l^{th} ring electrode where $l = 1$ to 11) in the z direction as specified in equation 10 (a polynomial with up to 20 poles) with their corresponding least-squares fits.

After the multipole coefficients for each ring were determined as described in the previous paragraph, arbitrary voltages were assigned to the various ring electrodes, and the resultant multipole components of the total electric field in the halo IT were calculated by multiplying the voltages applied to each ring by the various multipole coefficients and summing the products of each multipole type. The various summed higher-order multipole percentages were obtained by dividing each summed higher-order multipole coefficient by the summed quadrupole coefficient, and then multiplying by 100% (i.e., A_4/A_2 for octopole, and A_6/A_2 for dodecapole). Finally, the SOLVER function in Microsoft Office Excel was used to specify new

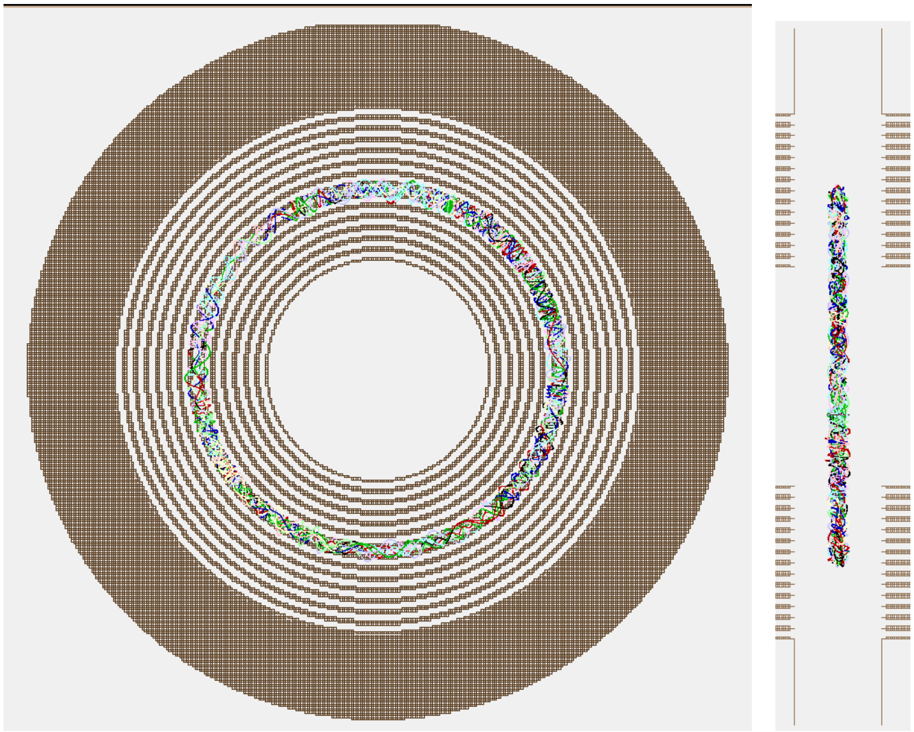

Figure 5.1. SIMION simulation showing the trajectories of trapped ions that have been collisionally cooled into a circular band by 1 mtorr helium.

voltages to apply to the ring electrodes in order to adjust the multipole percentages to the desired values.

5.3 Results and Discussion

5.3.1 Reliability of simulation

The SIMION software package was primarily used to calculate the electric fields generated when a configuration of electrodes and their voltages are specified. It was also used to calculate the trajectories of charged particles in these fields when the initial conditions for these particles are given. For an application, SIMION can define the system geometry and conditions, record and visualize results, and extend the simulation capabilities by user programming.

By using SIMION simulation, a visualized result was fitted to the theory prediction. For example, in the halo IT with radial ejection, the voltage on each ring was calculated using

SOLVER in the Excel software to produce a quadrupole electric field between the two trapping plates. Ions were expected to be trapped at a radius equal to that of the 8th electrode ring, corresponding to the toroidal trapping well. As shown in Figure 5.1, trapped ions collisionally cooled into a circular band between the two plates at the 8th electrode ring.

The SIMION simulated mass spectra matched the results from real experiments. The mass spectrum of toluene produced by SIMION (Figure 4.3) closely matches the spectrum from experiment under the same operating parameters, such as RF frequency and amplitude, ejection frequency and DC offset with dipole ejection. In the simulation, ions with an *m*/*z* value of 105 were not generated, and fewer ions were retained in the trap than in the real experiment. Therefore, the mass spectrum simulated by SIMION had better resolution, especially in the higher-mass region, and did not show a peak at *m*/*z* value of 105.

In SIMION simulations, the behaviors of ions as a result of changing one or more of the operating parameters agreed with the results produced from experiments. For instance, in experiments in which the resonant ejection frequency was scanned from high to low, if the RF amplitude was increased, every trapped ion was ejected sooner. In the simulations, several programs with different RF amplitudes were run and the resultant mass spectra were compared. Higher RF amplitude also gave earlier ejected mass peaks.

On the other hand, if SIMION simulations were not conducted correctly or according to experimental parameters, they produced results that were not consistent with experiments. Before figuring out how to simulate the germanium layer in SIMION, the electrode rings were set in the geometry files without correctly considering the germanium layer. The resultant simulations showed the expected trapping of ions in a toroidal shape, but ion ejection did not match the mass spectra obtained from experiments. The germanium layer is used to minimize edge effects of the electrode rings when ions were close to the plates in the halo IT. When ions were driven by resonant frequency and expanded their trajectories from the trapping center close to the plate, edge effects from the electrode rings greatly influenced the trajectories of resonant ions if the germanium layer was absent. Therefore, ions would not behave correctly according to the real experiments, and the simulations produced unexpected results. During other simulations, if some parameters, such as the potential on one electrode ring, or ejection amplitude, were improperly selected in SIMION, ions could not be trapped or ejected, and no simulated mass spectra were generated.

Overall, SIMION simulation produced the expected results according to theory and experiments in this work. Therefore, the SIMION modeling was considered reliable to be used in this work to predict and confirm experiments.

5.3.2 Simulations of the toroidal IT

The geometry, electric field profiles and mass analysis performances of a toroidal IT[26,27] were simulated in the SIMION program. Figure 5.2 shows the geometric images of the toroidal IT in full (A) and cut in half along the center axis (B). The electrodes were designed in simulations to produce a structure that approximated the shape and dimensions of a real toroidal IT with ideal machining techniques. The detector in Figure 5.2A was simplified to be a flat plate with – 1.7 kV applied as in real experiments.

Figure 5.3 shows the electric field with isopotential contours in the toroidal IT. From the figure, a quadrupole trapping field is shown to be formed in the toroidal IT, and the trapping center is not on the axis which connects the ejection slits. The vertices of the isopotential contours do not form a straight line, shown as green points in the inserted figure. When ions resonate with the ejection frequency and become excited and move from the trapping center to

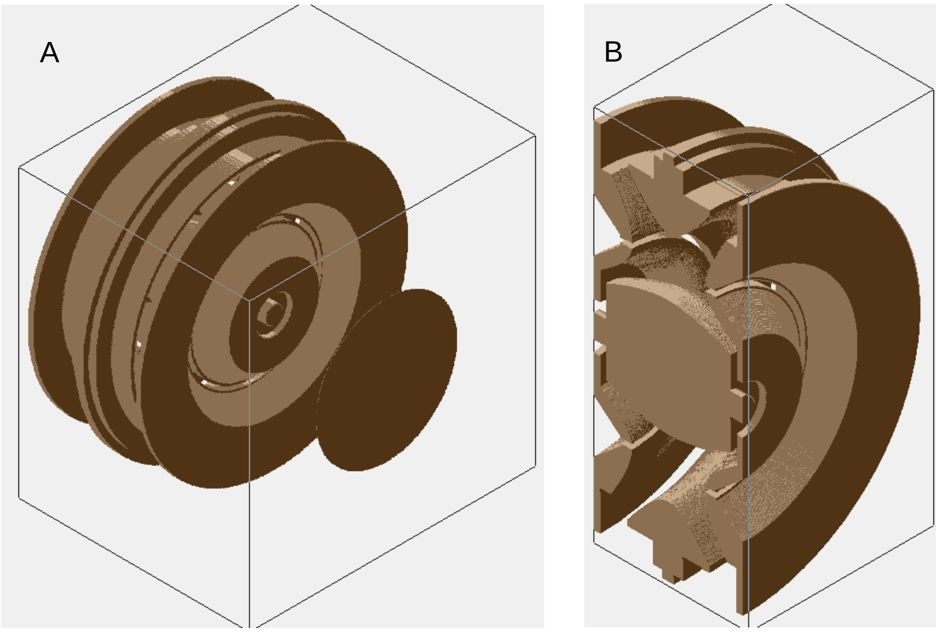

Figure 5.2. Images of the toroidal IT (A) in full with a detector and (B) cut in half along its center axis for simulations.

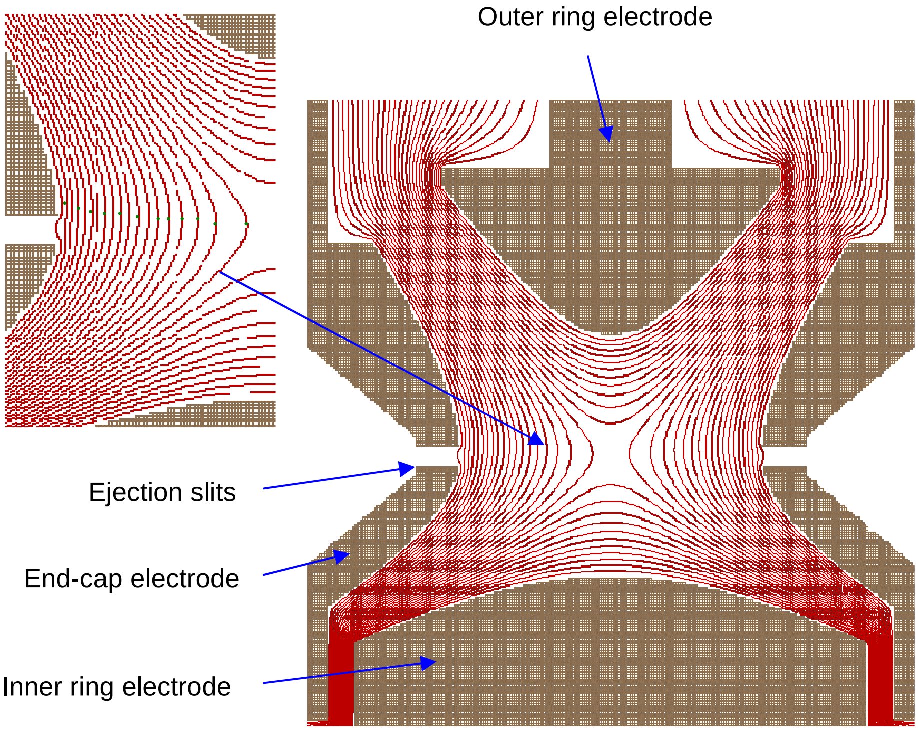

Figure 5.3. Isopotential contours in the toroidal IT showing the trapping electric field.

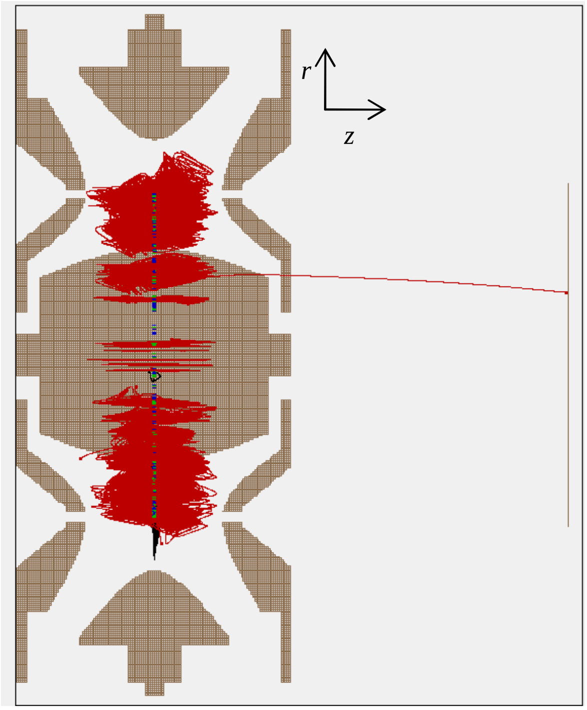

Figure 5.4. Simulation of ion trapping, excitation and ejection in the toroidal IT.

the slits, their ejection trajectories expand along the lowest potential points (the vertices of the isopotential contours) until they pass through the slits. Since the vertices for the isopotential contours do not line up with the slits, the excitation directions of ions are divided into the *z* and *r* directions. The excitation of ions in the *r* direction will lead to poor resolution; therefore, a small amount of DC offset must be added to the electrodes (either end-cap or ring electrodes) to modify the β_r value to minimize the excitation of ions in the *r* direction.

The SIMION program can also simulate trapping, excitation and ejection of ions in the toroidal IT, as shown in Figure 5.4. The green and blue ions remained tightly trapped at the center of the toroidal geometry, while the secular frequency of the red ions (different colors of ions represent different *m*/*z*) was coupled resonantly with the supplementary ejection AC in the *z* direction. Since a DC voltage offset was added, no apparent excitation of ions in the *r* direction

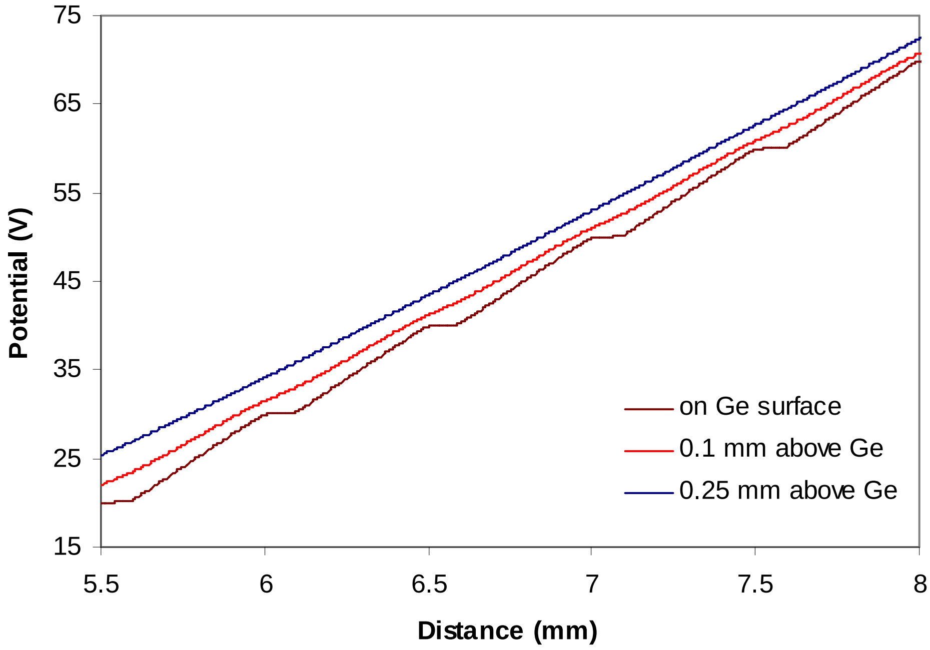

Figure 5.5. Potentials along the germanium surface, 0.1 mm and 0.25 mm above the germanium layer within the trap.

was observed. When the red ions obtain enough energy from the resonant ejection frequency, their unstable excursions in the quadrupole trapping volume eventually take them beyond the physical boundary of the device. Ions were ejected from the device through the slits in the end-cap electrodes toward the detector, as shown by the red trajectory out of the trap to the detector in Figure 5.4.

5.3.3 Simulations of the halo IT with radial ejection

The novelty of the halo IT[28] is that the trapping electric field is defined by desired surfaces with position-varying potentials rather than the shapes of the metal electrodes in traditional ITs. A surface with different potential functions on it can be realized using resistive materials, such as germanium. To create a desired electric field which can be controlled and optimized, it is necessary to superimpose the electric fields produced by arbitrary potential functions on the resistive materials. In the halo IT, concentric electrode rings were fabricated on a ceramic plate beneath a layer of germanium using photolithographic techniques. The voltage on each electrode ring was independently controlled by a capacitor network. The germanium layer on the electrode rings established a continuous boundary condition with defined voltages to create the trapping field. Figure 5.5 shows how the germanium layer smoothed the electric field in the halo trap. The voltage steps clearly evident directly on the germanium layer with increase in the distance from the center of the ceramic plate were much lessened at 0.1 mm above the germanium layer. The voltages at 0.25 mm above the germanium layer were continuous and smooth. Therefore, the germanium layer minimized edge effects in the halo IT. Another function of the germanium layer was to prevent charge build-up, which could interfere with the fields in the trap.

Simulations showed how ions were created, collided with helium molecules, and decreased their excursion ranges in the trap. During the process, the coupling of ion secular frequency and applied RF potential could be visually measured as small ripples. Trapped ions in the halo IT were collisionally cooled into a circular band, which is demonstrated by the SIMION simulation shown in Figure 5.1. Ions in a standard-size (r_0 = 1 cm) QIT or CIT are cooled to a ball with radius of roughly 0.5 mm at the center of the trap,[29] resulting in an effective trapping volume of roughly 0.5 mm^3. In contrast, ions in the halo IT are cooled to a ring between the plates. Assuming similar voltage gradients and 8-mm-radius trapped ion ring, the trapping volume is increased to roughly 40 mm^3. For a given density of ions and a given level of mass resolution, the halo IT can contain ~ 80 times as many ions as a conventional trap, which should result in greater sensitivity.

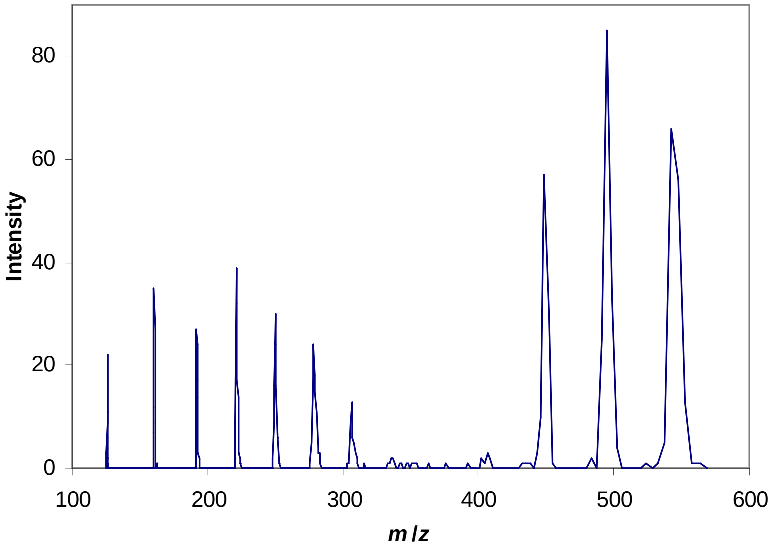

Figure 5.6. SIMION simulated mass spectrum showing good resolution in the low mass region and poor resolution in the high mass region.

Mass spectra simulated using SIMION in the halo IT with radial ejection indicated that good mass resolution could be obtained in the low mass region; in contrast, poor mass resolution occurred in the high mass region, as shown in Figure 5.6. In this simulation, ions in the range of *m*/*z* from 100 to 650 were generated between the two trapping plates at random positions, random energies, and random directions in a cylindrical volume. Resonant frequency scan ejection was used in this simulation, which was terminated when all ions hit the trapping plates, the boundary walls, or the detector. The simulated mass spectrum showed poor mass resolution at *m*/*z* higher than 250. The reason is due to edge effects that cause the field to drop off significantly near the center hole when ions are ejected out of the device along the radial axis, producing field distortions even though the trapping fields in the vicinity of the center of the trapping region agreed well with the toroidal IT. Moreover, simulations also showed that bending of the ion trajectories when they were ejected from the trap and passed through the central hole resulted in most of them hitting the plate, thereby producing poor sensitivity.

5.3.4 Simulations of the halo IT with axial ejection

In the halo IT, the effect on the trapping electric field by changing the distance between the two electrode plates is not the same as in conventional ITs, and the separation of the plates does not directly modify the higher order multipole contributions to the field. In ITs with metal electrodes, the distance between the electrodes plays an important role in the contribution of higher order multipoles in the trapping electric field. A positive octopole component was generated by stretching the end-cap electrodes to compensate for the negative octopole contribution caused by electrode truncation and perforations for electrons/ions entrance/exit, therefore improving ion ejection efficiency and mass resolution. In the halo IT with planar resistive electrodes,[28,30] the higher order multipole contributions are manipulated by modifying the potential function on the resistive electrodes instead of varying the plate spacing.[31]

Four trapping electric fields with different percentages of octopole components in the halo IT were designed by modifying the potential functions on the electrode rings on the plates. As shown in Figure 5.7, halo IT electric fields with 1, 3, 5 and 7% octopole and constant -50% dodecapole contributions were plotted with their resultant isopotential contours, and the higher order components in the axial direction along the axis connecting the centers of the slits were drawn for each trap. From the figure, the centers of the electric fields for the traps look similar; however, small differences are observed in the region near the trapping plates, which correspond to different higher order field components. Figure 5.7E also shows that the differences in higher order contributions mainly occur in the regions away from the centers of the electric fields ($z > 0.2$). Therefore, during ion trap operation, higher order components have little effect on ions when they are collisionally cooled to the trap center, but play an important role in ion trapping efficiency and ejection when their trajectories are near the trapping plates. These simulations

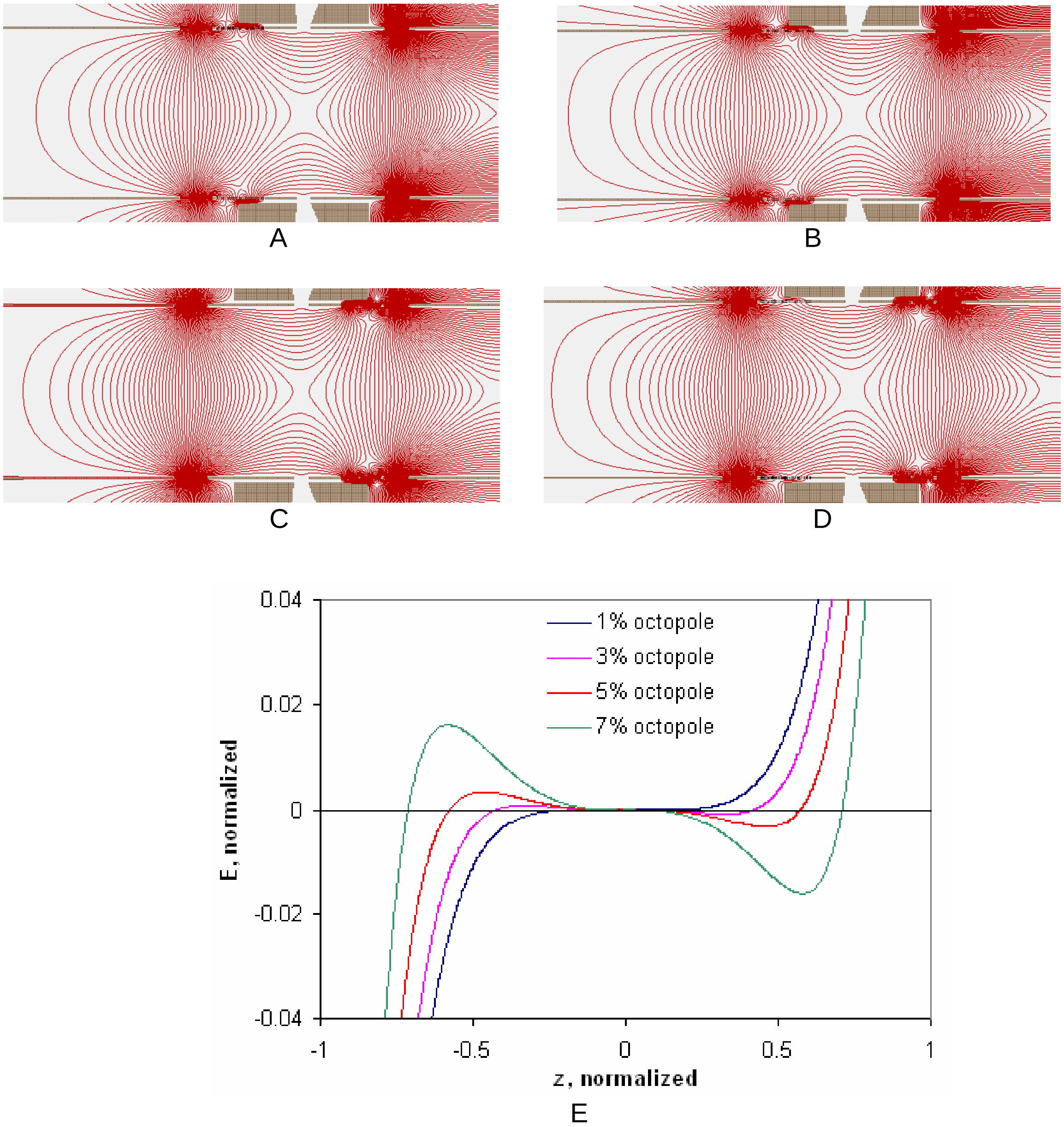

Figure 5.7. Isopotential contours for halo ITs with (A) 1% octopole, (B) 3% octopole, (C) 5% octopole, and (D) 7% octopole; and (E) higher order multipole contributions, excluding the quadrupole field component, in the axial direction for each of the above traps.

illustrate a possible way to optimize the performance of the halo IT by varying the higher order components independently.

5.4 Conclusions

SIMION simulation programs have been employed for studying and developing the toroidal and halo ITs. They allow simulations of IT electrodes and electric field profiles with arbitrary geometries, permit visual measurement of ion motions with various applied RF potentials and ejection parameters, and help to understand how the traps perform mass analysis. SIMION simulations for the toroidal and halo ITs elucidated ion motion behaviors, predicted experimental results, and showed the effects of higher order multipole contributions to the electric fields. These applications of SIMION demonstrated that it is a powerful and helpful tool for the design and development of ITs.

5.5 References

1. Forbes, M. W.; Sharifi, M.; Croley, T. R.; Lausevic, Z.; March, R. E. *J. Mass Spectrom.* 1999, *34*, 1219–1239.
2. Dawson, P. H.; Whetten, N. R. *J. Vac. Sci. Technol.* 1968, *5*, 1–10.
3. Dawson, P. H.; Lambert, C. *Int. J. Mass Spectrom. Ion Phys.* 1974, *14*, 339–347.
4. Londry, F. A.; Alfred, R. L.; March, R. E. *J. Am. Soc. Mass Spectrom.* 1993, *4*, 687–705.
5. Reiser, H. P.; Julian, R. K.; Cooks, R. G. *Int. J. Mass Spectrom. Ion Processes*. 1992, *121*, 49–63.
6. Weil, C.; Nappi, M.; Cleven, C. D.; Wollnik, H.; Cooks, R. G. *Rapid Commun. Mass Spectrom.* 1996, *10*, 742–750.
7. March, R. E.; Todd, J. F. J. *Quadrupole Ion Trap Mass Spectrometry*, 2nd ed.; John Wiley & Sons, Inc.: Hoboken, NJ; 2005.
8. Ma, C.; Lee, H. W.; Lubman, D. M. *Appl. Spectrosc.* 1992, *46*, 1769–1779.
9. Blaum, K.; Geppert, C.; Muller, P.; Nortershauser, W.; Otten, E. W.; Schmitt, A.; Trautmann, N.; Wendt, K.; Bushaw, B.A. *Int. J. Mass Spectrom.* 1998, *181*, 67–87.
10. Bui, H. A.; Cooks, R. G. *J. Mass Spectrom.* 1998, *33*, 297–304.
11. Ding, L.; Sudakov, M.; Kumashiro, S. *Int. J. Mass Spectrom.* 2002, *221*, 117–138.
12. Veryovkin I. V.; Chen, C. Y.; Calaway, W. F.; Pellin, M. J.; Lee. T. *Nucl. Instrum. Meth. A* 2004, *519*, 345–352.
13. He, L.; Lubman, D. M. *Rapid Commun. Mass Spectrom.* 1997, *11*, 1467–1477.
14. Mariano, A. V.; Su, W.; Guharay, S. K. *Anal. Chem.* 2009, *81*, 3385–3391.
15. Austin, D. E.; Cruz, D.; Blain, M. G. *J Am. Soc. Mass Spectrom.* 2006, *17*, 430–441.
16. Salazar, G. A.; Masujima, T. *J Am. Soc. Mass Spectrom.* 2008, *19*, 1367–1374.

17. Quarmby, S. T.; Yost, R. A. *Int. J. Mass Spectrom.* 1999, *191*, 81–102.
18. Doroshenko, V. M.; Cotter, R. J. *J. Mass Spectrom.* 1997, *32*, 602–615.
19. Song, K.; Cha, H.; Park, H.; Lee, S. C. *Microchem. J.* 2001, *70*, 285–291.
20. Gard, E. E.; Green, M. K.; Warren, H.; Camara, E. J. O.; He, F.; Penn, S. G.; Lebrilla, C. B. *Int. J. Mass Spectrom. Ion Processes*. 1996, *157/158*, 115–127.
21. Shaffer, S. A.; Tang, K.; Anderson, G. A.; Prior, D. C.; Udseth, H. R.; Smith, R. D. *Rapid Commun. Mass Spectrom.* 1997, *11*, 1813–1817.
22. Appelhans, A. D.; Dahl, D. A. *Int. J. Mass Spectrom.* 2002, *216*, 269–284.
23. Wu, H.; Chen, L.; Lin, Y. *J. Chin. Chem. Soc.* 1999, *46*, 923–932.
24. Fishbane, P. M.; Gasiorowicz, S.; Thornton, S. T. *Physics for Scientists and Engineers*, ext. ver.; Prentice-Hall, Inc.: Englewood Cliffs, NJ; 1993.
25. Austin, D. E.; Hansen, B. J.; Peng, Y.; Zhang, Z. *Int. J. Mass Spectrom.* 2010, *295*, 153–158.
26. Lammert, S. A.; Plass, W. R.; Thompson, C. V.; Wise, M. B. *Int. J. Mass Spectrom.* 2001, *212*, 25–40.
27. Lammert, S. A.; Rockwood, A. A.; Wang, M.; Lee, M. L.; Lee, E. D.; Tolley, S. E.; Oliphant, J. R.; Jones, J. L.; Waite, R. W. *J. Am. Soc. Mass Spectrom.* 2006, *17*, 916–922.
28. Austin, D. E.; Wang, M.; Tolley, S. E.; Maas, J. D.; Hawkins, A. R.; Rockwood, A. L.; Tolley, H. D.; Lee, E. D.; Lee, M. L. *Anal. Chem.* 2007, *79*, 2927–2932.
29. Hemberger, P. H.; Nogar, N. S.; Williams, J. D.; Cooks, R. G.; Syka, J. E. P. *Chem. Phys. Lett.* 1992, *191*, 405-410.
30. Zhang, Z.; Peng, Y.; Hansen, B. J.; Miller, I. W.; Wang, M.; Lee, M. L.; Hawkins, A. R.; Austin, D. E. *Anal. Chem.* 2009, *81*, 5241–5248.
31. Austin, D. E.; Peng, Y.; Hansen, B. J.; Miller, I. W.; Rockwood, A. L.; Hawkins, A. R.; Tolley, S. E. *J. Am. Soc. Mass Spectrom.* 2008, *19*, 1435–1441.

CHAPTER 6. CONCLUSIONS AND FUTURE DIRECTIONS

6.1 Conclusions

Miniature, field-portable MS is being developed for on-site analysis.[1] ITMS is particularly attractive for miniaturization due to its intrinsic advantages including new and unique geometries to maintain sufficient trapping volumes. This dissertation describes the design and development of toroidal[2,3] and halo ITs,[4] both of which have a circular trapping volume rather than only a trapping center as in a conventional IT. This allows higher ion capacities, especially when the devices are miniaturized.

The toroidal IT was designed by rotating a conventional 3D IT cross-section on an edge axis instead of the center axis. It has a toroidal trapping geometry and maintains similar trapping capacity as a conventional QIT, even though its dimensions were miniaturized. Unit mass resolution and high sensitivity was obtained using this miniature device through preliminary optimization of operating parameters, such as ionization and cooling times, RF drive amplitude, ejection β value, and ejection voltage. Further miniaturization is challenging due to the machining tolerances for the electrodes. Improvements of its performance are continually being made by optimization of the trapping electric fields in the non-ejection dimensions.

The halo IT combines the advantages of a toroidal trapping geometry with photolithographic microfabrication of two parallel ceramic trapping plates. This work demonstrates a novel idea for trapping ions in an arbitrarily generated electric field. The electric field in the halo IT is produced by controlling an array of voltages applied to concentric electrode rings on two mirrored plates, rather than using curved 3D metal electrodes. With a number of electrode rings on two identical, facing ceramic plates, the shapes of, and higher order multipole contributions to the trapping electric field can be changed by controlling the potentials on the rings without physically modifying the shapes of the electrodes or stretching the traps. Moreover, the products of any trapping geometry, such as a 3D trapping volume, a toroidal band, or a linear shape, are possible using this approach.[5-7]

The plates of the halo IT were initially designed with a center hole in each plate for radial ion ejection. This trap with only two ceramic plates provided an open structure, which allowed ions or electrons to have open access to the whole trapping area, and facilitated easy pumping of the trap. Mass spectra were obtained with mass resolution up to 120 (*m*/Δ*m*, FWHM), which demonstrated toroidal trapping and mass analysis with the novel trap. Mass resolution was limited in this design, since ions ejected through the center hole were influenced by the trapping field and the high voltage on the detector.

The geometry of the halo IT was subsequently modified by machining slits in the ceramic plates for ion ejection directly from the trapping toroid instead of through the center hole. The mass resolution was improved by a factor of 2.3 by performing axial ejection using the new halo IT. Investigation of octopole contributions to the trapping fields on performance of the halo IT demonstrated the concept that the overall trapping field shape and multipole composition could be easily controlled by applying different potentials to the electrode rings. Higher order multipole components in the trapping field are important for optimization of the performance of the halo IT. This axial ejection design kept all of the advantages of the previous design, such as open access for ions or electrons, large ion storage volume, and high precision fabrication, all of which are well-suited for future miniaturization efforts.

6.2 Recommendations for Improving Performance of the Halo IT

For the halo IT, worse mass resolution was observed for high-mass peaks than for low-mass peaks. The possible reason is that higher mass ions are trapped in a shallower pseudopotential well and are more easily ejected out of the trap compared to lower mass ions. Therefore, high mass ions are subjected to excitation even though their matched secular frequencies have not yet been reached, and they are ejected with a wider range of q_z values, which results in worse mass resolution.[8] If RF power with higher amplitude could be applied to the trap, the pseudopotential well for ions would be increased enough so that only a corresponding secular frequency could give sufficient energy to push ions out of the trap. Since the RF trapping frequency must also be increased with RF amplitude to keep ions in the desired region of the stability diagram, a new RF power generator that could provide higher frequency and higher amplitude would improve mass resolution.

A resonant ejection frequency scan with constant RF amplitude is primarily used for mass analysis with the halo IT. When resonant frequencies were scanned, ions with different m/z values are ejected at different β values. Due to the existence of higher order multipole components at specific β values in the non-ideal trapping electric field, ions with different m/z values are resonantly ejected from unexpected background fields.[9,10] Some would be excited because of nonlinear resonance and lost before they become resonant and ejected from an ideal quadrupole field. Ions with the same m/z value could also exhibit two or more peaks. When ions are ejected by scanning the RF amplitude with constant ejection frequency, those with different m/z values are always ejected at the same β value with the same higher order electric field, and they should exhibit the same peak width. This would require a new RF power generator which could provide amplitude-scanning.

In the toroidal IT, when ions were ejected at low β values with scanning RF amplitude, peaks with good mass resolution were observed. Halo ITs have the same toroidal-shaped trapping field as in the toroidal IT, and resonant ejection occurring at low β values should also give improved mass resolution.

Since the halo IT is a 2D quadrupole trapping device, trapped ions have similar secular frequencies in the z and r directions.[2] During ion resonant ejection, energy associated with the ion's motion in the z direction is coupled to motion in the r direction, resulting in spreading of the ion cloud in the non-ejection direction during mass analysis, therefore, producing poor resolution. A small DC voltage offset applied to the electrodes alters the Mathieu a value in the stability equations and improves the mass resolution.[3] However, in the halo IT, the trapping electric field is created by voltages on the electrode rings instead of shaped metal electrodes in conventional ITs. RF voltage is applied to one of the rings on each plate, and ejection voltage is applied to another. A capacitor network connecting all of the rings is used to conduct the trapping and ejection voltages to all electrode rings, which generates the quadrupole trapping field and dipole ejection. In this work, a DC offset was added to the ejection signal; however, it could not pass through the capacitor network to reach the other rings. Therefore, the DC voltage was applied to only one electrode ring on each plate. It is probably insufficient to alter the Mathieu a value if a DC offset is applied to only one ring. Systematic work should be focused on the Mathieu stability diagram of the halo IT to determine how many rings should be connected to the DC voltage to alter the Mathieu a value and how to realize the DC voltage applied to multiple rings.

6.3 Recommendations for Simulations

The trapping electric field in the halo IT can be simulated using the COMSOL Multiphysics modeling and simulation program (Comsol, Stockholm, Sweden).[11] COMSOL, using finite element analysis, allows the calculation of a quasi-static solution to Laplace's equation for the electric field with the RF module. The electric field is simulated by the calculation of voltages at each vertex of a tetrahedron. The tetrahedral mesh is adaptively refined, which is proportional to the electric field gradient and can be denser around the object of interest. Therefore, COMSOL is better for electric field calculation and simulation than SIMION, although it cannot simulate trajectories of trapped ions in the ITs. COMSOL also offers an extensive interface to MATLAB, and includes port and scattering boundary conditions, and complex material models. For the halo IT, COMSOL can simulate the unique design of a layer of germanium spread on the gold electrode rings, fabricated on ceramic plates. It avoids the electrode simulation problem in SIMION which only recognizes electrodes and nonelectrodes. COMSOL is more suitable for calculation of the higher order multipole contributions to the trapping electric fields in the halo IT.

6.4 Tandem MS in the Halo IT

In order to perform tandem MS in the halo ion trap, after ionizing the sample and cooling down the ions, parent ions whose structures are of interest must be isolated.[12] A combination of RF and DC voltages can be applied to the trap to accomplish this. By changing the amplitudes of the RF and DC voltages, conditions can be established in which only ions within a narrow mass range are stable and other ions are ejected. These trapped ions have a characteristic secular frequency related to the stability parameter. A dissociation AC with a small voltage having a frequency matching the secular frequency of the parent ions could be applied. Absorption of

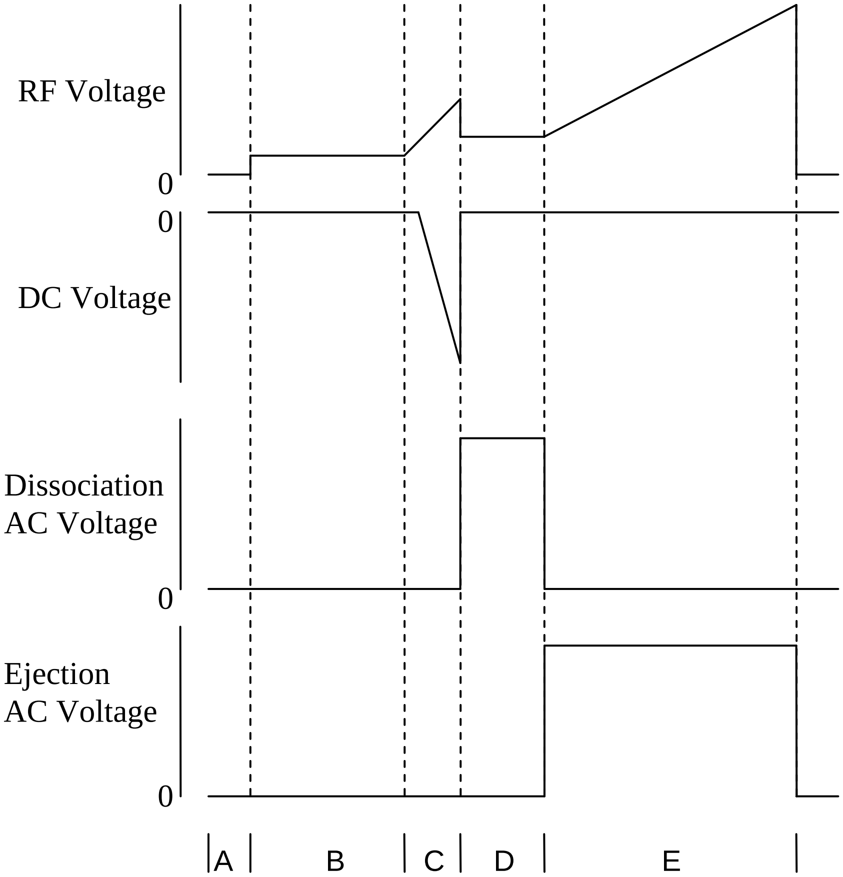

Figure 6.1. Halo IT timing sequence to perform tandem MS. Dumping non-ejected ions out of the trap in period A; ionization in period B; parent ion isolation in period C; fragment ions generated in period D; and mass analysis scan performed in period E.

energy from the dissociation AC would increase the kinetic energy of the ions and, through collisions with helium buffer gas, this kinetic energy would be converted into internal energy, which could cause dissociation of the parent ion by CID (collision-induced dissociation). Finally, the fragment ions would be analyzed by the standard mass-selective instability scan with resonance ejection AC to record the daughter MS/MS spectrum. Figure 6.1 summarizes this tandem MS experiment, showing how the combination of RF, DC, dissociation AC and ejection AC voltages could be applied to the electrodes in an appropriate sequence to record the MS/MS spectrum.

6.5 Ion Mobility Spectrometry in the Halo IT

Ion mobility spectrometry (IMS)[13] is an electrophoretic separation technique in the gas phase, where ions are separated based on their mobilities as they drift through a buffer gas under the influence of an electric field. Field asymmetric ion mobility spectrometry (FAIMS)[14] was introduced in an attempt to achieve more selectivity than that obtained with traditional IMS by using a strong, high-frequency, amplitude-asymmetric electric field and a weak DC compensation voltage.

The unique design of the halo IT is suitable for performing FAIMS analysis between the two parallel plates. Combining IMS measurement with MS in one device would produce a very powerful analyzer because of its ability to distinguish different ions with identical or nearly identical masses.

If the halo IT could be operated in the sequence of ion mobility analysis to mass analysis, ions of interest could be first selected by FAIMS and then the same ions could be ejected out of the trap in order of *m*/*z* values. During such operation, all ions could first be pushed into the halo IT by the ionization gate for mobility analysis. Then a high DC potential would be applied to the outermost and innermost rings on both plates to keep ions within the trap. At the same time, the rings in the lower plate would be maintained at ground potential while a high-frequency asymmetric waveform is applied to the rings in the upper plate to perform the mobility experiment. Different ions with different mobility values would oscillate between the two plates with different trajectories as a function of the applied waveform. At a certain value of the asymmetric potential waveform, only ions with a corresponding mobility would be allowed to remain, while ions outside the mobility range would be lost by colliding with the plates. Then, the helium bath gas would be decreased to lower the operating pressure for mass analysis. At the same time, the high potential on the outermost and innermost rings would be maintained until the pressure is stabilized for mass analysis. Then an RF waveform would be added to the middle ring for cooling the ions selected by FAIMS, and a standard mass-selective instability scan with resonance ejection would be used for mass analysis. The advantage of operating the halo IT for both mass and mobility analyses sequentially in one mass analyzer is that it would be possible to identify ions not possible with mass analysis alone. For example, isobaric ions with different mobilities could be separated and identified.

6.6 References

1. Badman, E. R.; Cooks, R. G. *J. Mass Spectrom.* 2000, *35*, 659–671.
2. Lammert, S. A.; Plass, W. R.; Thompson, C. V.; Wise, M. B. *Int. J. Mass Spectrom.* 2001, *212*, 25–40.
3. Lammert, S. A.; Rockwood, A. A.; Wang, M.; Lee, M. L.; Lee, E. D.; Tolley, S. E.; Oliphant, J. R.; Jones, J. L.; Waite, R. W. *J. Am. Soc. Mass Spectrom.* 2006, *17*, 916–922.
4. Austin, D. E.; Wang, M.; Tolley, S. E.; Maas, J. D.; Hawkins, A. R.; Rockwood, A. L.; Tolley, H. D.; Lee, E. D.; Lee, M. L. *Anal. Chem.* 2007, *79*, 2927–2932.
5. Zhang, Z.; Peng, Y.; Hansen, B. J.; Miller, I. W.; Wang, M.; Lee, M. L.; Hawkins, A. R.; Austin, D. E. *Anal. Chem.* 2009, *81*, 5241–5248.
6. Peng, Y.; Zhang, Z.; Hansen, B. J.; Wang, M.; Lee, M. L.; Hawkins, A. R.; Austin, D. E. Presented at the 58th ASMS conference, Salt Lake City, UT, May 2010.
7. Hansen, B. J.; Quist, H.; Barley, B.; Hawkins, A. R.; Austin, D. E. Presented at the 58th ASMS conference, Salt Lake City, UT, May 2010.
8. Julian, R. K.; Nappi, M.; Weil, C.; Cooks, R. G. *J. Am. Soc. Mass Spectrom.* 1995, *6*, 57–70.
9. Wang, Y.; Franzen, J.; Wanczek, K. P. *Int. J. Mass Spectrom. Ion Processes*. 1993, *124*, 125–144.
10. Alheit, R.; Kleineidam, S.; Vedel, F.; Vedel, M.; Werth, G. *Int. J. Mass Spectrom. Ion Processes*. 1996, *154*, 155–169.
11. www.comsol.com
12. Sleno, L.; Volmer, D. A. *J. Mass Spectrom.* 2004, *39*, 1091–1112.
13. Eiceman, G. A.; Karpas, Z. *Ion Mobility Spectrometry*, 2nd ed.; CRC Press: Boca Raton, FL; 2005.
14. Buryakov, I. A.; Krylov, E. V.; Nazarov, E. G.; Rasulev, U. Kh. *Int. J. Mass Spectrom. Ion Processes*. 1993, *128*, 143–148.

APPENDIX. SIMION SIMULATION PROGRAMS

SIMION simulations support user-written programs to control and establish most of the properties of ions and fields, such as ion initial parameters in traps, ion-neutral collisions, time-varying electric fields, and other computational parameters. This appendix includes programs written for simulations of ions from creation, collisional cooling, excitation, to ejection according *m*/*z* order in the toroidal and halo ITs. A complicated version was used to understand ion motions in the traps, while a simplified version was used to provide useful results in shorter time.

1 Complicated version of SIMION program

```
-- program for toroidal ion trap
-- created by Daniel Austin
-- revised with resonant ejection frequency scan by Miao Wang
-- written in Lua for SIMION 8

simion.workbench_program()

--define buffer gas parameters
adjustable _gas_mass_amu             = 4     -- amu
adjustable _pressure_pa              = 0.133 -- 0.133 pa = 1 mtorr
adjustable _temperature_k            = 300   -- K
adjustable _mean_free_path_mm        = -1
adjustable _sigma_m2                 = 2.27E-18 -- cross section 200 amu w He

-- define ionization volume
adjustable initial_ion_spread_r       = 1    -- mm radial width
adjustable initial_ion_spread_axial   = 1    -- mm total width

-- define trap parameters
adjustable initial_voltage           = 385   -- volts 0-p
adjustable ionization_time           = 1     -- ms
adjustable cooling_time              = 3     -- ms
  --adjustable ramp_rate               = 0.2   -- V/ms
adjustable trap_frequency            = 3E6 -- Hz driving RF
adjustable detector_voltage          = -1500  -- volts DC
```

```
-- define ejection frequency
adjustable frequency_0               = 1.3E6 -- Hz, beginning ejection frequency
adjustable frequency_1               = 88.5E3 -- Hz, ending ejection frequency
adjustable ramping_time               = 60    --ms
adjustable _eject_voltage             = 2.5      -- volts 0-p
adjustable DC_offset                 = 1        -- volts

-- define maximum time and PE steps
adjustable pe_update_each_usec        = 0.01  -- PE display update
adjustable max_time_step              = 0.01  -- in microsec

-- define other variables

-- functions
function erf(z)
    local z2 = abs(z)
    local t = 1 / (1 + 0.32759109962 * z2)
    local res = (    - 1.061405429 ) * t
    res = (res + 1.453152027 ) * t
    res = (res - 1.421413741 ) * t
    res = (res + 0.2844966736) * t
    res =((res - 0.254829592 ) * t) * exp(-z2*z2)
    res = res + 1
    if z < 0 then res = -res end
    return res
end

function gaussian_random()
    local s = 1
    local v1, v2
    while s >= 1 do
        v1 = 2*rand() - 1
        v2 = 2*rand() - 1
        s = v1*v1 + v2*v2
    end
    local rand1 = v1*sqrt(-2*ln(s) / s)
    return rand1
end
-----------------------------------------------------
function segment.initialize()
    sim_rerun_flym = 1

-- randomize initial ion positions to a cylinder
local radial_position = initial_ion_spread_r * sqrt(rand())
local random_phase = (6.2832 * rand())
local z_offset = sin(random_phase) * radial_position
```

```
local y_offset = cos(random_phase) * radial_position
local x_offset = initial_ion_spread_axial * (rand()-0.5)
ion_px_mm = ion_px_mm + x_offset
ion_py_mm = ion_py_mm + y_offset
ion_pz_mm = ion_pz_mm + z_offset

-- randomize ion time of birth
ion_time_of_birth = ionization_time * rand() * 1000

-- randomize ion velocities to Maxwell curve
local root_kt_m = sqrt((8314 * _temperature_k) / ion_mass)
ion_vx_mm = 0.00155*root_kt_m*(rand()+rand()+rand()+rand()-2)
ion_vy_mm = 0.00155*root_kt_m*(rand()+rand()+rand()+rand()-2)
ion_vz_mm = 0.00155*root_kt_m*(rand()+rand()+rand()+rand()-2)
end
------------------------------------------------------
function segment.tstep_adjust()
  if ion_time_step > max_time_step then ion_time_step = max_time_step
  end
end
------------------------------------------------------
function segment.fast_adjust()
-- control trap RF and ejection frequency

local ramp_start = (cooling_time + ionization_time)*1000
local omega      = 1.0    -- frequency (rad/usec)
local eject_coefficient = 0    -- eject coefficient
local eject_amplitude = 0  -- ejection signal amplitude
local eject_DC_offset = 0  -- DC offset in ejection signal
local Q = 2 * 3.14159 * ramping_time * 1E-3 * frequency_0 * frequency_1 / (frequency_0 -
frequency_1)
   omega = trap_frequency * 2 * 3.14159 * 1E-6       -- frequency (rad/usec)
   if ion_time_of_flight >= ramp_start then
      eject_DC_offset = DC_offset
      eject_amplitude = _eject_voltage
      eject_coefficient = ln ((frequency_0 - frequency_1) * (ion_time_of_flight - ramp_start) /
(ramping_time * 1E3 * frequency_1) + 1)
   end
adj_elect01 = eject_DC_offset
adj_elect02 = initial_voltage * sin(omega * ion_time_of_flight)
adj_elect03 = adj_elect02
adj_elect04 = eject_amplitude * sin(Q * eject_coefficient) + eject_DC_offset
adj_elect05 = detector_voltage
end
-------------------------------------------------------
function segment.other_actions()
```

```
-- ensure PE surfaces are updated regularly
local next_pe_update = 0.0          -- next time to update PE surface
   if ion_time_of_flight >= next_pe_update then
     sim_update_pe_surface = 1
     next_pe_update = ion_time_of_flight + pe_update_each_usec
   end

local last_ion_number = -1
local last_speed_ion = -1
local effective_mean_free_path_mm = -1

-- Define constants
local k = 1.3806505e-23       -- Boltzmann constant (J/K)
local R = 8.3145              -- Ideal gas constant (J/(mol*K))
local kg_amu = 1.6605402e-27  -- (kg/amu) conversion factor
local pi = math.pi            -- PI constant
local eV_J = 6.2415095e+18    -- (eV/J) conversion factor

  -- Compute mean-free-path.
   -- Only recompute mean-free-path if speed_ion has changed

   local vx = ion_vx_mm
   local vy = ion_vy_mm
   local vz = ion_vz_mm

local speed_ion = sqrt(vx^2 + vy^2 + vz^2)
     if abs(speed_ion / last_speed_ion - 1) > 0.05 then
        -- Compute mean gas speed (mm/us)
        local c_bar_gas = sqrt(8*k*_temperature_k/pi/(_gas_mass_amu * kg_amu)) / 1000
       -- Compute median gas speed (mm/us)
       local c_star_gas = sqrt(2*k*_temperature_k/(_gas_mass_amu * kg_amu)) / 1000
       -- Compute mean relative speed (mm/us) between gas and ion.
       local s = speed_ion / c_star_gas
       local c_bar_rel = c_bar_gas * ((s + 1/(2*s)) * 0.5 * sqrt(pi) * erf(s) + 0.5 * exp(-s*s))

        -- Compute mean-free-path (mm)
        effective_mean_free_path_mm = 1000 * k * _temperature_k * (speed_ion / c_bar_rel) /
(_pressure_pa * _sigma_m2)

        -- Store data about this calculation.
        last_speed_ion = speed_ion
     end

   -- Compute probability of collision in current time-step.
   local collision_prob = 1 - exp(- speed_ion * ion_time_step / effective_mean_free_path_mm)
```

```
  if rand() > collision_prob then
    return -- no collision
  end

  -- collision follows (Temperature and kinetic energy used in collision)

  local vr_stdev_gas = sqrt(k * _temperature_k / (_gas_mass_amu * kg_amu)) / 1000
  local vx_gas, vy_gas, vz_gas -- computed velocities
  local scale = speed_ion + vr_stdev_gas * 1.732 * 3  --sqrt(3)=~1.732
  repeat
    vx_gas = gaussian_random() * vr_stdev_gas
    vy_gas = gaussian_random() * vr_stdev_gas
    vz_gas = gaussian_random() * vr_stdev_gas
    local len = sqrt((vx_gas - vx)^2 + (vy_gas - vy)^2 + (vz_gas - vz)^2)
  until rand() < len / scale
  vx = vx - vx_gas
  vy = vy - vy_gas
  vz = vz - vz_gas
  local impact_offset = sqrt(0.999999999 * rand())
  local impact_angle = asin(impact_offset)
  local impact_theta = 2*pi*rand()
  local speed_ion_r, az_ion_r, el_ion_r = rect3d_to_polar3d(vx, vy, vz)
  local vr_ion = speed_ion_r * cos(impact_angle)        -- radial velocity
  local vt_ion = speed_ion_r * sin(impact_angle)        -- normal velocity
  local vr_ion2 = (vr_ion * (ion_mass - _gas_mass_amu)) / (ion_mass + _gas_mass_amu)
  vx, vy, vz = elevation_rotate(90 - deg(impact_angle), vr_ion2, vt_ion, 0)
  vx, vy, vz = azimuth_rotate(deg(impact_theta), vx, vy, vz)
  vx, vy, vz = elevation_rotate(-90 + el_ion_r, vx, vy, vz)
  vx, vy, vz = azimuth_rotate(az_ion_r, vx, vy, vz)
  vx = vx + vx_gas
  vy = vy + vy_gas
  vz = vz + vz_gas
  ion_vx_mm, ion_vy_mm, ion_vz_mm = vx, vy, vz
end
----------------------------------------------------------
function segment.terminate()
  sim_rerun_flym = 0
end
```

2 Simplified version of SIMION program

```
-- program for halo ion trap with slits
-- includes boundary ejection only
-- designed for a PA array, only one adjustable array
-- created by Miao Wang in April 2009 by revising the trap Demo
-- written in Lua for SIMION 8
```

```
simion.workbench_program()

-- particle initial conditions
adjustable percent_energy_variation = 90.0  -- randomized ion energy variation (+- %)
adjustable cone_angle_off_vel_axis = 180 -- random trajectory cone angle (+- degrees)
adjustable random_offset_mm        = 0.1   -- randomized initial ion offset position (in mm)
                                           --   with mid-point at zero offset.

-- collision damping (if enabled)
adjustable _collision_gas_mass  = 4.0    -- mass in amu (helium=4)
adjustable _mean_free_path      = 0.4    -- mean free path in mm

-- define trap parameters
adjustable initial_voltage           = 80   -- volts 0-p
adjustable ionization_time            = 1    -- ms
adjustable cooling_time               = 1    -- ms
adjustable ramp_rate                 = 55.55   -- V/ms
adjustable trap_frequency             = 1.5E6 -- Hz driving RF
   --adjustable detector_voltage           = -2500 -- volts DC

-- define ejection frequency
--adjustable frequency_0               = 1.73E6 -- Hz, beginning ejection frequency
--adjustable frequency_1               = 200E3 -- Hz, ending ejection frequency
adjustable ramping_time               = 100    --ms
--adjustable _eject_voltage            = 15      -- volts 0-p
--adjustable DC_offset                 = 3        -- volts

-- define maximum time and PE steps
adjustable pe_update_each_usec        = 0.005  -- PE display update
adjustable max_time_step              = 0.005  -- in microsec
------------------------------------------------------------
function segment.initialize()
    sim_rerun_flym = 1

-- Randomize ion's position, KE, and direction.

    -- Ensure 0 <= percent_energy_variation <= 100.
    percent_energy_variation = min(abs(percent_energy_variation), 100)
    -- Ensure 0 <= cone_angle_off_vel_axis <= 180.
    cone_angle_off_vel_axis = min(abs(cone_angle_off_vel_axis), 180)

    -- Convert ion velocity vector to 3-D polar coordinates.
    local speed, az_angle, el_angle
        = rect3d_to_polar3d(ion_vx_mm, ion_vy_mm, ion_vz_mm)
```

```
   -- Randomize ion's defined KE.
   local ke = speed_to_ke(speed, ion_mass)
      * (1 + (percent_energy_variation / 100) * (2 * rand() - 1))
   -- Convert new KE back to ion speed, and set it.
   speed = ke_to_speed(ke, ion_mass)

   -- Now, to randomize the ion velocity direction, we first
   -- make the ion's possible random velocity directions fill a solid cone
   -- with vertex at the origin and axis oriented along the positive y-axis.
   -- The angle that the cone side makes with the cone axis will be
   -- the cone_angle_off_vel_axis value.

   -- randomize elevation angle: (90 +- cone_angle_off_vel_axis)
   local new_el = 90 + cone_angle_off_vel_axis * (2*rand()-1)
   -- randomize azimuth angle: (0 +-90)
   local new_az = 90 * (2*rand()-1)

   -- Now that we generated this randomized cone, we will rotate it
   -- so that the expected ion velocity direction matches the ion's
   -- original velocity direction.

   -- Convert to rectangular velocity components.
   local x, y, z = polar3d_to_rect3d(speed, new_az, new_el)
   -- Rotate back to defined elevation.
   x, y, z = elevation_rotate(-90 + el_angle, x, y, z)
   -- Rotate back to defined azimuth.
   ion_vx_mm, ion_vy_mm, ion_vz_mm = azimuth_rotate(az_angle, x, y, z)

   -- Randomize ion's position components.
   ion_px_mm = ion_px_mm + random_offset_mm * (rand() - (1/2))
   ion_py_mm = ion_py_mm + random_offset_mm * (rand() - (1/2))
   ion_pz_mm = ion_pz_mm + random_offset_mm * (rand() - (1/2))

   -- Randomize ion's time of birth.
   ion_time_of_birth = ionization_time * rand() * 1000
end
-------------------------------------------------------
function segment.tstep_adjust()
  if ion_time_step > max_time_step then ion_time_step = max_time_step
  end
end

-------------------------------------------------------
function segment.fast_adjust()
-- control trap RF and ramp
```

```
local ramp_start = (cooling_time + ionization_time)*1000
local omega      = 1.0    -- frequency (rad/usec)
local amplitude = initial_voltage
   omega = trap_frequency * 2 * 3.14159 * 1E-6  -- frequency (rad/usec)
   if ion_time_of_flight > ramp_start then
      amplitude = initial_voltage + ((ion_time_of_flight - ramp_start)*ramp_rate)
   end
adj_elect00 = amplitude * sin(omega * ion_time_of_flight)
end

-----------------------------------------------------------
function segment.other_actions()

-- ensure PE surfaces are updated regularly
local next_pe_update = 0.0 -- next time to update PE surface
   if ion_time_of_flight >= next_pe_update then
     sim_update_pe_surface = 1
     next_pe_update = ion_time_of_flight + pe_update_each_usec
   end

-- simple collision
-- Get particle speed v.
   local v, az, el = rect3d_to_polar3d(ion_vx_mm, ion_vy_mm, ion_vz_mm)
   -- Compute distance step (distance traveled in time-step) in mm
   local distance_step = v * ion_time_step

   -- Detect collision.
   -- This uses a probability of collision by comparing the
   -- distance step to the mean-free-path.
   if rand() <= 1 - exp(- distance_step / _mean_free_path) then
      -- Attenuate velocity, ASSUMING direct hit on still gas molecule.
      v = v * (ion_mass - _collision_gas_mass) / (ion_mass + _collision_gas_mass)
      -- Convert back to rectangular coordinates and save.
      ion_vx_mm, ion_vy_mm, ion_vz_mm = polar3d_to_rect3d(v, az, el)
   end

--to end flights that get stuck past resonant frequency
    if ion_time_of_flight > (ramping_time + ionization_time + cooling_time) * 1000 then
      ion_splat = -1 end
end

-----------------------------------------------------------
function segment.terminate()
   sim_rerun_flym = 0
end
```